
# Nonlinear Optics Pulse Propagation in Fiber Optics filled with gases, liquids, and organic dyes.

**Sebastian Vergara Palacio**

Universidad Nacional de Colombia
Facultad de Ciencias, Escuela de Física
Medellín, Colombia
2019

# Nonlinear Optics Pulse Propagation in Fiber Optics filled with gases, liquids, and organic dyes.

**Sebastian Vergara Palacio**

Tesis o trabajo de grado presentada(o) como requisito parcial para optar al título de:
**Magister en Física**

Director(a):
Ph.D. Rodrigo Acuña Herrera

Línea de Investigación:
Nonlinear Optics.
Grupo de Investigación:
Fotónica y Opto-electrónica

Universidad Nacional de Colombia
Facultad de Ciencias, Escuela de Física
Medellín, Colombia
2019

A mi madre, Astrid. Mi abuela, Yolanda. Mis dos hermanos: Nataly y julian. Y a Linda y Haku .

...No hay que olvidar que en el sur, solo en su pequeño barquito, un hombre combatia contra huracanes, contra olas de siete y ocho metros de altura, contra el hambre y dolor de su cuerpo... contra el silencio y la soledad mas cerrados, solo para recordarnos que hay una zona de nosotros que es capaz de sobreponerse a toda adversidad, una zona de pureza incontaminada, una zona donde esta lo mejor de nosotros mismos. Casi nada

Mario Mendoza

# Resumen

La caracterización de propiedades ópticas no lineales, como lo son el índice de refracción y el coeficiente de absorción no lineal, es uno de los temas más importantes en óptica no lineal debido a su aplicación en muchos campos como la espectroscopia, procesamiento de materiales, biofísica, sensado atmosférico, metrología, entre otros. Además de la posibilidad de creación de nueva tecnología. En esta tesis se implementó y calibró la técnica Z-Scan, una de las técnicas más utilizadas para obtener tanto el índice de refracción no lineal como el coeficiente de absorción de un material. Asimismo, los fenómenos no lineales dentro de la fibra óptica son bien conocidos debido a sus aplicaciones y ventajas tales como la baja energía de entrada requerida para generar fenómenos de supercontinuo, mezclado de cuatro ondas y ondas dispersivas. En este trabajo se realizaron varias simulaciones con nuevas geometrías de fibras, respuestas de material y gases nobles dentro de la fibra. Se consideraron diferentes regímenes de potencia de entrada, ancho de pulso y presión. Se reportaron los parámetros no lineales para las sustancias orgánicas usadas, nanotubos de carbono de paredes múltiples y $CS_2$, indicando la razón principal detrás de cada resultado y abordando los posibles nuevos fenómenos involucrados. La respuesta de salida no lineal tanto en el dominio del tiempo como en el de frecuencia se reportó en varias simulaciones, obteniendo el pulso no lineal de salida para la nueva función de respuesta del $CS_2$, se propuso una nueva consideración donde el pulso final depende de la distancia de propagación para materiales no instantáneos y la constante no lineal ($\gamma$) se deben recalcular en cada paso. Se demostró cómo se puede controlar el pulso de salida cambiando la longitud de la fibra; entre los resultados más importantes se encontró la posibilidad de cambiar entre la inestabilidad de la modulación y el mezclado de cuatro ondas solo variando la distancia de propagación. Finalmente, se encontró que un tipo especial de fibra, a saber, la fibra de núcleo hueco de curvatura negativa, se puede usar para obtener un amplio espectro de banda cuando se llena con gases nobles y se sintoniza con la presión, desde el comportamiento lineal hasta la zona supercrítica.

**Palabras clave: óptica no lineal, Z-scan, generación de supercontinuo, onda dispersiva, mezclado de cuatro ondas, índice de refracción no lineal, fibra de cristal fotónico de núcleo hueco, fenómenos no lineales.**

# Abstract

The characterization of nonlinear optical material properties, such as nonlinear refractive index and nonlinear absorption coefficient, is one of the most important subjects in nonlinear optics due to its application in many fields such as spectroscopy, material processing, biophysics, atmospheric sensing and metrology, among others. Besides the possibility of creating new technology. In this thesis, the Z-scan technique was implemented and calibrated. It remains one of the most widely used techniques to obtain both nonlinear refractive index and the absorption coefficient of a material. Moreover, nonlinear phenomena inside optical fiber is well known due to their applications and advantages like the low input energy required to generate supercontinuum, four wave mixing, dispersive wave, among others. In this work, several simulations were performed with new fiber geometries, material responses and different noble gases infiltrated in fiber. Different simulation regimes were considered as well by varying input power, pulse width and pressure. Nonlinear parameters for organic dyes, multi-walled carbon nanotubes, and $CS_2$ were reported, pointing out the main reasons behind each result and addressing possible new phenomena involved. The nonlinear output response in both time and frequency domains was reported for several simulations, obtaining the nonlinear pulse output for the new $CS_2$ response function. A novel consideration was proposed in which the final pulse depends on the propagation distance for non-instantaneous materials and the nonlinear constant ($\gamma$) must be recalculated at each step. It was demonstrated how the output pulse can be controlled by changing the fiber length. Among the most important results, it was found there exists a possibility to change between modulation instability and four wave mixing by only varying the propagation distance. Finally, it was also found that a special type of fiber, namely negative curvature hollow core fiber, can be used to obtain a broad band spectrum when it is filled with noble gases and they can be tuned with pressure from linear behavior up to a super critical zone.

**Keywords: Non-linear optics, Z-scan, supercontinuum generation, dispersive wave, four wave mixing, nonlinear refractive index, hollow core photonic crystal fiber, nonlinear phenomena.**

# Hypothesis

Implementation of a temporal resolution nonlinear optical characterization technique Z-scan. To achieve it, first a research about the theoretical bibliography involved in the technique is going to be performed , then the set up implementation and finally the technique validation through the measurement of different and known nonlinear substances as $CS_2$. In the set up implementation a code is going to be develop to have control about the variables involved in the measurement where the all system is going to be integrated: physical and software to finally obtain the nonlinear coefficients. This is to the aim of answer different questions about substances such as: pulse width, power and concentration influence in the measurement. On the other hand, how an optical pulse that travels inside fiber optic is affected in its width and shape both in temporal and frequency domain under different circumstances: fiber geometry, fiber material filled, input pulse parameters, among others will be addressed. For this purpose simulations will be performed taking into account the theory known at the moment and contrast it with the results.

# General Objective

To Study theoretical and experimentally the nonlinear pulse propagation in fiber optics infiltrated with inert gasses and liquids.

# Specific Objectives

- To measure the nonlinear properties of some liquids and organic dyes by using the Z-scan technique.
- To simulate the nonlinear pulse propagation in fibers filled with inert gases, liquids, and organic dyes.

# Contents

# Figure list

# Table list

# 1. List of symbols and abbreviations

## Symbols

| | | |
|---|---|---|
| $E$ | — | Electric field. |
| $P$ | — | Polarization. |
| $\chi^{(i)}$ | — | ith order susceptibility. |
| $n_2$ | — | nonlinear refractive index. |
| $n_{2,el}$ | — | Nonlinear refractive index due to the electronic response. |
| $n_{2,mol}$ | — | nonlinear refractive index due to the molecular contribution. |
| $\omega_0$ | — | Central pump wavelength . |
| $\varepsilon$ | — | dielectric constant with its nonlinear part. |
| $\varepsilon_0$ | — | dielectric constant in vacuum. |
| $k_0$ | — | Pump wave vector. |
| $\beta$ | — | Propagation constant. |
| $\gamma$ | — | Nonlinear coefficient. |
| $\gamma(z)$ | — | Nonlinear coefficient propagation dependent. |
| $R(t)$ | — | Raman response function. |
| $f_R$ | — | fractional contribution of the delayed Raman response to nonlinear polarization. |
| $L_{NL}$ | — | Nonlinear length. |
| $L_D$ | — | Dispersive length. |
| $P_0$ | — | Initial peak power. |
| $P_s$ | — | Peak power of fundamental soliton. |
| $T_0$ | — | Initial pulse width. |
| $\phi_{NL}$ | — | Nonlinear phase. |
| $N$ | — | Soliton number. |
| $\beta_2$ | — | Group velocity dispersion. |
| $I_s$ | — | Stoke intensity. |
| $I_p$ | — | Pump intensity. |
| $g_R$ | — | Raman gain coefficient. |
| $\omega_s$ | — | Soliton frequency. |
| $\omega_d$ | — | Phase matching in Dispersive wave. |

$\rho_d$ — Normalized dispersive wave power.
$\delta_m$ — normalized dispersion parameter.
$\omega_{FWM}$ — Four wave mixing frequency.
$\Omega_s$ — Phase matching condition for four wave mixing.
$\alpha_0$ — Linear absorption.
$z_0$ — Rayleigh distance.
$L_{eff}$ — Effective sample length.
$T(z)$ — Normalized transmittance in Z-scan technique.
$\Delta T_{p-v}$ — difference peak valley in the transmittance, Z-scan technique.
$CS_2$ — Carbon disulfide.
$\mu_{mn}$ — dipole moment between $m$ and $n$ states.
$A_{eff}$ — Effective area.
$T_{FWHM}$ — Pulse width at half maximum.
$f_m$ — Molar fraction.
$h'(t)$ — Characteristic response time of the nuclear mechanisms.
$r_d(t)$ — Diffusive contribution.
$r_l(t)$ — Librational contribution.
$r_c(t)$ — Collision contribution.
$P_{cr}$ — Critical power to achieve ionization .

## Operators

$\hat{D}$ — Differential operator.
$\hat{N}$ — Nonlinear operator.

## Abbreviations

$GVD$ — group velocity dispersion.
$SPM$ — self-phase modulation.
$SRS$ — Spontaneous Raman scattering .
$CW$ — Continuous wave.
$TOD$ — Third order dispersion.
$DW$ — Dispersive wave.
$SCG$ — Supercontinuum generation .
$ZDW$ — Zero dispersion wavelength .
$SVEA$ — Slowly varying envelope approximation .
$GD$ — Gaussian decomposition method.
$PCF$ — Photonic crystal fiber.

$HCPCF$ — Hollow core photonic crystal fiber.
$LCPCF$ — Liquid core photonic crystal fiber.
$NHCPCF$— Negative hollow core photonic crystal fiber.
$FEM$ — Finite element modeling.
$NLSE$ — Nonlinear Schrödinger equation.
$GNLSE$ — Generalized nonlinear Schrodinger equation.
$FFT$ — Fast Fourier transform.
$MWCNT$ — Multi walled carbon nanotubes.
$TPA$ — Two photon absorption.
$NSR$ — Non-solitonic radiation.
$NT$ — Nonlinear terms.

# 2. Introduction

The study of nonlinear optic properties is of great importance due to its applications in many fields as spectroscopy, frequency metrology, sensing, arbitrary waveform generation [1], telecommunications, laser development, and fundamental science such as modelling of relativistic systems or statistical rogue wave formation [68] among others. Nonlinear phenomena occur at high power levels because the magnitude of the nonlinear properties are very low, so it's necessary a high interaction that these properties can be considered. There are many factors that affect the nonlinear propagation through fiber optics which need to be considered in order to study the mechanism of generation of different phenomena, some of them are the optical pulse intensity, temporal width, material, and fiber structures. In the interaction between light and material, there are different terms that account for different properties, one approach to understand the influence of each term in the interaction is using the nonlinear Schrodinger equation (NLSE) [2]. This equation allows us to make simulations and compare with experimental studies in order to understand how the light interacts with different materials. Some terms involved in the NLSE are: dispersion, random noise, kerr effect, and Raman response. Mixing of these effects can turn out in amazing behaviors, like optical solitons formation which is a result of the interplay between the dispersion and the kerr effect [13], [14], [15]. It is very important to have a correct nonlinear characterization of the material under study in order to be able of interpreting the results and make good calculations, with the goal of identifying each phenomenon and have a clear picture of the physics. To do this, there are many techniques, one of them, that have attracted a lot of attention because its velocity, and versatility, is the Z-scan technique, where is possible identifying the nonlinear refractive index and the nonlinear absorption coefficient at the same time [22], [23], [24]. This technique is implemented in chapter four, where was made a program to obtain the nonlinear refractive index and absorption coefficient, where we have correctly measured some materials such as $CS_2$ , Organic dyes, ethanol and Multiwalled carbon nanotubes. The major attractive of some kind of liquids and organic dyes are the high nonlinear refractive indexes, which permit to work with low power lasers. There are other ways to obtain a considerable reaction between light and materials, one of these is by means of the fiber infiltration with these liquids or even gases where light is confined with the objective of getting more nonlinear interaction. On the other hand, the use of gases, which exhibit new properties and applications like filamentation that works as wave guide through so many kilometers without almost any losses, have received much attention due to its capability to

measure atmospheric pollutants [7], [25], [26], [33]. Another interesting property of gases is that they do not suffer easily damage due to the use of high energy lasers, facilitating the appearance of new phenomena like ionization that generate a dispersive wave in the ultra violet region, which is a good start to study new physics and applications, besides this opens the door to enhance the spectral broadband in the supercontinuum generation. In this work, we will focus on nonlinear calculations in fiber structures infiltrated with liquids and gases, with different pump pulse parameters such as intensity, pulse width, and wavelength. Where the principal objective of this thesis is the theoretical and experimental study of the nonlinear pulse propagation in fiber optics infiltrated with inert gases and liquids, to achieve it the work will focus in the nonlinear properties measurement of some liquids by the Z-scan technique (chapter four) and the simulation of the nonlinear pulse propagation in fibers filled with inert gases, liquids, and organic dyes (chapter five), besides a preliminary fiber infiltration system is proposed and its fabrication is described to the experimental study of nonlinear pulse propagation (appendix A).

# 3. Theoretical framework

## 3.1. Fundamentals of nonlinear optics

### 3.1.1. Chromatic Dispersion

The bound electrons' response in a dielectric to an external electric field is known as chromatic dispersion, which is manifest trough the frequence dependency of the refractive index $n(\omega)$. Far from a medium's resonances, the refractive index can be approximated by the Sellmeier equation [2] :

$$n^2(\omega) = 1 + \sum_{j=1}^{m} \frac{B_j \omega_j^2}{\omega_j^2 - \omega^2} \tag{3-1}$$

Where $\omega_j$ is the resonance frequency and $B_j$ is the strength of $j$th resonance. Conventionally, these parameters are obtained by fitting the dispersion curves. For the case of gases, the Sellmeier equation can be modified to take into account the pressure and temperature dependencies [3] and thus can be written as [4].

$$n^2(\lambda, \rho, T) - 1 = \frac{\rho}{\rho_0} \cdot \frac{T_0}{T} \cdot \left( \frac{B1\lambda^2}{\lambda^2 - C_1} + \frac{B2\lambda^2}{\lambda^2 - C_2} \right) \tag{3-2}$$

In the nonlinear regime, the combination of dispersion and nonlinearity create new phenomena that will be discussed more thoroughly in the next chapters. In table**3-1**, it is presented some gases used along this thesis and their Sellmeier coefficients, including one correction from [4].

**Table 3-1**.: Sellmeier coefficients for some gases at $1000mbar$ and $0°c$ take it from [4]

| Gas | $B1 \times 10^{-8}$ | $C1 \times 10^{-6}$ | $B2 \times 10^{-8}$ | $C2 \times 10^{-3}$ |
|---|---|---|---|---|
| Argon | 20332.29 | 206.12 | 34458.31 | 8.066 |
| Krypton | 26102.88 | 2.01 | 56946.82 | 10.043 |
| Xenon | 103701.61 | 12.75 | 31228.61 | 0.561 |

The effects of fiber dispersion are included by expanding the propagation constant $\beta$ in a Taylor series around the frequency $\omega_0$ at which the pulse spectrum is centered:

$$\beta(\omega) = n(\omega)\frac{\omega}{c} = \beta_0 + \beta_1(\omega - \omega_0) + \frac{1}{2}\beta_2(\omega - \omega_0)^2 + ... \tag{3-3}$$

The envelope of an optical pulse travels at the group velocity, the parameter $\beta_2$ represents dispersion of the group velocity and is responsible for pulse broadening. This phenomenon is known as *group velocity dispersion* (GVD). The dispersion parameter D is related to $\beta_2$ and $n$ as follows:

$$D = \frac{\mathrm{d}\beta_1}{\mathrm{d}\lambda} = -\frac{2\pi c}{\lambda^2}\beta_2 = -\frac{\lambda}{c}\frac{\mathrm{d}^2 n}{\mathrm{d}\lambda^2} \tag{3-4}$$

From equations 3-3 and 3-4 it can be seen that the dispersion parameter depends on the material and the structure of the waveguide. For the different fiber structures considered, the GVD can be changed to reach a desire effect. Gases exhibit an interesting phenomenon, the GVD can be tuned through pressure and temperature while keeping the same fiber geometry. When $\beta_2 > 0$, the fiber is said to exhibit normal dispersion while for $\beta_2 < 0$ the fiber exhibits anomalous dispersion. Thus, one can expected to see different GVD behaviour under distinct conditions of fiber geometry, medium of propagation and pressure.

### 3.1.2. Maxwell equations

The propagation of an electric field is governed by Mawxell's equations, which in differential form are read as:

$$\bigtriangledown \times \mathbf{E} = -\frac{\partial \mathbf{B}}{\partial t} \tag{3-5}$$

$$\bigtriangledown \times \mathbf{H} = \mathbf{J} + \frac{\partial \mathbf{D}}{\partial t} \tag{3-6}$$

$$\bigtriangledown \cdot \mathbf{D} = \rho_f \tag{3-7}$$

$$\bigtriangledown \cdot \mathbf{B} = 0 \tag{3-8}$$

where $E$ and $H$ are electric and magnetic fields, respectively, and $D$ and $B$ are electric and magnetic flux densities. In the absence of free charges: $J = 0$ and $\rho_f = 0$. The flux densities $D$ and $B$ arise in response to $E$ and $H$ propagating inside the medium and are related through:

$$\mathbf{D} = \varepsilon_0 \mathbf{E} + \mathbf{P} \tag{3-9}$$

$$\mathbf{B} = \mu_0 \mathbf{H} + \mathbf{M} \tag{3-10}$$

for a nonmagnetic medium $M = 0$. By taking the curl of eq.3-5 and using eq.3-6, eq.3-9 and eq.3-9 one can obtain the wave equation that describes light propagation in optical fibers:

$$\bigtriangledown \times \bigtriangledown \times \mathbf{E} = -\frac{1}{c^2}\frac{\partial^2 \mathbf{E}}{\partial t^2} - \mu_0 \frac{\partial^2 \mathbf{P}}{\partial t^2} \tag{3-11}$$

where $P$ is known as polarization and it is in this term that optical nonlinearity lies. Far from medium resonances, $P$ can be expressed as two parts: one accounts for linear response and the other for the nonlinear response $P(r,t) = P_L(r,t) + P_{NL}(r,t)$. Considering $P_{NL}(r,t)$ as a small perturbation term and $n(\omega)$ independent of position one can turn eq.3-11 into the Helmholtz equation, with the identity:

$$\bigtriangledown \times \bigtriangledown \times \mathbf{E} \equiv \bigtriangledown(\bigtriangledown \cdot \mathbf{E}) - \bigtriangledown^2 \mathbf{E} = -\bigtriangledown^2 \mathbf{E} \tag{3-12}$$

and the Helmholtz equation with the electric field in the frequency domain

$$\bigtriangledown^2 \widetilde{\mathbf{E}} + n^2(\omega)\frac{\omega^2}{c}\widetilde{\mathbf{E}} = 0 \tag{3-13}$$

### 3.1.3. Source of nonlinearities

When an external electric field's magnitude is high enough for a certain dielectric medium, its response starts to be significantly nonlinear, where the bound electrons exhibit an an-

harmonic motion in response to the electric field. As result, the total polarization $P$ can be expressed as

$$\mathbf{P} = \varepsilon_0 \left( \chi^{(1)} \cdot \mathbf{E} + \chi^{(2)} : \mathbf{EE} + \chi^{(3)} \vdots \mathbf{EEE} + ... \right) \tag{3-14}$$

where $\chi^{(i)}$ is the ith susceptibility. $\chi^{(2)}$ is zero for the case of centrosymmetric crystalline media as is the case of fused silica, so $\chi^{(3)}$ plays a dominant role in nonlinear fiber optical propagation. In a simplified form, the refractive index with the intensity dependence can be expressed as:

$$\widetilde{n}(\omega, I) = n(\omega) + n_2 I = n + \overline{n_2}|E|^2 \tag{3-15}$$

where $I$ is the optical intensity and $\overline{n_2}$ is the nonlinear index coefficient related to $\chi^{(3)}$ by the relation $\overline{n_2} = \frac{3}{8n} Re(\chi^3)$.

The nonlinear refractive index $n_2$ is a intrinsic property of the material, some relevant values for this thesis are tabulated in table **3-2**.

**Table 3-2**.: $n_2$ for some relevant gases used in this thesis [5], [6]

| | $n_2(\times 10^{-20} m^2/W)$ | | | |
|---|---|---|---|---|
| **material** | **1 bar** | **25 bar** | **90 bar** | **140 bar** |
| Argon | 0.001268 | 0.013 | 0.8 | 0.9 |
| Krypton | 0.003069 | 0.015 | 0.1 | 0.19 |
| Xenon | 0.09158 | 0.12 | 1.4 | 1.6 |

### 3.1.4. Pulse propagation

Assuming a quasi-monochromatic pulse spectrum, centered at $\omega_0$ and with spectral width $\Delta\omega$ such that $\Delta\omega/\omega_0 << 1$ and under the slowly varying envelope approximation, the electric field can be expressed as:

$$\mathbf{E}(\mathbf{r}, t) = \frac{1}{2} \widehat{x} [E(\mathbf{r}, t) exp(-i\omega_0 t) + c.c] \tag{3-16}$$

where $E(\mathbf{r}, t)$ is a slowly varying function of time. In a similar way, $\mathbf{P}$ and $\mathbf{P}_{NL}$ can be expressed. Substituting eq.3-16 and each corresponding $\mathbf{P}$ and $\mathbf{P}_{NL}$ in the spectral domain

into eq.3-11, the result is found to satisfy the Helmholtz equation:

$$\bigtriangledown^2 \widetilde{E} + \varepsilon(\omega) k_0^2 \widetilde{E} = 0 \tag{3-17}$$

where $k_0$ is the wave vector and $\varepsilon(\omega) = 1 + \widetilde{\chi}^{(1)}(\omega) + \varepsilon_{NL}$ is the dielectric constant with its nonlinear part. Equation 3-17 can be solved by using separation of variables. Assuming a solution of the form $\widetilde{E}(\mathbf{r}, \omega - \omega_0) = F(x, y)\widetilde{A}(z, \omega - \omega_0) exp(i\beta_0 z)$.

Using the Taylor series expansion presented before for $\beta$ one can find:

$$\frac{\partial A}{\partial z} + \beta_1 \frac{\partial A}{\partial t} + i\frac{\beta_2}{2}\frac{\partial^2 A}{\partial t^2} + \frac{\alpha}{2}A = i\gamma(\omega_0)|A|^2 A \tag{3-18}$$

where the Taylor expansion was considered up to the second order nonlinear coefficient and $\alpha$ accounts for losses. The nonlinear parameter $\gamma$ is defined, under the condition that $F(x, y)$ varies slowly over the pulse bandwidth, as:

$$\gamma(\omega_0) = \frac{\omega_0 \overline{n}_2 \iint_{-\infty}^{\infty} |F(x,y)|^4 dxdy}{c \iint_{-\infty}^{\infty} |F(x,y)|^2 dxdy} \tag{3-19}$$

This expression holds under the assumption of an instantaneous response i.e. involving only electrons. Now, considering non-instantaneous response, electronic and nuclear, the $\mathbf{P}_{NL}$ takes the form:

$$P_{NL}(\mathbf{r}, t) = \frac{3\varepsilon_0}{4}\chi^3_{xxxx} E(\mathbf{r}, t) \int_{-\infty}^{t} R(t - \tau)|E(\mathbf{r}, t)|^2 d\tau \tag{3-20}$$

After some straightforward manipulation one can obtain **the generalized Nonlinear schrödinger equation** (**GNLSE**)

$$\frac{\partial A}{\partial z} + \frac{1}{2}(\alpha(\omega_0) + i\alpha_1 \frac{\partial}{\partial t})A - i\sum_{n=1}^{\infty} \frac{i^n \beta_n}{n!}\frac{\partial^n A}{\partial t^n} = i(\gamma(\omega_0) + i\gamma_1 \frac{\partial}{\partial t})(A(z,t) \int_0^{\infty} R(t')|A(z, t - t')|^2 dt' \tag{3-21}$$

where $R(t)$ is known as the Raman response function and includes both the electronic and nuclear contributions, its functional form can be written as:

$$R(t) = (1 - f_R)\delta(t) + f_R h_R(t) \tag{3-22}$$

$f_R$ represents the fractional contribution of the delayed Raman response to nonlinear polarization $\mathbf{P}_{NL}$. In the case of noble gases there is no Raman response, so only the electronic response may be taken into account.

**Table 3-3**.: some characteristics terms of GNLSE and its main contribution.

| **Dispersion contribution** | |
|---|---|
| Group velocity dispersion (GVD) | $\frac{1}{2}\beta_2(\partial^2 A/\partial T^2)$ |
| Third order dispersion (TOD) | $\frac{1}{6}\beta_3(\partial^3 A/\partial T^3)$ |
| **Nonlinear contribution** | |
| Kerr effect | $i\gamma A(1-f_R)\lvert A\rvert^2$ |
| Raman effect | $i\gamma A\int_0^\infty f_R h_R(t')\lvert A(z,t-t')\rvert^2 dt'$ |
| self steepening | $-\frac{1}{\omega_0}\frac{\partial}{\partial T}A(1-f_R)\lvert A\rvert^2$ |
| self frequency shift | $-\frac{1}{\omega_0}\frac{\partial}{\partial T}\int_0^\infty f_R h_R(t')\lvert A(z,t-t')\rvert^2 dt'$ |

It is possible to define some useful variables that account for the physics of pulse propagation. For example the scaling length can be defined as:

$$L_{NL} = \frac{1}{\gamma P_0} \tag{3-23}$$

and

$$L_D = \frac{T_0^2}{|\beta_2|} \tag{3-24}$$

where $P_0$ is the peak intensity and $T_0$ is the initial pulse width. The dispersion must be take it into account for pulses traveling over distance $L > L_D$, and is the same for nonlinear phenomena $L > L_{NL}$. For a fiber such that $L < L_D$ and $L < L_{NL}$ neither the dispersive nor nonlinear effects affect the propagating pulse. When $L_D \sim L$ and $L << L_{NL}$ the dispersive effects dominate over nonlinear effects and vice versa.

### 3.1.5. Self-phase modulation

Considering a pulse travelling a distance $L$, such that $L_{NL} < L << L_D$ one can consider only nonlinear effects and neglect dispersion effects. Without considering dispersive terms and only electronic response the pulse propagation equation can be written, with zero losses, as follows:

$$\frac{\partial A}{\partial z} = \frac{i}{L_{NL}}|A|^2 A \tag{3-25}$$

equation 3-25 has a solution of type

$$A(L,T) = A(0,T)exp(i\phi_{NL}(L,T)) \tag{3-26}$$

and

$$\phi_{NL}(L,T) = |A(0,T)|^2(L/L_{NL}) \tag{3-27}$$

The spectral changes induced by self-phase modulation (SPM) are a direct consequence of the time dependence of $\phi_{NL}$. A temporally varying phase implies that the instantaneous optical frequency differs across the pulse from its central value. The difference is given by $\delta\omega(T)$ as:

$$\delta\omega(T) = -\frac{\partial\phi_{NL}}{\partial T} = -(\frac{L}{L_{NL}})\frac{\partial|A(0,T)|^2}{\partial T} \tag{3-28}$$

New frequencies are generated continuously as the pulse propagates down the fiber. The SPM-induced chirp can produce spectral broadening or narrowing depending on the initial chirp. For the case of unchirped pulses, the spectral always will be broader. Considering an unchirped Gaussian pulse, the trailing part will shift towards higher frequencies (blue shift) as $\frac{\partial|A(0,T)|^2}{\partial T} < 0$, while the leading part will experience a frequency down shift (red shift), $\frac{\partial|A(0,T)|^2}{\partial T} > 0$.

### 3.1.6. Self-focusing

When a Gaussian beam has a transverse intensity distribution, i.e., the intensity at the center is much stronger than at the edges. Thus when a Gaussian beam propagates in a nonlinear medium, the Kerr effect leads to a refractive index distribution inside the medium that is non-uniform along the radial direction. In this scenario, the medium plays a role similar to a lens, the profile size of the beam will continuously be changed between convergence or divergence, as is shown in Fig.3-1.

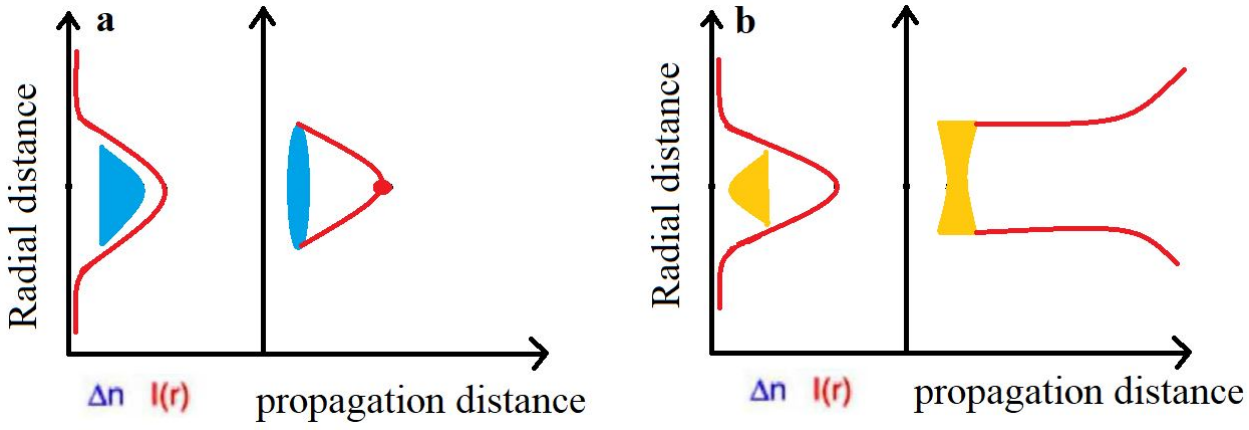


**Figure 3-1**.: self-focusing effect inside a nonlinear medium: a. Self-focusing, $n_2 > 0$. b. Self-defocusing, $n_2 < 0$.

In the self-focusing process, there is a competition between self-focusing and diffraction, in this continuous shift between focus and defocus at some point the beam could achieve a

balance and a self-trapping effect will take place. This process is the *space optical soliton effect*. The laser intensity required to produce self-focusing will be [8]:

$$I \geq \frac{n_0}{2n_2k^2a^2} \tag{3-29}$$

where $a$ is the beam waist radius of the laser. It's worthwhile to notice that this is the fundamental principle of the Z-scan technique.

### 3.1.7. Self-steepening

The group velocity of a pulse propagating in a Kerr medium presents an intensity dependence that results in pulse distortion. The peak of the pulse moves slower than its trailing edge. Unlike the effect caused by SPM, the broadening due to Self-steepening is asymmetric. Since the SPM causes the trailing edge (blue components) to become steep, the overall broadening spectrum is significantly more blue shifted when compared to SPM. however, although the pulse spectrum is more blue shifted, the red shifted peaks become more intense.

### 3.1.8. Temporal soliton

Soliton refers to a kind of wave that can propagate undistorted over long distances. Optical solitons occur when both dispersion parameters and nonlinear parameters have an impact on the propagating pulse, giving as a result a balance between both effects. Introducing three dimensionless variables:

$$U = \frac{A}{\sqrt{P_0}}, \xi = \frac{z}{L_D}, \tau = \frac{T}{T_0} \tag{3-30}$$

Additionally, an important parameter is defined: *the soliton number*, $N$, which accounts for the relationship between the dispersive length and nonlinear length, and it is a good indicator in many dynamics and processes about the beam evolution. In this work we will consider the following definition of $N$:

$$N^2 = \frac{L_D}{L_{NL}} = \frac{\gamma P_0 T_0^2}{|\beta_2|} \tag{3-31}$$

where $N$ does not have to be an integer. Finally, defining $u = NU$ and considering only instantaneous process and GVD, the standard form of the NLS equation is obtain

$$i\frac{\partial u}{\partial \xi} + \frac{1}{2}\frac{\partial^2 u}{\partial \tau^2} + |u|^2 u = 0 \tag{3-32}$$

In the equation 3-32, $\beta_2$ is negative. This sign that accompanies the second derivative with respect to time is convened to be negative when the pulse is propagating in anomalous regime. The previous equation can be solved by the inverse scattering method, for the case of fundamental soliton $N = 1$ it's defined as:

$$u(\xi, \tau) = sech(\tau)exp(i\xi/2) \tag{3-33}$$

In absence of higher order nonlinear and dispersive effects, a higher solution of soliton $N > 1$, changes its shape and returns to its original form periodically. These periods are known as soliton periods: $L_{sol} = (\pi/2)L_{LD}$. As the soliton propagates it splits in $(N - 1)$ distinct pulses around $L_{sol}/2$ only to rejoin to its original shape after a soliton period.

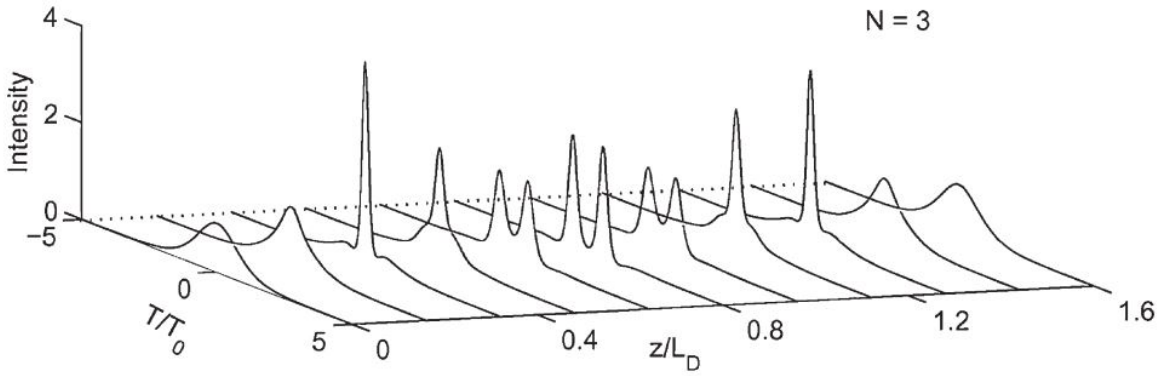


**Figure 3-2**.: Temporal evolution of higher soliton number $N = 3$ over one soliton period, higher nonlinear and dispersive effects are ignored. [2]

In case the soliton number is not be an integer, the pulse will evolve behaving as if it were an integer soliton, for example $N = 1.3$ behaves as $N = 1$. Part of this extra energy is shed away in the form of dispersive waves. Under non-ideal conditions, solitons can be subjected to many types of perturbations as they propagate, such as: fiber losses, noise, third order dispersion and intra pulse Raman scattering. In the presence of these phenomena, higher order solitons can split into fundamental solitons, this process is known as soliton fission, the solitons are ejected one after the other with the earliest ejected having the highest peak power, shortest duration and propagating with the fastest group velocity. This process is fundamental to understanding some interplay effects like deep ultra violet vacuum dispersive wave generation, that will be addressed in more detail later.

### 3.1.9. Stimulated Raman Scattering

In any molecular medium, spontaneous Raman scattering (SRS) can transfer part of the energy from one optical field to another, whose frequency is downshifted. In noble gases, SRS is not present, making them suitable to studies that imply spectral broadening without this contribution [9], [10], [20]. In a simple approach, valid under continuous wave (CW) and quasi continuous wave conditions, the initial grow in stokes waves can be described as

$$\frac{\mathrm{d}I_s}{\mathrm{d}z} = g_R I_p I_s \tag{3-34}$$

Where $I_s$ is the stoke intensity and $I_p$ is the pump intensity, and the Raman gain coefficient, $g_R$, is related to the cross section of the stimulated Raman scattering, which is related to the imaginary part of the third order susceptibility. The Raman gain depends on the composition of the fiber core.
Assuming pulse widths larger than the Raman response time so that transient effects are negligible. Wave lengths of the pulse Raman can lie in normal or anomalous GVD, when it is localized in anomalous region soliton effect become important and Raman pulse can propagate as a soliton. Numerical results have shown the formation of Raman soliton when the pulse is formed at a distance at which the pump pulse, propagating as a higher-order soliton, achieves its maximum width. So that the solitons are formed is necessary that $L_D \sim L_w$, where $L_w$ is known as the walk-off length and is defined as

$$L_w = \frac{T_0}{|d|} \tag{3-35}$$

and $d$ is the walk-off parameter that accounts for the group velocity mismatch between the pump and the Raman pulse, $d = v_{gp}^{-1} - v_{gs}^{-1}$. The Raman effect is a shift to red wavelengths and in the time domain is seen as a pulse that lags behind the input pulse because the red components travel slowly in the anomalous GVD regime.

### 3.1.10. Dispersive Wave

From eq.3-31, when $N = 1.5$ the optical pulse propagates as $N = 2$ and as $N > 1$, the soliton undergoes fission process due to the perturbation by the third or higher order dispersion terms. The importance of the parameter $N$ is clear as any combination of $\gamma$, $P_0$, $T_0$ and $\beta_2$ that give raise to the same number N will have the pulse experiment the same behavior and effects. As the pulse propagates, it is perturbed by higher order dispersive and nonlinear terms, eventually these perturbations break up the pulse into its constituent solitons, the phenomenon called solition fission. The perturbation of the third order dispersion term (TOD) to the travelling pulse gives as a result an energy transfer to a dispersive wave (DW)

even if only the fundamental soliton is present. The frequency of this DW is determined by a phase matching condition, this kind of radiation is also known as Cherenkov radiation [12]. The phase matching condition is that both dispersive wave and soliton must propagate at the same phase velocity, fulfilling the following:

$$\beta(\omega) = \beta(\omega_s) + \beta_1(\omega - \omega_s) + \frac{1}{2}\gamma P_s \tag{3-36}$$

Expanding $\beta(\omega)$ in a Taylor series around the soliton frequency $\omega_s$, one obtains: [13]

$$\sum_{m=2}^{\infty} \frac{\beta_m(\omega_s)}{m!}(\omega_d - \omega_s)^m = \frac{1}{2}\gamma p_s \tag{3-37}$$

where $P_s$ is the peak power of the fundamental soliton. Taking terms up to third order the phase matching is then given by:

$$\Omega_d \approx -\frac{3\beta_2}{\beta_3} + \frac{\gamma P_0 \beta_3}{3\beta_2^2} \tag{3-38}$$

Based on the given phase matching, it is possible to obtain the radiation frequency and relative power of the DW:

$$\Delta\upsilon_d T_0 \approx \frac{1}{4\pi\delta_3}[1 + 4\delta_3^2(2N-1)^2] \tag{3-39}$$

$$\rho_d = \frac{P_d}{P_0} \approx (\frac{5\pi N}{4\delta_3})^2[1 - \frac{2\pi}{5}(2N-1)\delta_3]^2 exp(-\frac{\pi}{2(2N-1)\delta_3}) \tag{3-40}$$

where the normalized dispersion parameter is defined as:

$$\delta_m = \frac{\beta_m}{m! T_0^{m-2}|\beta_2|} \tag{3-41}$$

In Fig.**3-3** the spatial evolution of the spectrum is presented with $N = 2$ for two different cases: when no higher order dispersion terms are considered $\delta_m = 0$ and when the TOD is considered $\delta_3 = 0.03$:

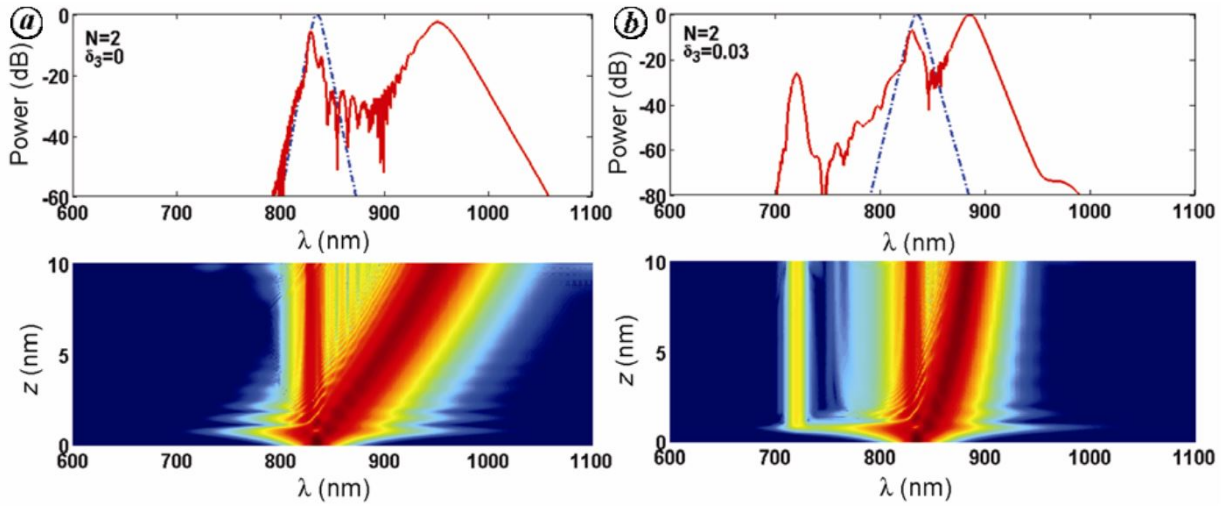


**Figure 3-3**.: **a.**Spectrum soliton ($N = 2$) in the absence of dispersive terms at 10 m propagation distance. **b.**Spectrum with $\delta_3 = 0.03$. [13]

### 3.1.11. Intrapulse Raman Scattering

The main influence of the Raman-induced frequency shift (RIFS) term can be seen over the dispersive wave generation, where a DW is generated at the same frequency and spatial propagation, nevertheless it presents a much lower amplitude. This is a good indicator that the DW is generated before the Raman term starts to act, but its effects are observed over the power distribution, where other waves are shifted towards red spectral components.

### 3.1.12. Four Wave Mixing

Four wave mixing is one of the most important third-order parametric processes in spectral broadening phenomena. It is a process where three frequencies, under phase matching condition, interact in a Kerr medium leading to the generation of a fourth frequency. In the case where all frequencies are equal, then a third harmonic is generated with $\omega_{FWM} = 3\omega$. Parametric processes are those in which optical waveguides play a passive role, there is no interaction with the propagating media that induces changes in its quantum states. The medium only mediates interaction among optical waves, they require phase-matching before they can build up along the waveguide. There are several techniques to achieve phase-matching in optical fibers: either through the use of physical mechanisms, multimode fibers or single mode fibers. The last method presents different regimes where the phase matching can be achieved, in this thesis the phase matching due to self phase modulation will be

considered: in this case the pump wavelength lies in the anomalous GVD regime and the material contribution surpasses the wave contribution significantly, nevertheless as the material and wave contribution are negative, it is possible to compensate this by the nonlinear contribution. Under this view, the phase matching occurs when:

$$\Omega_s = (\frac{2\gamma P_0}{|\beta_2|})^{1/2} \tag{3-42}$$

Thus, a pump wave would develop sidebands at $\omega_1 \pm \Omega_s$, where the lower wavelength generated is known as anti-Stokes band and the higher as Stokes band. In the case of microstructured fibers, higher order dispersive effects become important and must be considered. It has been found that even orders also affect the phase matching condition. Considering all orders of dispersion, the phase matching condition can be written as:

$$\sum_{m=2,4,\ldots}^{\infty} \frac{\beta_m(\omega_p)}{m!}\Omega_s^m + 2\gamma P_0 = 0 \tag{3-43}$$

where $\Omega_s = \omega_s - \omega_p$ is the shift of the signal frequency from the pump frequency $\omega_p$. in anomalous dispersion regime, the $m = 2$ term dominates and the frequency shift is given by equation 3-42.

### 3.1.13. Supercontinuum generation

When an optical pulse propagates inside a highly nonlinear fiber, its temporal as well as its spectral evolution are affected by both nonlinear and dispersive effects. For intense enough pulses the pulse spectrum becomes so broad that it may extend over a wide range of frequencies due to both nonlinear effects seen before being able to take place. Such extreme spectral broadening, it is referred to as *Supercontinuum generation*(SCG). The parameter N defined in eq3-31 is a good indicator of the supercontinuum process, it has found out that if $N$ is relatively large ($N > 10$) the phenomenon of soliton fission can produce a supercontinuum. One critical criterion to obtain SCG is the choice of pump wavelength, this must be close to the Zero dispersion wavelength (ZDW), more precisely where $\beta_2 < 0$. Much research about SCG has been done with different pulse widths, pump wavelengths, fiber geometries and infiltrated materials as organic liquids or noble gases that present different dispersive properties [16][17] [18][19][20].

## 3.2. Z-scan

The measurement of third order nonlinear susceptibility $\chi^3$, nonlinear refractive index $n_2$ and nonlinear absorption coefficient $\beta_2$ is an important matter for their use in different fields. Different techniques have been developed to achieve this task, among them: nonlinear elliptical polarization method, the interference method and the beam-deflection technique [21]. Most of these methods require two light beams and can not directly measure the real and imaginary part of the susceptibility. The Z-scan technique was invented at the end of the eighties as an alternative as it is based on the self-focusing phenomenon. The real and imaginary parts of $\chi^3$ can be obtained with only one light beam. Besides this, it is possible to extract the nonlinear refractive index, its sign, and the nonlinear absorption coefficient with a single optical set up.

### 3.2.1. The Z-scan technique

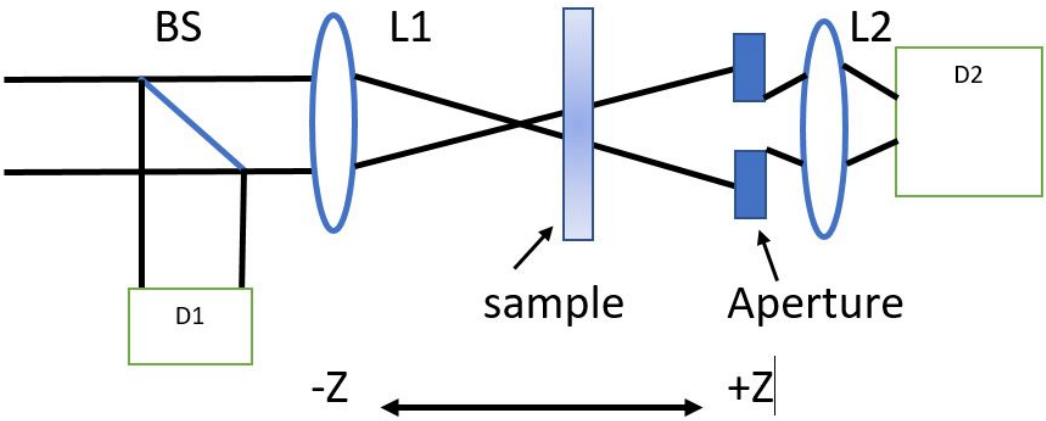


**Figure 3-4**.: Z-scan set-up, the light comes from left to right. D1: reference detector. BS: beam splitter. L1: Lens to focus into sample. L2: Lens to focus into detector. D2: transmittance detector.

Using a single-mode Gaussian beam, the transmittance is measured in the far field after the light passes the sample, as shown in Fig3-4. The sample's position is varied between

an aperture and the detector. Assuming a thickness sample smaller than the diffraction length of the focused beam, this setup can be seen as a thin lens of variable focal length. The scan starts from negative Z, because of the low irradiance nonlinear phenomena are excited negligibly and, as a consequence, $D2/D1$ remains relatively constant. As the sample is moved towards positive Z, when it gets close to the focal point of the lens, the beam irradiance increases giving as a result an excitation of nonlinear phenomena and leading to self lensing in the sample. There are two possible material responses: one is where as the sample is brought closer to the focus a negative self-lensing tends to collimate the beam causing an increase in the transmittance and after the sample passes the focal plane to the right, the same negative self-defocusing increases the beam divergence, leading to beam broadening at the aperture and a decrease in transmittance. This case corresponds to a negative $n_2$. The second kind of response occurs when there is a self-defocusing prior to the focus leading to a decrease in transmittance followed by an increase after the focal plane, this indicates a positive $n_2$. In the above case and in the Fig**3-5** only refractive nonlinearity was considered assuming that no absorptive nonlinearities are present. In case that multiphoton absorption is present the response peak is suppressed and the valley is enhanced, while saturation produces the opposite effect.

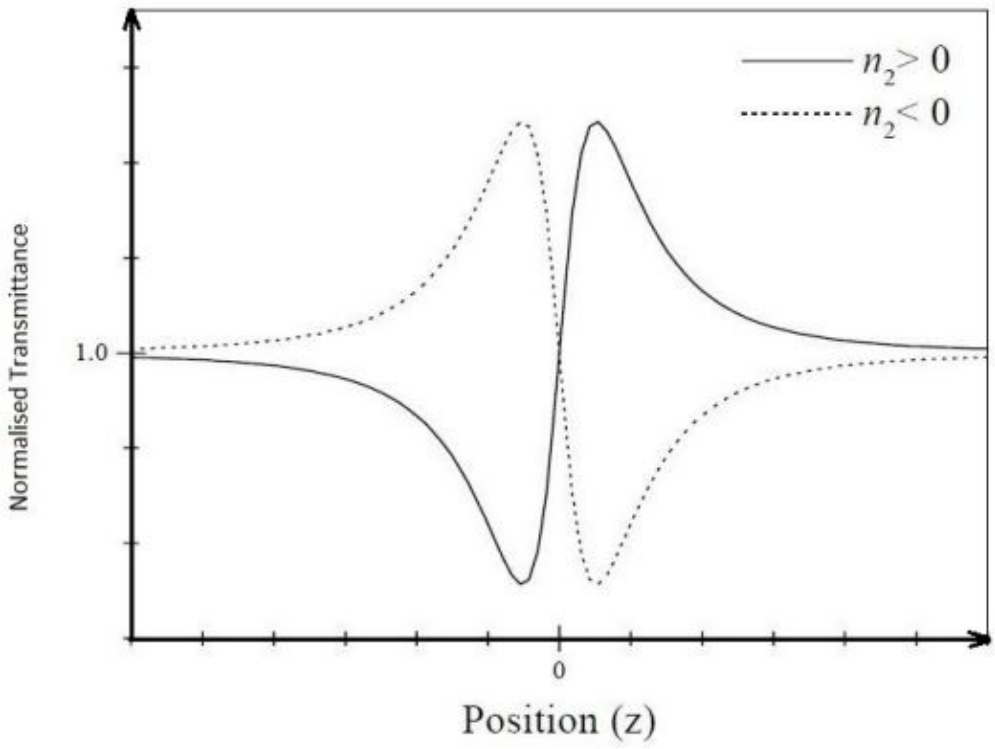


**Figure 3-5**.: Z-scan traces for negative and positive nonlinear refractive indexes

In case of purely nonlinear absorption the experiment is performed in open aperture,

$$\alpha(z,r) = \alpha_0 + \beta I(z,r) \tag{3-44}$$

where $\alpha_0$ is the linear absorption and $\beta$ is the nonlinear absorption coefficient. There are two different cases for $\beta$. When $\beta < 0$, it is saturable absorption, the transmittance curve is a symmetrical peak with center at the focal point. For $\beta > 0$, we have reverse saturable absorption or two photon absorption, in this case the trace has a symmetrical valley centered at the focal point position.

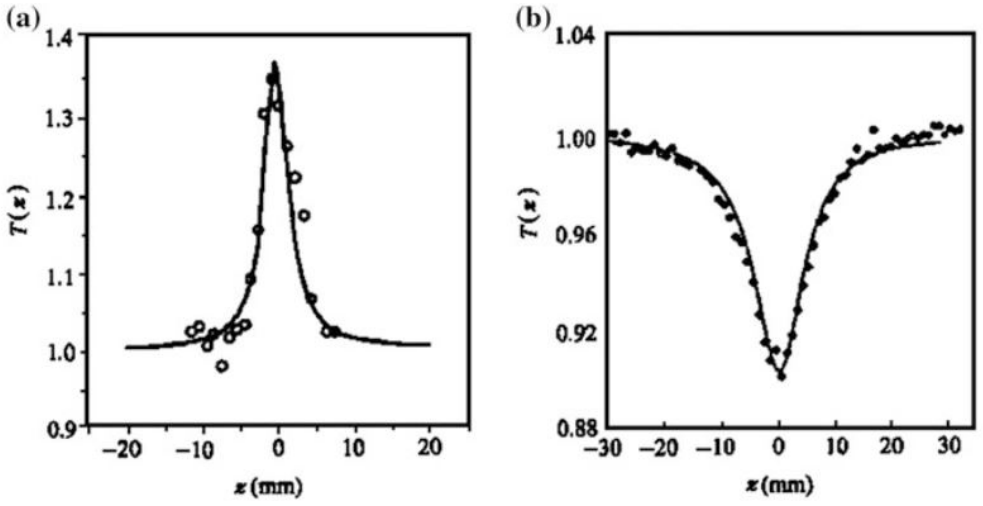


**Figure 3-6**.: Example of positive and negative $\beta$ in a $2.7mm$ thick ZnSe sample. Taken from [8]. (a) Saturable absorption $\beta < 0$. (b) Two photon absorption $\beta > 0$

### 3.2.2. Theory

Considering cubic nonlinearity, the total refractive index is given by:

$$n = n_0 + \frac{n_2}{2}|E|^2 = n_0 + \gamma I \tag{3-45}$$

where $E$ is the peak electric field (cgs) and $I$ is the irradiance (MKS) of the laser beam within the sample. If $E$ is a Gaussian beam with waist radius $w_0$ propagating along the +Z direction, the optical field amplitude can be expressed as:

$$E(z,r,t) = E_0(t)\frac{w_0}{w(z)}exp(-\frac{r^2}{w^2(z)} - \frac{ikr^2}{2R(z)})e^{-i\phi(z,t)} \tag{3-46}$$

where $w(z) = w_0^2(1 + (z/z_0)^2)$ is the beam radius at z position, $R(z) = z(1 + (z/z_0)^2)$ is the radius of curvature of the wavefront at z, $z_0 = kw_0^2/2$ is the diffraction length of the beam, $k = 2\pi/\lambda$ is the wave vector and $\lambda$ is the laser wavelength, all in free space. $E_0(t)$ is the light electric field at the focal plane and contains the temporal envelope of the light pulse. $e^{-i\phi(z,t)}$ contains all the radially uniform phase variations, obtained by making use of the slowly varying envelope approximation (SVEA) where the main interest is the calculation of the radial phase variation $\Delta\phi(r)$. In a thin medium, where the sample length is small enough that changes in the beam diameter within the sample can be neglected, the self-refraction process is referred to as external self-action. This condition means $L << z_0$, where $L$ is the sample length.
The amplitude and phase of the electric field are thus governed by the pair of equations:

$$\frac{\mathrm{d}\Delta\phi}{\mathrm{d}z'} = \Delta n(I)k \tag{3-47}$$

$$\frac{\mathrm{d}I}{\mathrm{d}z'} = -\alpha(I)I \tag{3-48}$$

where $z'$ is the propagation depth in the sample. Neglecting nonlinear absorption, equations 3-47 and 3-48 are solved to give the phase shift at the exit surface of the sample:

$$\Delta\phi(z, r, t) = \Delta\phi_0(z, t)exp(-\frac{2r^2}{w^2(z)}) \tag{3-49}$$

With

$$\Delta\phi_0(z, t) = \frac{\Delta\Phi_0(t)}{1 + (z/z_0)^2} \tag{3-50}$$

where $\Delta\Phi_0(t)$ is the wavefront change in the sample at the focal point and

$$\Delta\Phi_0(t) = k\Delta n_0(t)L_{eff} = kn_2I_0(t)L_{eff} \tag{3-51}$$

where $L_{eff}$ is the sample length, given by $L_{eff} = (1 - e^{-\alpha L})/\alpha$. In case there is no linear absorption present, we have $L_{eff} = L$.
The complex electric field leaving the sample, $E_e$, now contains the nonlinear phase distortions described as:

$$E_e(r, z, t) = E(r, z, t)e^{-\alpha L/2}e^{i\Delta\phi(r,z,t)} \tag{3-52}$$

Using the Gaussian decomposition (GD) method [27], the electric field at the exit plane is decomposed into a summation of Gaussian beams through a Taylor series expansion of the $e^{i\Delta\phi(r,z,t)}$ term. According to Huygens principle, each Gaussian beam can be propagated to

the aperture plane where they will reconstruct the beam. The resultant electric field at the aperture is:

$$E_a(z,r,t) = E(z,r=0,t)e^{-\alpha L/2}\sum_{m=0}^{\infty}\frac{[i\Delta\phi_0(z,t)]^m}{m!}\frac{w_{m0}}{w_m}exp(-\frac{r^2}{w_m^2}-\frac{ikr^2}{2R_m}+i\theta_m) \tag{3-53}$$

Defining $d$ as the propagating distance in free space from the sample to the aperture plane and $g = 1 + d/R(z)$, then each parameter in 3-53 becomes:

$$w_{m0}^2 = \frac{w^2(z)}{2m+1} \tag{3-54}$$

$$w_m^2 = w_{m0}^2[g^2 + (\frac{d}{d_m})^2] \tag{3-55}$$

$$d_m = \frac{kw_{m0}^2}{2} \tag{3-56}$$

$$R_m = d[1 - \frac{g}{g^2 + (d/d_m)^2}]^{-1} \tag{3-57}$$

$$\theta_m = tan^{-1}[\frac{d/d_m}{g}] \tag{3-58}$$

The transmitted power passing throw the aperture is obtained by spatially integrating $E_a(z,r,t)$ up to the cross section of the aperture radius $r_a$:

$$P_T(z,\Delta\Phi_0(t)) = c\varepsilon_0 n_0 \pi\int_0^{r_a}|E_a(z,r,t)|^2 r dr \tag{3-59}$$

Taking into account the time variation of light pulse power, the normalized transmittance is thus:

$$T(z) = \frac{\int_{-\infty}^{\infty}P_T(z,\Delta\Phi(t))dt}{S\int_{-\infty}^{\infty}P_I(t)dt} \tag{3-60}$$

where $P_I(t) = \pi w_0^2 I_0(t)/2$ is the instantaneous input power (within the sample) and $S = 1 - exp(-2r_a^2/w_a^2)$ is the aperture linear transmittance. With $w_a$ denoting the beam radius at the aperture in the linear regime. For small $|\Delta\Phi_0|$, the peak and valley occur at the same distance with respect to the focal point of the lens.

The transmittance can be expressed approximately by setting $r = 0$ and $\Delta\Phi(t) << 1$, where the far field condition is fulfilled, in equation 3-53. Only two terms are retained, yielding the expression:

$$T(z,\Delta\Phi_0) = 1 - \frac{4\Delta\Phi_0(t)x}{(x^2+9)(x^2+1)} \tag{3-61}$$

where $x = z/z_0$. Defining $\Delta T_{p-v}$ as the difference peak valley in the transmittance, it is possible obtain the nonlinear refractive index from $\Delta T_{p-v}$. When the aperture is almost closed ($S \approx 0$):

$$\Delta T_{p-v} \approx 0.406|\Delta\Phi_0| \tag{3-62}$$

obtaining an expression for the nonlinear refractive index:

$$\Delta n \approx \frac{\Delta T_{p-v}}{0.406 k L_{eff}} \tag{3-63}$$

if the aperture in opened, but the phase changes at focal point is $|\Delta\Phi_0 \leq \pi|$:

$$\Delta T_{p-v} \approx 0.406(1-S)^{0.25}|\Delta\Phi_0| \tag{3-64}$$

and the nonlinear refractive index

$$\Delta n \approx \frac{\Delta T_{p-v}}{0.406(1-S)^{0.25} k L_{eff}} \tag{3-65}$$

### 3.2.3. Nonlinear absorption in open aperture

The third order susceptibility is considered now to be a complex quantity, where the imaginary part is related to the nonlinear absorption coefficient $\beta$. We start by expressing the total absorption as:

$$\alpha(I) = \alpha_0 + \Delta\alpha = \alpha_0 + \beta I \tag{3-66}$$

according to this, the light intensity distribution and phase shift at the output surface sample would then be:

$$I_e = \frac{I_0(r,z,t)exp[-\alpha L]}{1+q(z,r,t)} \tag{3-67}$$

and

$$\Delta\phi(z,r,t) = \frac{k\gamma}{\beta} ln[1+q(z,r,t)] \tag{3-68}$$

where $q(z,r,t) = \beta I(z,r,t) L_{eff}$. The complex field amplitude at the surface of the sample after propagation through it would be:

$$E_e = E(z,r,t)e^{-\alpha L/2}(1+q)^{ik\gamma/\beta - 1/2} \tag{3-69}$$

Where $ik\gamma/\beta$ is the ratio between the real and imaginary parts of the third order susceptibility, so the nonlinear absorption and nonlinear refractive index both make a contribution to the far field wavefront variation and transmittance. For $|q < 1|$, following a binomial series

expansion in powers of $q$, Eq.3-69 can be expressed as an infinite sum of Gaussian beams as follows:

$$E_e = E(z,r,t)e^{-\alpha L/2}\sum_{m=0}^{\infty}\frac{q(z,r,t)^m}{m!}[\prod_{n=0}(ik\gamma/\beta - 1/2 - n + 1)] \tag{3-70}$$

When the aperture is removed, the Z-scan becomes insensitive to beam distortions and is only a function of the nonlinear absorption (i.e. $S = 1$). The transmitted power can be obtained by a spatial integral of the beam cross section power:

$$P(z,t) = P_i(t)e^{-\alpha L}\frac{ln[1+q_0(z,t)]}{q_0(z,t)} \tag{3-71}$$

Where $P_i(t)$ is the input power and $q_0(z,t) = \beta I_0(t)L_{eff}/(1+(z/z_0)^2)$. For a temporal Gaussian pulse, Eq3-71 can be time integrated to give the normalized energy transmittance:

$$T(z,S=1) = \frac{1}{\sqrt{\pi}q_0(z,0)}\int_{-\infty}^{\infty} ln[1+q_0(z,0)e^{-\tau^2}]d\tau \tag{3-72}$$

When $|q_0 < 1|$, the transmittance can be expressed in terms of the peak irradiance:

$$T(z,S=1) = \sum_{m=0}^{\infty}\frac{[-q_0(z,0)]^m}{(m+1)^{3/2}} \tag{3-73}$$

In open aperture (i.e. $S = 1$) the transmittance can be taken from the first order approximation of Eq3-73 and simplified to obtain:

$$T(z) = 1 - \frac{q_0(z,0)}{2\sqrt{2}} \tag{3-74}$$

From Eq3-74 and making use of $q_0(z,0)$, the nonlinear absorption coefficient approximation expression is obtained:

$$\beta = \frac{2^{3/2}[1-T(0)]}{I(0)L_{eff}} \tag{3-75}$$

Where $T(0)$ is the open aperture transmittance for $S = 1$ at $z = 0$:

## 3.3. Photonic Crystal Fibers

Photonic crystal fibers (PCFs) are a class of optical fibers based on the properties of photonic crystals. They employ a microstructured material arrangement of different refractive indexes that has the ability to confine light. PCFs are divided in two categories: high index guiding fibers and low index guiding fibers. The first type guide light in a solid core by the modified total internal reflection (M-TIR) principle. Low index guiding fibers, also known as photonic-bandgap fibers, instead guide light by the photonic bandgap (PBG) effect [28]. PCFs led to increased versatility in nonlinear optical research as their dispersion and nonlinearity properties are of special interest.

### 3.3.1. Hollow-Core Photonic Crystal Fibers

Hollow core fibers (HCPCF) are a special class of PBG guiding fibers, where the core is created by introducing a defect in the PBG structure, thereby creating an area where the light can propagate, in the case of HCPCF the field is confined to an air-filled core. Furthermore, the fact that the core can be filled by gas or liquid opens the possibility to change its waveguide properties on the fly, this cannot be made in TIR fibers because the refractive index of gases is very close to that of air. Among the most notable properties found in HCPCF we have: high power delivery, potential for gas sensing, low loss in vacuum, ultra long single-mode interaction lengths (of 10 or even 1000 meters) and near insensitivity to bending effects [2] [28] [30].

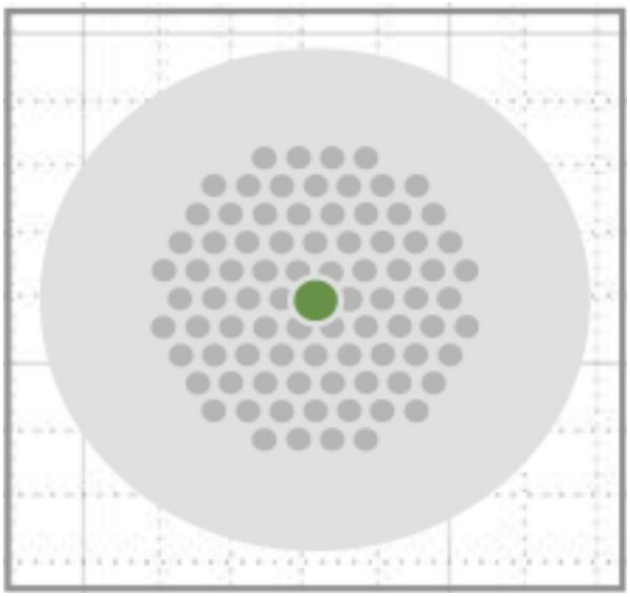

**Figure 3-7**.: Photonic Band Gap HC-PCF geometry used in this thesis.

HCPCF have restricted transmission wavelength windows. Filling the fiber's holes with gases or liquids can shift these transmission windows. This kind of fiber enables for example the creation of controlled plasma generation [29]. Between the major attractions of a gaseous core, in contrast with solid core fiber, is that the nonlinearity and the group velocity dispersion (GVD) can be varied by changing the gas pressure, making it possible to shift the ZDW ranging from UV to near IR.

The most common structure of HCPCF is formed by a hexagonal lattice of holes in the center of the fiber, surrounding a central hollow core. This arrangement guides a tightly confined single mode over a restricted spectral range (low loss propagation). The GVD of HCPCF filled with air has a steep slope, passing through zero inside the transmission windows, but this spectral shape can be changed when air is replaced by a gas or liquid. In this thesis the core was filled with $CS_2$, Xenon, Argon and Krypton. In Fig**3-8** the results of finite element modeling (FEM) calculation are presented for a structure designed to operate around a wavelength of 800nm. The limited transmission windows and extreme dispersion slope prevent application in extreme ultrafast experiments.

There is a second common type of HC-PCF, which has a Kagome-lattice cladding, characterized by a star of David-shaped pattern of glass webs. This kind of fiber provides ultrabroadband guidance at loss levels, of $\sim$ 1 dB/m, and anomalous GVD over the entire transmission window with a low dispersion slope. For the reasons mentioned above, Kagome fiber has been studied extensively, including the infiltration with gases and how it changes the nonlinear and dispersion properties with pressure [9] [30] [10].

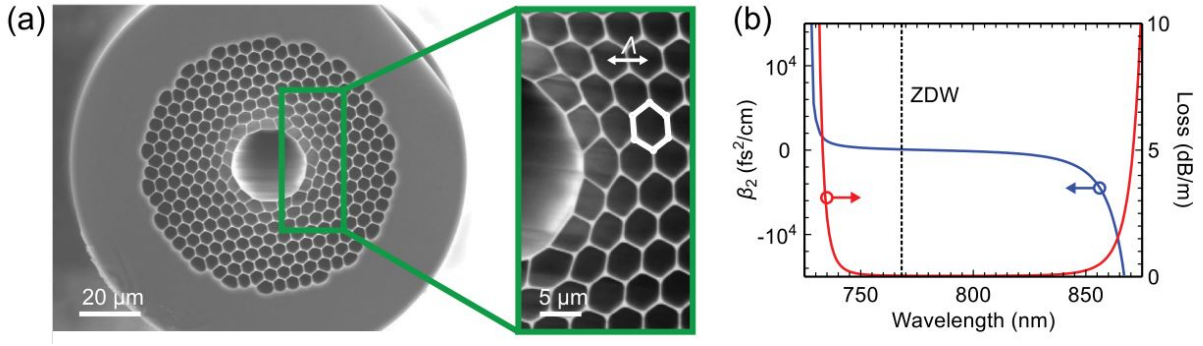


**Figure 3-8**.: Example of a HC-PCF. (a) Scanning electron micrographs (SEMs). (b) GVD and loss calculated using finite-element modeling (FEM) of an idealized HCPCF structure. [30]

### 3.3.2. Negative Curvature Hollow Core Fiber

A hollow core fiber with negative curvature of its core boundary exhibits lower attenuation than PBG HC-PCF. This was discovered first in 2010 by Y.Y.Wang et al. analyzing the curvature of the core boundary in HC-PCF. After that, it was demonstrated that the cladding structure had negligible effects on the losses of Kagome fiber. Negative curvature hollow core fibers consist on an array of capillaries, which can be in contact or not, non-touching capillaries can reduce the confinement loss compared to touching capillaries. The hollow space formed by the capillaries creates the core of the fiber, where the light is confined. Different parameters can affect the fiber properties: capillaries thickness, whether they are in contact or now, outer fiber diameter and capillariy diameter, which also determines the core diameter.Fig **3-9**(a) shows the main characteristics of NHCPCF, where the number $N$ makes reference to the number of capillaries forming the structure. When gas infiltration is performed, $D_{core}$ is the only part of the structure filled. In this thesis we considered 3 different gases: Krypton, Xenon and Argon all at 1 Bar, 25 Bar, 90 Bar and 140 Bar, using different input powers, pulse widths and propagation lengths.
Different works have been developed to calculate the loss (dB/m), among them [31] [32] where the range of analysis goes from $2\mu m$ up to $9\mu m$, including the fundamental mode as well as higher order ones. Furthermore, in [31] a loss analysis in function of capillary thickness was made.

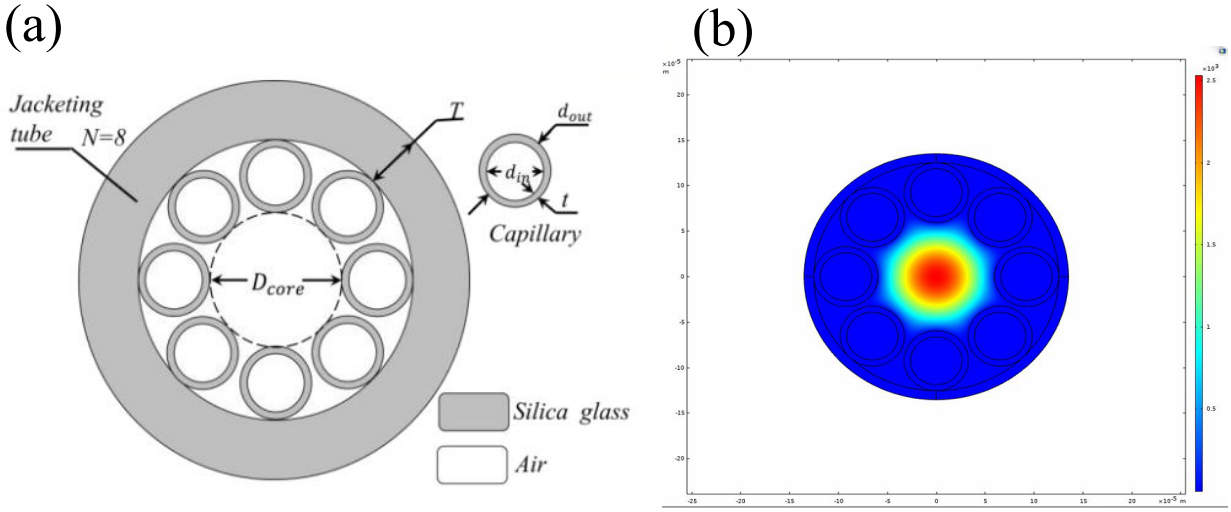


**Figure 3-9**.: (a)Cross section of NCHCPF, taked from [31]. (b) Fundamental mode of NCHCPCF resolved by FEM, in Krypton at 1 bar.

## 3.4. From analytical solution to numerical methods

NLS equation 3-21 is a nonlinear partial differential equation that generally cannot be solved analytically, except for some specific cases in which the inverse scattering method can be employed. In this way, a numerical approach is necessary to know its solution. Numerical methods can be classified in two categories: finite-difference and pseudospectral methods. The most used method to solve the GNLSE is the *split-step Fourier method*. In this thesis two different codes have been implemented: the first was used the Split-step Fourier method and the second one used the extended Crank-Nicolson method. The main difference between the two is that in the former, the diffraction term is not included (transverse coordinates), but in the latter diffraction is taken into account, making it more robust and computationally expensive. The fast speed at which the split-step method works makes it ideal to use in many propagation problems, mainly in fiber propagation where diffraction can be neglected. When free space propagation is considered, diffraction plays a important role at the final output pulse, in this case a complete scheme must be considered.

### 3.4.1. Split-Step Fourier Method

We start by approximating the Eq.3-21 to

$$\frac{\partial A}{\partial z}+\frac{\alpha}{2}+\frac{i\beta_2}{2}\frac{\partial^2 A}{\partial T^2}-\frac{\beta_3}{6}\frac{\partial^3 A}{\partial T^3}=i\gamma(|A|^2A+\frac{i}{\omega_0}\frac{\partial}{\partial T}(|A|^2A)-T_RA\frac{\partial|A|^2}{\partial T}) \tag{3-76}$$

where $T_R \equiv \int_0^\infty tR(t)dt \approx f_R\int_0^\infty th_R(t)dt$.
To implement the Split-Step method. it is useful to write Eq3-76 in the form:

$$\frac{\partial A}{\partial z}=(\hat{D}+\hat{N})A \tag{3-77}$$

where $\hat{D}$ is the differential operator which accounts for dispersion and losses within a linear medium and $\hat{N}$ is a nonlinear operator, that represents the nonlinear phenomena included in the propagation. These operators are described as:

$$\hat{D}=-i\sum_{n=1}^{\infty}\frac{i^n\beta_n}{n!}\frac{\partial^n A}{\partial t^n}-\frac{\alpha}{2} \tag{3-78}$$

$$\hat{N}=i\gamma(|A|^2A+\frac{i}{\omega_0}\frac{\partial}{\partial T}(|A|^2A)-T_RA\frac{\partial|A|^2}{\partial T}) \tag{3-79}$$

The split-Step method obtains an approximate solution by supposing that in a small propagating distance h, the dispersive and nonlinear effects act independently. In this way, a

propagation from z to z+h acts in two steps: first the nonlinearity acts alone ($\hat{D} = 0$), in the second step only dispersion acts and nonlinearity is ignored ($\hat{N} = 0$). Expressed mathematically:

$$A(z+h,T) \approx exp(h\hat{D})exp(h\hat{N})A(z,T) \tag{3-80}$$

The exponential operator $exp(h\hat{D})$ can be evaluated in the Fourier domain as:

$$exp(h\hat{D})B(z,T) = F_T^{-1}exp[h\hat{D}(-i\omega)]F_T B(z,T) \tag{3-81}$$

where $F_T^{-1}$ denotes the inverse Fourier transform. The use of FFT algorithms makes the Split-Step method faster by up two orders of magnitude compared with most finite-difference schemes [2].
The Split-Step method ignores the non-commuting nature of the operator $\hat{D}$ and $\hat{N}$. Thus, it is accurate up to the second order of the step size h.

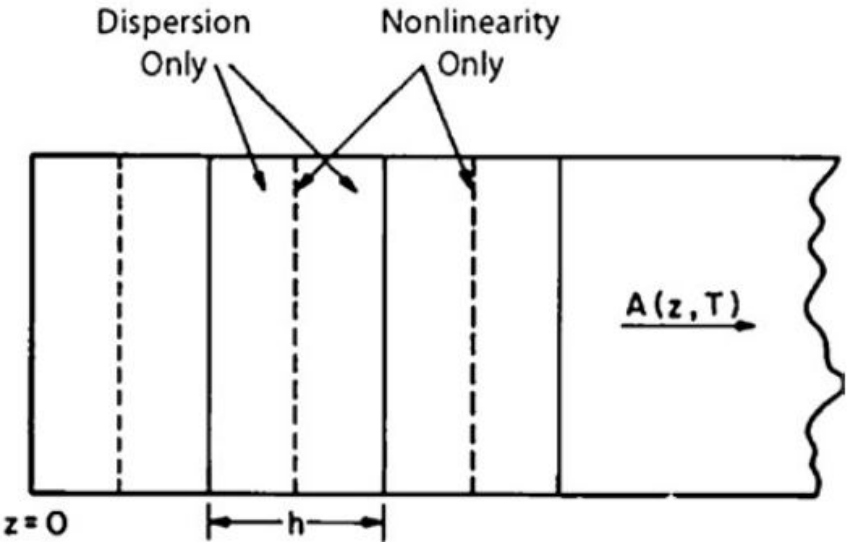


**Figure 3-10**.: Illustration of the Split-Step method used for numerical simulations. Fiber length is subdivided into a number of segments of width $h$, where nonlinearity acts at the middle, $h/2$ (dashed line), and dispersion at the boundaries (continuous line). From [2]

The implementation of the Split-Step method consists in the division of the fiber length in segments that need not be spaced equally. The optical field is propagated until a distance of half of a given section length $h$ with only dispersion terms taken into account, using Eq3-81.

After that, the field is multiplied by a nonlinear term that represents the effect of nonlinearity over the whole segment $h$. Finally, the field is propagated the remaining $h/2$ distance with dispersion only to obtain A(z+h,T). This same procedure is repeated throughout the entire propagation distance. Although its implementation is very straightforward, it requires a careful selection of the step sizes in Z and T to maintain the required accuracy. The use of FFT imposes periodic boundary conditions, which gives the requirement that the temporal windows be much wider than the pulse width, typically 10 to 20 times wider. In [17] a complete review of supercontinuum generation can be found, where they address numerical calculation issues, such as temporal and spectral windows, number of discretization points and their relationship with the pulse width.

### 3.4.2. Envelope Propagation Model

This model considers the paraxial envelope equation, where the proposed method for this kind of equations can be extended to paraxial carrier-resolving equation. First, the diffraction term will be considered and then one by one all terms of GNLSE will be added, including dispersive and nonlinear terms.
Working in cylindrical symmetry around the propagation axis, let $E$ denote the envelope $E(r, z, t)$, where the laser field has a carrier frequency $\omega_0$ and wavenumber $k_0 = k(\omega_0)$. The propagation equation reads then [33]:

$$\kappa\frac{\partial E}{\partial z} = \frac{i}{2}[\Delta_\perp E + D(E)] + k_0[(T^2 N_{kerr}(E)) + TN_{NLL}(E) + N_{plasma}(\rho, E)] \tag{3-82}$$

Where $\Delta_\perp \equiv \partial_r^2 + (1/r)\partial_r$ is the transverse Laplacian, acting only on transverse coordinates. $D$ denotes the operator accounting for all dispersive terms, $N_{kerr}$ and $N_{NLL}$ correspond to kerr effect and nonlinear losses, $N_{plasma}$ makes reference to plasma contributions. $T = 1 + i\omega_0^{-1}\partial/\partial t$ and $\kappa \equiv k_0 + ik_0'\partial/\partial t$

### 3.4.3. Diffraction

Using a monochromatic beam, i.e. laser pulse with central wave number $k_0$ and a narrow spectrum so that all frequency dependencies can be neglected, the paraxial equation from Eq 3-82, neglecting all terms except diffraction, becomes:

$$\frac{\partial E}{\partial z} = \frac{i}{2k_0}\Delta_\perp E \tag{3-83}$$

We start by describing the beam propagation in terms of 1+1 dimensions, i.e. one transverse dimension and one evolution or propagation variable $z$. To solve Eq.3-83 it is necessary to define the boundary equations. As the highest order derivative in Eq.3-83 is of second order, we need two boundary conditions at $r = r_{min}$ and $r = r_{max}$. In cylindrical geometry,beams have generally an intensity distribution with a peak (zero slope) at the origin which vanishes far from the origin, giving the boundary conditions:

$$\frac{\partial E(r, z)}{\partial r}|_{r=0} = 0 \tag{3-84}$$

$$E(r = r_{max}, z) = 0 \tag{3-85}$$

Next, we discretize the transverse coordinate $r$ to form a numerical grid of finite size with $N_\perp + 2$ points, i.e. $N_\perp$ inner points and two boundaries. Using the finite difference method, we the discrete position $r$ and the step size $\Delta r$ as:

$$r_j = r_{min} + j\Delta r \tag{3-86}$$

$$\Delta r = (r_{max} - r_{min})/(N_\perp + 1) \tag{3-87}$$

with $j = 0, 1, 2, ..., N_\perp + 1$. In the case of cylindrical geometry $r_{min} = 0$. A similar discretization is performed in the propagation variable $z$:

$$z_n = n\Delta z \tag{3-88}$$

with $n = 0, 1, 2, ..N_z$ of constant size $\Delta z$. Defining $E_j^n \equiv E(r = r_j, z = z_n)$ we discretize also the evolution operator from 3-83 as:

$$\frac{\partial E}{\partial z}(r = r_j, z = z_n) \approx \frac{E_j^{n+1} - E_j^n}{\Delta z} + O(\Delta z) \tag{3-89}$$

Which is first-order accurate in $\Delta z$. In the same way, a discretization of the second order derivative appearing in the transverse Laplacian, this time second order accurate, yields:

$$\frac{\partial^2 E}{\partial r^2}(r = r_j, z = z_n) \approx \frac{E_{j+1}^n - 2E_j^n + E_{j-1}^n}{\Delta r^2} + O(\Delta r^2) \tag{3-90}$$

*Numerical stability* refers to the condition that a numerical calculation does not amplify truncation or approximation errors. Depending on the calculation scheme, stability may require restrictive conditions on the step sizes in order to be achieved [34].
To solve Eq3-83, there are two types of scheme: explicit and implicit. The explicit scheme has the advantage of allowing the calculation of quantities at each position j on the grid, i.e. $E_j^{n+1}$ explicitly from the previous known quantity $E_j^n$. An implicit scheme requires the resolution of implicit equations coupling $E_j^{n+1}$ with several j positions each with already known quantities, this scheme turns computationally more expensive. However, the explicit scheme requires very restrictive conditions to ensure stability: $\Delta z << k_0 \Delta r^2$. The method used in this thesis to solve Eq 3-83 and the following equations is the Crank-Nicolson method, which corresponds to an explicit method with the advantage that is unconditionally stable and allows to use a large implicit step to advance the solution instead of many small explicit steps.
**Crank-Nicolson method:** This scheme is second-order accurate in both $\Delta r$ and $\Delta z$. Discretizing the diffraction operator as:

$$\Delta_j E_j^n \equiv E_{j-1}^n - 2E_j^n + E_{j+1}^n + \frac{\nu}{2j}(E_{j+1}^n - E_{j-1}^n) \tag{3-91}$$

where $\nu = 1$ for cylindrical geometry and $\Delta_j$ can be represented as a tridiagonal matrix acting on $E_j^n$.
Using the evolution operator Eq.3-89 and Eq.3-91 we obtain the electric field in the next z point:

$$E_j^{n+1} = (1 - i\delta\Delta_j)^{-1}(1 + i\delta\Delta_j)E_j^n \tag{3-92}$$

or equivalently, $E_j^{n+1} = L_-^{-1}L_+E_j^n$, where $\delta = \Delta z/4k_0(\Delta r)^2$

### 3.4.4. Diffraction and Nonlinear terms

Consider now simple nonlinear terms such as instantaneous Kerr and nonlinear losses included in:

$$\frac{\partial E}{\partial z} = \frac{i}{2k}\Delta_\perp E + i\frac{\omega_0}{cn_2}|E|^2E - \frac{\beta_K}{2}|E|^{2K-2}E \tag{3-93}$$

where $\beta_K \equiv K\hbar\omega_0\sigma_K\rho_{nt}$ denotes the cross section for multi-photon absorption. $\rho_{nt}$ is the density of neutral atoms. $\sigma_K$ denotes cross section for multiphoton ionization and $K$ is the number of photons. In order to solve the new terms from Eq. 3-93, the Dufort-Frankel scheme is used, which is an explicit scheme working generally for all types of nonlinear terms. The use of this scheme presents the advantage of preserving the second order accuracy of Crank-Nicolson scheme. It reads:

$$E_j^{n+1} - E_j^n = i\frac{\delta}{2}(\Delta_j E_j^{n+1} + \Delta_j E_j^n) + \frac{3}{2}N_j^n - \frac{1}{2}N_j^{n-1} \tag{3-94}$$

where

$$N_j^n \equiv N(E_j^n) = \Delta z[i\frac{\omega_0}{c}n_2|E_j^n|^2E_j^n - \frac{\beta_K}{2}|E_j^n|^{2K-2}E_j^n] \tag{3-95}$$

Finally, obtaining the electric field in the next propagation step:

$$E_j^{n+1} = (L_-)^{-1}[L_+E_j^n + \frac{3}{2}N(E_j^n) - \frac{1}{2}N(E_j^{n-1})] \tag{3-96}$$

The overall stability of the scheme depends on the nonlinear terms, so that a careful control of the step size $\Delta z$ may be necessary. However, the condition needed for stability associated with the Kerr effect ($\Delta z << c/\omega_0 n_2 I_{max}$) is not so drastic as that of diffraction with the explicit scheme.

### 3.4.5. Diffraction, dispersion and nonlinear effects

Now we add one more dimension: time. The field can then be expressed as $E(r, z, t)$. This new coordinate is discretized as:

$$t_l = t_{min} + l\Delta t \tag{3-97}$$

and in the spectral domain:

$$\omega_l = \omega_0 + l\Delta\omega \tag{3-98}$$

where the temporal coordinate is discretized with $N_t$ equally spaced steps of size $\Delta t$ , for $l = 0, 1, 2, ..., N_t - 1$.

The pulse propagation is described by including each propagation step from the previous scheme in a loop of time for each index $l$. In this way, the discretized pulse envelope at a given propagation distance $z_n$ must be defined over a two dimensional grid as:

$$E^n_{j,l} = E(r = r_j, z = z_n, t = t_l) \tag{3-99}$$

for $j = 0, 1, 2, ..., N_\perp$ and $l = 0, 1, 2, ..., N_t$. As long as the propagation equation does not involve differential operators with respect to time, these are the only additions necessary to extend previous scheme from (1+1) to (2+1) dimensions.
The standard way to extend the Crank-Nicolson scheme to a (2+1)D simulation of paraxial propagation equations is presented. Expressing Eq.3-82 in the spectral domain:

$$\hat{\kappa}\frac{\partial \hat{E}}{\partial z} = \frac{i}{2}[\Delta_\perp \hat{E} + \hat{D}\hat{E}] + k_0[\hat{T}^2\hat{N}_{kerr}(E) + \hat{T}\hat{N}_{NLL}(E) + \hat{N}_{plasma}(\rho, E)] \tag{3-100}$$

The numerical scheme reads as:

$$\hat{E}^{n+1}_{j,l} - \hat{E}^n_{j,l} = i\frac{\delta_j}{2}(\Delta_j \hat{E}^{n+1}_{j,l} + \Delta_j \hat{E}^n_{j,l}) + i\frac{d_l}{2}(\hat{E}^{n+1}_{j,l} + \hat{E}^n_{j,l}) + \frac{3}{2}\hat{N}^n_{j,l} - \frac{1}{2}\hat{N}^{n-1}_{j,l} \tag{3-101}$$

Whose solution, representing one step along the propagation direction, is:

$$\hat{E}^{n+1}_{j,l} = (L_{-,l})^{-1}[L_{+,l}\hat{E}^n_{j,l} + \frac{3}{2}\hat{N}^n_{j,l} - \frac{1}{2}\hat{N}^{n-1}_{j,l}] \tag{3-102}$$

with:

$$L_{-,l} \equiv 1 - i(\delta_j/2)\Delta_j - i(d_l/2) \tag{3-103}$$
$$L_{+,l} \equiv 1 + i(\delta_j/2)\Delta_j + i(d_l/2) \tag{3-104}$$

In table **3-4** one can find the parameters necessary to simulate the final pulse envelope according to the extended Crank-Nicolson scheme.

**Table 3-4**.: Parameters needed to simulate Eq. 3-102

| **Parameter** | **Expression** |
|---|---|
| $\delta_l$ | $\frac{\delta}{\hat{\kappa}_l} = \frac{\Delta z}{2(\Delta r)^2 \hat{\kappa}_l}$ |
| $d_l$ | $\frac{\Delta z \hat{D}_l}{2\hat{\kappa}_l}$ |
| $\hat{\kappa}$ | $k_0 + k_0^{'}(\omega_l - \omega_0)$ |
| $\hat{D}(E)$ | $(k^2(\omega) - \hat{\kappa}^2)\hat{E}$ |
| $\frac{(k^2(\omega)-\hat{\kappa}^2)}{2\hat{\kappa}} \approx$ | $\frac{k_0^{''}(\omega_l-\omega_0)^2}{2!} + \frac{k_0^{'''}(\omega_l-\omega_0)^3}{3!} + ...$ |
| $\hat{N}_{j,l}^n$ | $\frac{k_0 \Delta z}{\hat{\kappa}_l}[\hat{T}_l^2 \hat{N}_{kerr} + \hat{T}_l \hat{N}_{NLL} + \hat{N}_{plasma}]$ |

# 4. Nonlinear parameters measurement

## 4.1. Z-Scan set up

The implementation of the set-up is shown in Fig3-4. A femtosecond Gaussian laser with a wavelength of 780 nm, of variable pulse energy and width is used, as can be seen in table 4-1. The set-up implemented is very similar to the theoretical one, where a beam splitter of 13-87 % was placed to divide the beam: 13 % goes to the reference detector, while the remaining 87 % of energy goes trough a 17 cm focal length lens towards the sample, that is inside a 1 mm thick quartz or glass cuvette, depending on the sample conditions required. The sample is on a mobile computer controlled platform with step resolution of 0.001 $\mu$m. In this way, the sample can be moved along the Z-axis, within our defined +z and -z positions. Once the light goes leave the sample, it propagates a long enough distance to ensure the far field condition, after which an aperture is placed to execute the $n_2$ measurements. Following the aperture there is a second lens of 3.5 cm focal length, it allows to collect all incoming light into the second detector to obtain the final intensity.

**Table 4-1**.: Laser parameters used in the Z-scan set-up

| **CURRENT (A)** | **OUTPUT POWER (mV)** | **PULSE WIDTH (fs)** | **PULSE ENERGY (nJ)** |
|---|---|---|---|
| 3 | 44 | 248 | 0.9 |
| 4 | 114 | 170 | 2.3 |
| 5 | 218 | 107 | 4.4 |
| 6 | 378 | 76 | 7.6 |
| 7.23 | 607 | 51 | 12.1 |

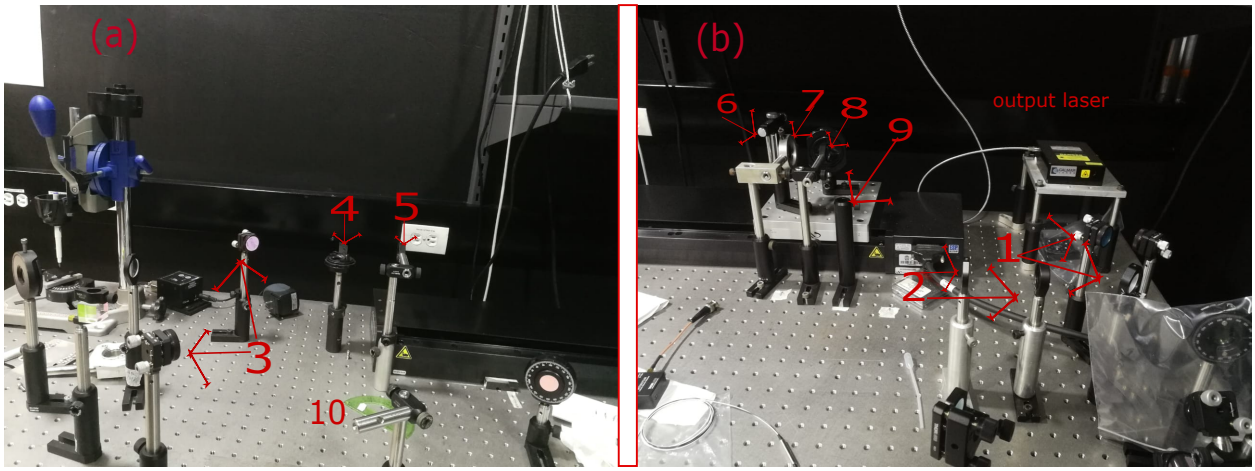


**Figure 4-1**.: Implemented Z-scan set up. (a) 3. Mirrors to change light direction. 4. Beam splitter. 5. Focusing lens. 10. Reference power detector. (b) 1. Mirrors to direct the light. 2. Beam collimator. 6. Cuvette with sample. 7. Aperture. 8. Second lens to focus light into the optical power detector. 9. Transmitted power detector

## 4.2. Control Code

In order to obtain the nonlinear refractive index and the nonlinear absorption coefficient, it is necessary to measure the reference power and final transmittance, as well as control the sample position, plot the normalized transmittance (in real time would be ideal) and calculate the different parameters related to equations 3-61, 3-64 and 3-74. For this purpose, a control code has been developed, which achieves these tasks and is also able to set the step size at which the platform performs its displacement (it may or may not be uniform), the displacement speed and optical parameters such as mirror and lens losses can be tuned to obtain the input energy at the sample.

Fig **4-2** presents the user interface of the developed code. In the left side there is a control column where we have: 1. Transmittance powermeter, 2. Reference powermeter, 3. Optical parameters, such as the initial laser energy and pulse width (according to table **4-1**), wavelength, initial Rayleigh distance ($Z_0$), initial beam waist, focal length of the first lens and propagation distance from the output laser to the first lens, 4. Variables related to the relative position of the platform: home position makes reference to the initial position ($Z = 0$) and path length relative to home position, 5. Command buttons: "Run Z-scan" starts the measurement, "Save As" records the normalized Z-scan trace, "Trash Data" erases

the Z-scan trace and "Fit Data" executes the theoretical fit from the measured data and the available information, 6. Switches between nonlinear refractive index and nonlinear absorption calculation, 7. Indicates when the Z-scan measurement is being executed, 8. In this bar we have the motor controllers and the exit button that ends program execution, 9. "N" is the number of data points that will be measured corresponding to each different Z position, 10. This block controls N, setting the minimum and maximum distances between adjacent points and "NearF" determines the distance around the focus, the number of final points is determined by an equation in which the number of points in "NearF" is finer than the rest of the displacement, 11. In this section there are the different tabs for navigation within the software.

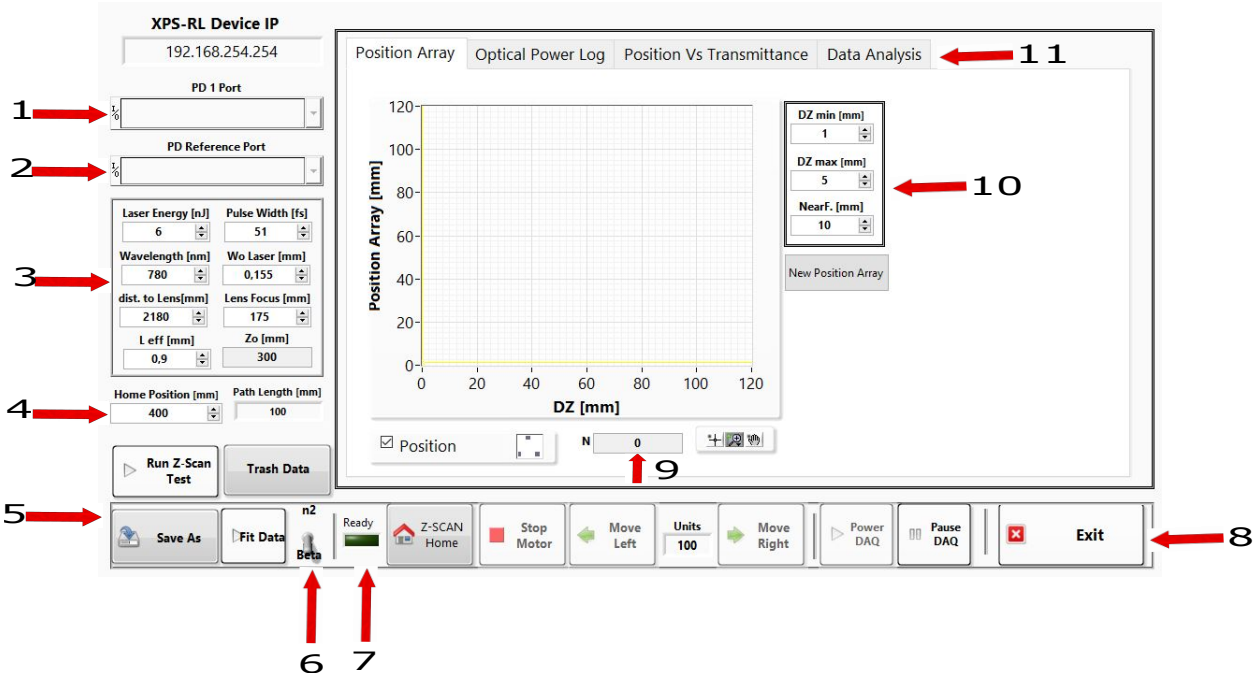


**Figure 4-2**.: Z-scan software implementation: general variables and initial tabs

Fig 4-3 presents the Optical Power Log tab, where the reference and final transmittance powers are displayed, the normalization settings that can be changed are: number of loops (2) and the different beam losses due to Lens transmittance, mirrors, beam splitter and cuvette absorptions or reflections. Besides this, the presence or absence of an aperture ($S$) is taken into account to obtain the final energy that enters the transmittance photodetector (3). These features allow the normalization of the trace and calculation of the real energy arriving at the sample.

The remaining tabs are shown in Fig 4-4, these are "Position Vs Transmittance" and "Data

Analysis". The former displays the recorded transmittance point by point at the different Z-positions, where the ratio between reference and transmittance power is made. Once the measurement is done, the Z-scan traces are saved in the file path shown in the lower part of the tab. The filename includes the aperture ($S$) as well as other parameters relevant to its study. In Fig4-4(b the "Data Analysis tab is presented, where the theoretical fit with respect to the recollected data is shown. It is also where the nonlinear refractive index or nonlinear absorption coefficients are calculated. (4) marks the data plot and its fit, the "Divide" button (5) allows to made the division between closed and open aperture powers to remove absorption phenomena. Some useful values are displayed below this columns such as $\Delta T_{p-v}$, $\Delta\Phi$, $n_2$ and $\beta$. There is also a calibration button, where some laser parameters can be tuned in order to obtain the $n_2$ of a substance and compare it with a known value, this process will be explained in the next section.

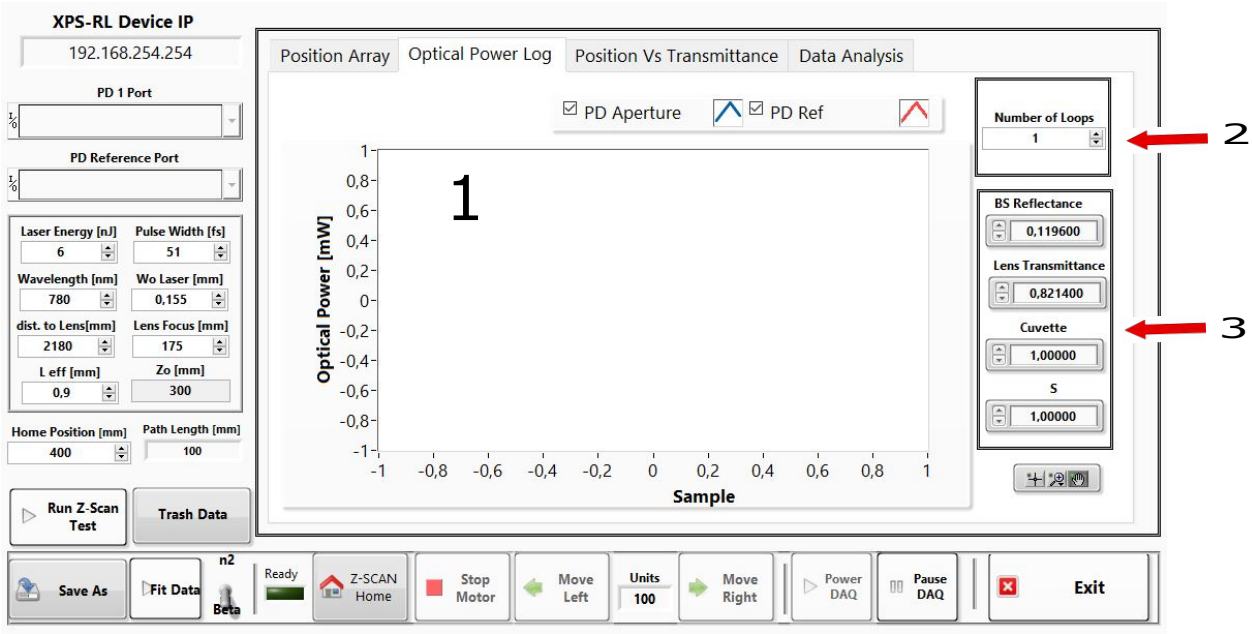


**Figure 4-3**.: Z-scan tab software implementation: Optical power Log and normalization settings

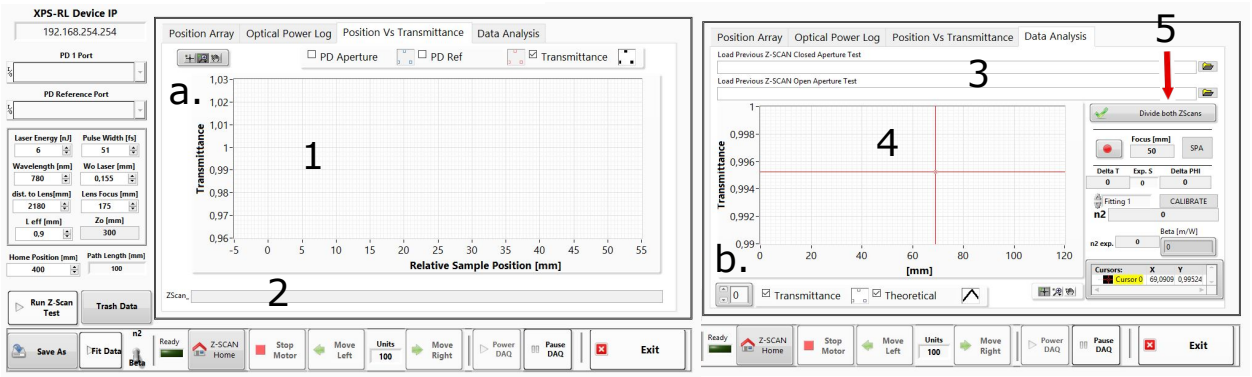


**Figure 4-4**.: Z-scan tab software implementation. (a) 1. Data plot in real time. 2. File path. (b) Data analysis tab: extraction of $n_2$ and $\beta$ as well as laser variables tuning

## 4.3. Calibration

To ensure the correct system operation, it is necessary to know the different variables involved in the calculation of nonlinear refractive index and nonlinear absorption coefficient. These variables are: input Laser energy, pulse width, wavelength, beam waist ($w_0$), lens focus, rayleigh distance ($z_0$). Wavelength and lens focus are relatively easy to obtain and have a low uncertainty as they are supplied by the manufacturer and can be checked with precision. Despite the remaining variables being also supplied by the manufacturer, this information is valid only directly after the laser output, when the beam is propagated through the different optical elements, these values change and at the sample vary from the initial ones. Making it necessary to estimate the new values. The laser energy at the input can be known by subtracting the loses after each optical element from the initial power as done in software (Fig4-3). The pulse width is given by the manufacturer, assuming a short enough propagation distance to neglect pulse broadening or narrowing and low impact from the optical elements, we can use this value in our calculations. The last parameter to calculate is $w_0$, related to $z_0$. Due to equipment constraints, this measurement is performed as follows: knowing the nonlinear refractive index of some substance, in this case $cs_2$, the Z-scan is executed. The corresponding trace is shown in Fig4-5. After this, in the data analysis tab of the software the $w_0$ value can be changed until obtain the $CS_2$ nonlinear index value.

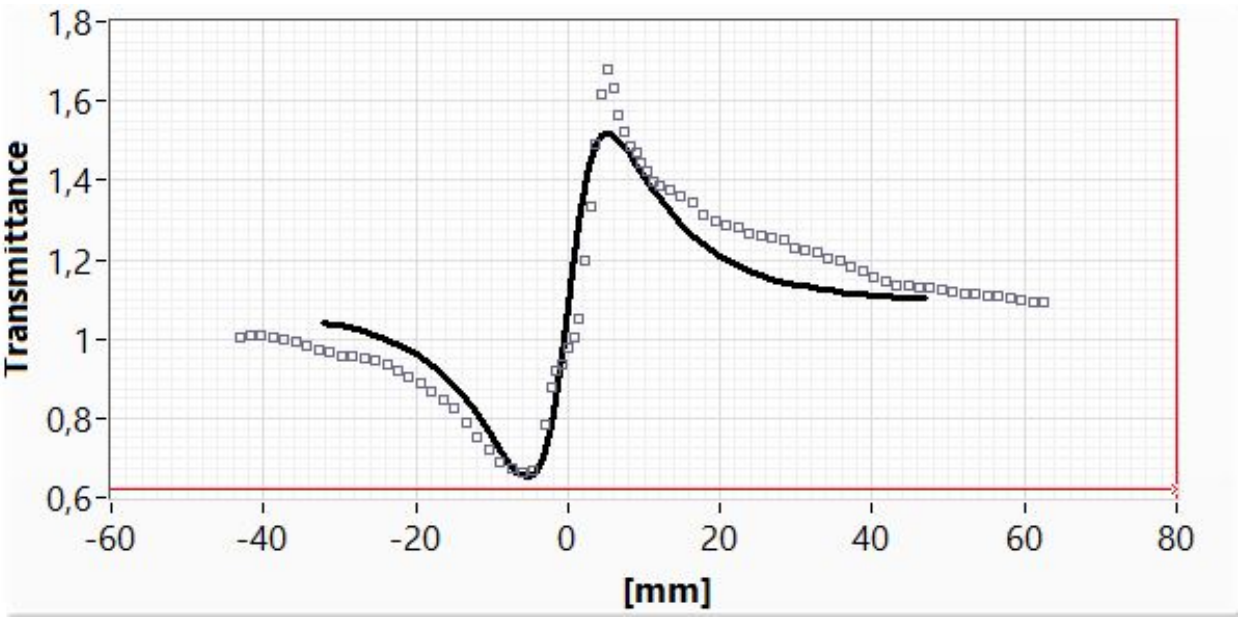


**Figure 4-5**.: $CS_2$ z-scan trace. Doted: experimental. Continuous: theoretical fit.

Its value must be consistent with that reported in literature [21]. Once the beam waist value is obtained, the calibration is corroborated with other known substances as methanol

and ethanol. In this way, the reported value uncertainty is based on a global uncertainty calculated from the difference between the experimental data and the theoretical fit, which is around 20 %.

## 4.4. Measurements

### 4.4.1. carbon disulfide ( $CS_2$ )

Carbon disulfide is a colorless volatile liquid with chemical formula $CS_2$ , with linear refractive index $n = 1.6060$ at 800 nm and a linear molecular shape, heat capacity $C = 75.73$ j/(mol K). $CS_2$ is one of the most widely studied substances [22] [21] (references within) [35] [36] and is commonly used as reference for many measurements and calibrations.
The work done in this thesis was about the study of the $CS_2$ nonlinear refractive index dependence with laser energy and pulse width at 50 MHz of repetition rate. Table**4-1** shows the energy and pulse widths considered. At each laser current four powers were used: 100 %, 69.11 %, 54.27 %, 22.79 %, of the maximum energy listed for their respective current. This was done for keeping the pulse width constant and study the dependence on energy. The only addition made to the set-up (**3-4**) was the insertion of a second beam splitter between the incoming light and the first beam splitter (BS), in this way it was possible to control laser energy.
The different z-scan traces are shown in Fig**4-6**. As the energy increases, so does $\Delta T_{p-v}$. The nonlinear refractive index obtained from the measurements is presented in Fig **4-7**, where it can be see that for the lowest energy, with widest pulse width (3 A), the nonlinear refractive index is the highest and this goes down as the energy percentage decreases keeping the same pulse width, the same behavior is found in the case where the energy is increased but the pulse width is decreased. In this way it is possible to affirm that both energy and pulse width are important variables involved in the total nonlinear refractive index.
The nonlinear optical response of carbon disulfide can be attributed to two main mechanisms: electronic response and nuclear response, the first one is characterized by an almost instantaneous response of the bound electrons and has no dependency on pulse width. The nuclear response depends on the time duration of the excited beam and is characterized by three different mechanism: diffusive reorientation, libration mechanism and intermolecular collision-induced variations in the molecular polarizability [37]. Due to this nonlinear response dependence with pulse duration, it is expected that a wider pulse widens the nonlinear refractive index increase in its value because more structures are aligned with the electric field Fig **4-7**.

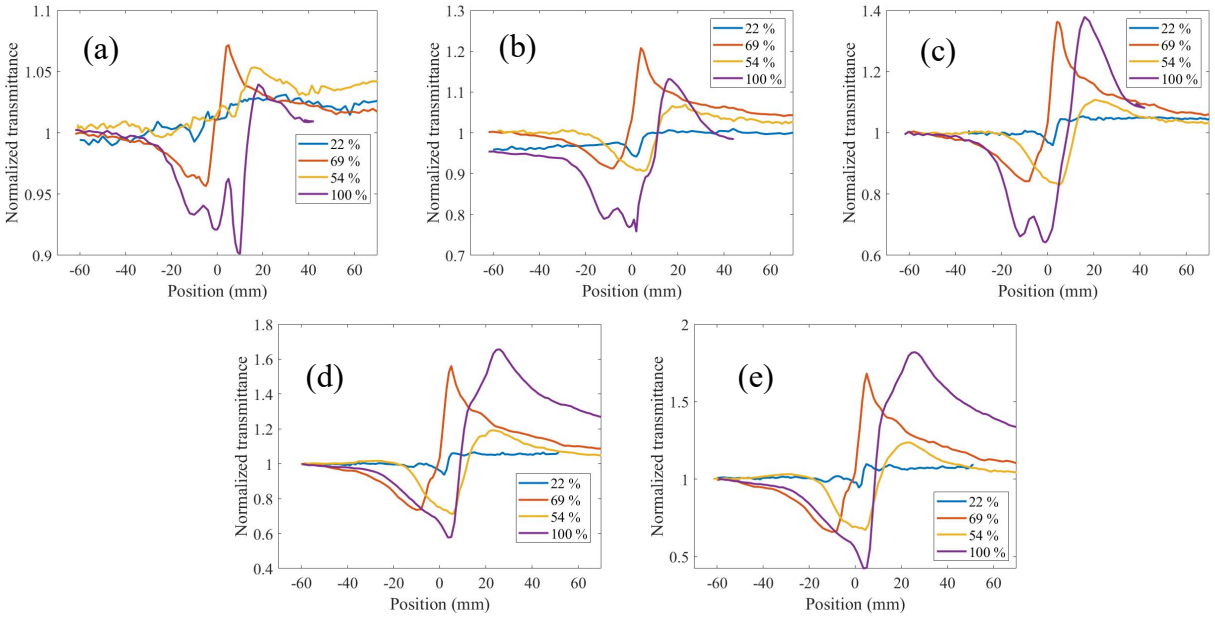


**Figure 4-6**.: $CS_2$ z-scan traces for different pulse widths and energies. (a)3 A, 248 fs pulse width. (b)4 A, 170 fs pulse width. (c)5 A, 107 fs pulse width. (d)6 A, 76 fs pulse width. (e)7.23 A, 51 fs pulse width

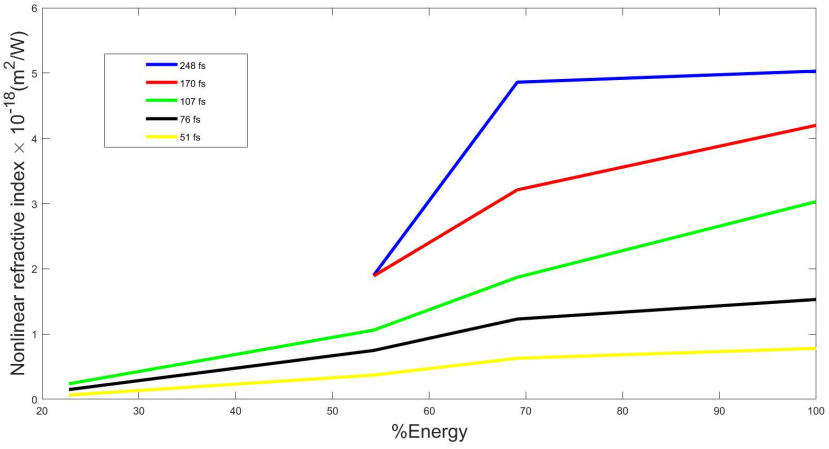


**Figure 4-7**.: $CS_2$ nonlinear refractive index in function of energy for different pulse widths.

Now, the remaining question is why at the same pulse width but lower energy there is a decrease in the nonlinear refractive index. it is well known that the nonlinear optical coefficient is independent from the intensity (Eq 3-45). This behavior is a good indicative of the presence of other nonlinear phenomena, thermal effect or the Stark effect. Due to the 50 MHz repetition rate of the laser used, it is necessary to take into account the thermal effect. Besides this, for the pump wavelength (800 nm) used there is probability of two-photon absorption. At low intensities and with the lower energy percentages, nonlinear refraction was not observed, it was until 5 A (**4-6**(c)) that a symmetric z-scan trace can be seen, which means that only the nonlinear refractive index phenomenon is presented, after that at 6 A and 7.23 A the trace corresponding to 22.79 % of energy exhibits a small peak just before the valley, indicating the presence of two photon absorption. On the other hand, comparing Fig **4-7** (b) to (e) the red trace with green one, there is other evidence of the presence of two photon absorption, in (b) red is almost symmetric, but this symmetry is break in (c) where the valley is enhanced, for (d) and (e) the valley continuous being increased, meanwhile the valley of the green trace follows the same behavior of the red, but its peak is much taller, this can be explained because the energy is high enough to excite other nonlinear phenomena that contribute to this comportment. For the highest energies (6 A and 7.23 A) the blue trace at its peak starts to distorts which means that nonlinear absorption and refraction starts to saturate due to the addition of free carriers.
The above observations indicate that the nature of nonlinear absorption and refraction is determined not only by third order nonlinear processes but also by higher-order ones as well as the effect of free charge carriers. The change in the refractive index due to higher order terms can be expressed as:

$$n = n_0 + n_{eff} I = n_0 + (n_2 + \eta I) I \tag{4-1}$$

where $n_{eff}$ is the effective value of the nonlinear refractive index and $\eta$ determines the fifth-order nonlinearity. In the case of generation of free carriers, the change in the refractive index can be expressed as:

$$\Delta n = n_2 I + \sigma_r N \tag{4-2}$$

the second term on the right hand side determines the contribution to the refractive index due to free carriers. $\sigma_r$ characterizes the change in refractive index due to a single charge carrier as a result of photoexcitation and formation of a cloud of free carriers with density $N(I)$. Although, $\sigma_r$ is negative for most media, in this case its contribution is positive because of the $n_2$ increase with intensity an alternative explanation is that its negative contribution would be compensated and surpassed by other nonlinear phenomena [36].
Nonlinear refraction can be influenced by thermal lensing effects, which can be caused by two processes: Propagation of an acoustic wave or a change in the medium density caused by the accumulation of thermal energy in the absorbing region as occurs in the case of low thermal conductivity of the medium and/or a high repetition rate of the laser pulses.

The time necessary for the occurrence of the first case, $\tau$, can be determined as the ratio of the beam waist radius to the speed of sound in the medium: $\tau = \omega_0/V_s$, that in the experimental conditions considered here: $\omega_0 = 0.3$ mm and $V_s \sim 1500$ m/s, the resultant response time of the process is: $\tau \sim 200$ ns, although the pulse widths used were lower than 300 fs, the repetition rate of 50 MHz means that the time interval between pulses is $\Delta t = 20$ ns, which is in the same scale of time as the acoustic wave. It has been found that the necessary time to form the acoustic wave can be two to three times shorter than this [36], although the ratio is close to ten times lower, this effect can not be neglected because in previous works thermal lensing acts to change the sign in the nonlinear refractive index coefficient, but in this occasion its effect increases its value, which means that the change in the molecular density acts in such a way that allows this behavior. However, further studies about the acoustic wave at this specific features must be perform to bring a clear answer, but it could not be performed due to the laboratory limitations.
The second process is the heat accumulation due to the nonlinear absorption and low thermal conductivity of the medium. The time necessary for the heat dissipation is determined by the relation [36]: $\tau = \omega_0^2 \rho c_p / 4\kappa$. Where $c_p$ is the specific heat capacity, $\rho$ is the density and $\kappa$ is the thermal conductivity of the medium. Giving $\tau \sim 589$ ms and hence it is necessary to take into account the heat accumulation. One confirmation in the role of the nonlinear absorption in the $n_2$ value is the dependence of $\Delta T_{p-v}$ with intensity. Even though similar experiments and studies have been done at 10 Hz and 80 MHz, the novel behavior exhibited at these laser parameters opens the possibility to know new features about how the different nonlinear phenomena interplay giving as a result an increase in the nonlinear refractive index with the increase of intensity.

### 4.4.2. Multi-Walled Carbon Nanotubes

Materials with high nonlinearities have found numerous applications in areas related to nanoscience, nanotechnology, metrology, spectroscopy and communications since they exhibit greatly properties such as nonlinear absorption, optical limiting, and Kerr effect. Among these materials, multi-walled carbon nanotubes (MWCNTs) are found, due to its significant delocalized $\pi$-electrons cloud along the tube axis as it was shown previously. [38] [39] [40] [41] The carbon nanotubes (CNTs) have been a cornerstone in several scientific disciplines, from Physics to Chemistry, going through Medicine and Biology, since their discovery by Ijiima[42] in the 1990s. Carbon nanotubes can be manufacturing by three different processes such as: arc discharge method that is appropriated for producing single or multi-walled CNTs with excellent quality[43], laser ablation method in order to obtain single-walled carbon nanotubes[44] and Chemical vapor deposition technique that is based on the hydrocarbons decomposition at high temperatures, This method allows the control of CNTs diameters[45] and the number of CNTs concentric tubes during the manufacture process.[46][47] In materials science, technology and applied engineering, a large number of studies has been conducted on carbon nanotubes, due to their extraordinary mechanical, thermal, physical and optical properties.[48][49][50][51][52][53] Its exceptional properties have allowed it to be used for various applications such as: quantum communication, optical switches and optical limiting devices[47]. CNTs are made up of hexagonal ring structures of carbon where each carbon atom undergoes $sp^2$ hybridization and thus having one free pure $p_z$ electron which can undergoes deslocalization. It has been found that materials with this characteristics exhibit high nonlinear optical properties, [49][50][51] so according to this it can be expected that MWCNTs as well.

Previously measurements of nonlinear optical properties of CNTs have been carried out, where the major investigation was done about single walled carbon nanotubes,[54] [55] [56] [57] nonetheless Zhaoxia Jin et al[58] reported both nonlinear refractive index and nonlinear absorption coefficient in MWCNTs through Z-scan technique.
To measure the nonlinear properties of MWCNT, the Z-scan technique was used.
Nevertheless in presence of high nonlinear refractive index the nonlinear phase shift is higher ($\mid \Delta\Phi \mid > \pi$) and the trace becomes asymmetric with respect to the focus, even under these conditions GD method is still valid and is better than some others[59], i.e., Fresnel–Kirchhoff diffraction and the aberration-free approximation model[60] due to its accuracy when the coefficients are extracted ($n_2$ and $\beta$).
Other phenomena rather than nonlinear refractive index and absorption can be presented such as thermal optical nonlinearities which take into account absorption process involving an arbitrary number of photons as the source of nonlinearity[61]. In addition, closed aperture is sensitive to this kind of effect,i.e, thermal lens which comes into play if the long time behavior is investigated. The presence of such effect occurs when the train of pulse spacing that inside

in the sample are shorter than the thermal characteristic time $t_c = \omega^2/4D$ where $D(cm^2s^{-1})$ is the thermal diffusion coefficient of the material, for typical samples the condition is met when the laser repetition rates is greater than kHz, this gives as result large Z-scan signals. In this work, is reported the influence of MWCNTs concentration, pulse width, and energy on MWCNTs nonlinear optical parameters, as well as the possible appearance of other nonlinear effects that make bigger the Z-scan trace.

### MWCNTs preparation

In this study, MWCNTs with outer diameters of $10-40$ nm and inner diameters of $10-20$ nm and a length of $30-50nm$ were used (Fig**4-8**). Although inner diameters of the MWCNTs have no direct influence on the dispersion of the CNTs in a solution, outer diameters of the MWCNTs used in this work are small, which could increase the risk of re-agglomeration. Due to this, a polyvinyl alcohol (PVA) solution was used for dispersing, and the dispersing effect of the polymer (PVA) was maintained for a long time, whereby the CNTs re-agglomeration was avoided, and this effect was reported by Olayo et al[62]. The dispersion of the MWCNTs in the PVA was quantified in a previous work[48] and well behavior was found (for details see Ref. [48]). For the samples preparation, pellets of fully hydrolyzed PVA were diluted in hot distilled water to produce a solution of $1wt.$ % of PVA. MWCNTs were introduced into the PVA solution in percentages of 0.212, 0.235, 0.675 and $0.75wt.$ %, where the MWCNTs were dispersed by magnetic stirring during 30 min at an average speed of $600-900$ rpm followed by a sonication during one hour in a Vibra Cell series CLC equipment, which was set to a power of 100 W and an amplitude of the probe of 20 %; the dispersion parameters were selected in order to prevent damage of the CNTs.[63][64]

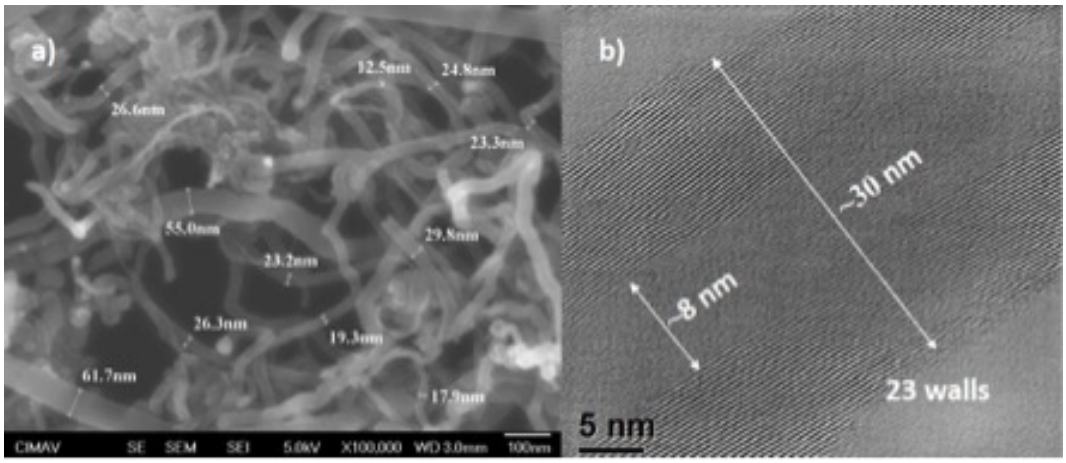


**Figure 4-8**.: a) Scanning electron microscope (SEM) image of MWCNTs and b) Transmission electron microscope (TEM) image detail of a multi-walled carbon nanotube

### Z-scan measurement

Different Gaussian pulse width were considered: 248 fs, 170 fs, 107 fs, and 76 fs, with a repetition rate of 50 MHz at 780 nm wavelength, the samples were deposited in a quartz cell of $1mm$-thickness which was moved along the Z-axis. After light passed through the sample, it encounters an aperture that allows to make the measurements in open and closed aperture ($S = 0.5$). From closed aperture measurements, according to eq.3-61, we can obtain the nonlinear refractive index. The dependence between nonlinear refractive index and MWCNTs concentration was investigated, in this case, the same pulse width and energy were used. In Fig.**4-9** is shown how the nonlinear refractive index value increases with MWCNTs concentration, nonetheless at higher input energies and shorter pulse widths the nonlinear values decrease. The growth in MWCNTs' $n_2$ because of concentration can be attributed to the number of structures that can be aligned with the electric field, that is, the number of dipole moments.

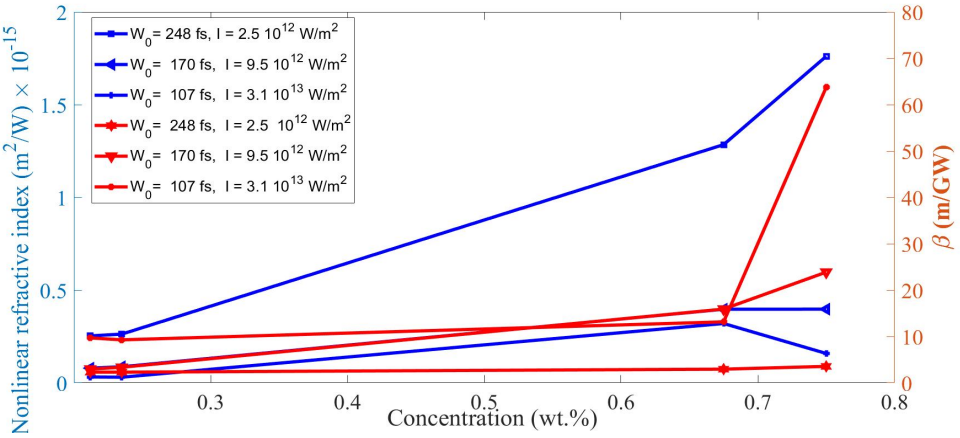


**Figure 4-9**.: Nonlinear refractive index and $\beta$ values for different MWCNTs concentrations at different pulse widths and energies

On the other hand, $n_2$ decreases with shorter pulse widths and higher energy. In Fig**4-10** is shown how these effects affect the nonlinear refractive index when the concentration is fixed, for longer pulse widths we have a slow increase in $n_2$ from the lowest concentrations while higher ones show faster changes in their values. Fig**4-10**(b) shows how at high intensities the nonlinear refractive index decreases which is slower for lower concentrations and more pronounced for the highest ones. This can be explained according to: an enhancement in $n_2$ with long pulses indicate the presence of non-instantaneous nonlinearity (nuclear response), this can be checked in Fig.**4-11** where the nonlinear dependence of $\Delta T_{p-v}$ vs intensity is

shown [22]; in case of pure electronic contribution this dependence scales linearly, the reason of this behavior change with respect to the concentration can be attributed to the number of dipole moments that contribute to the hyperpolarizability. At short pulses it can be seen that $n_2$ undergoes a relatively low change, at this point the nuclear contribution starts to disappear and the electronic response is the only one present. The second reason is that the difference in transmittance between peak and valley begins to reduce at certain intensity level, with higher intensities come into play other nonlinear phenomena such higher absorption orders and thermal effects, where the nonlinear refractive index is directly proportional to $\Delta T_{p-v}$.

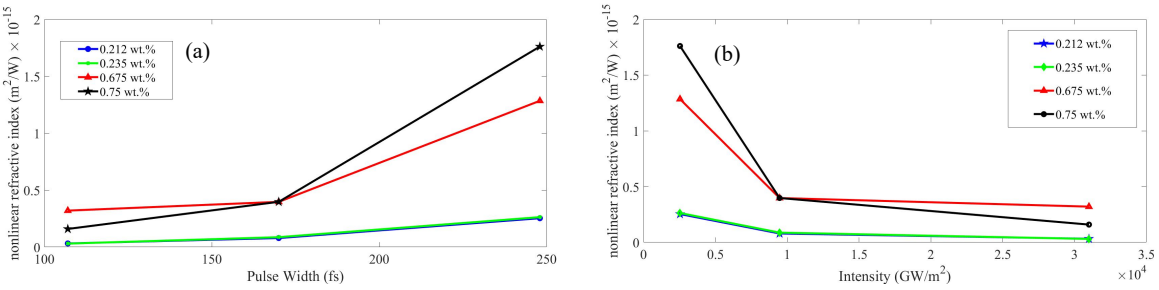


**Figure 4-10**.: Nonlinear refractive index behavior as function of (a) pulse width and (b) intensity, with fixed concentration.

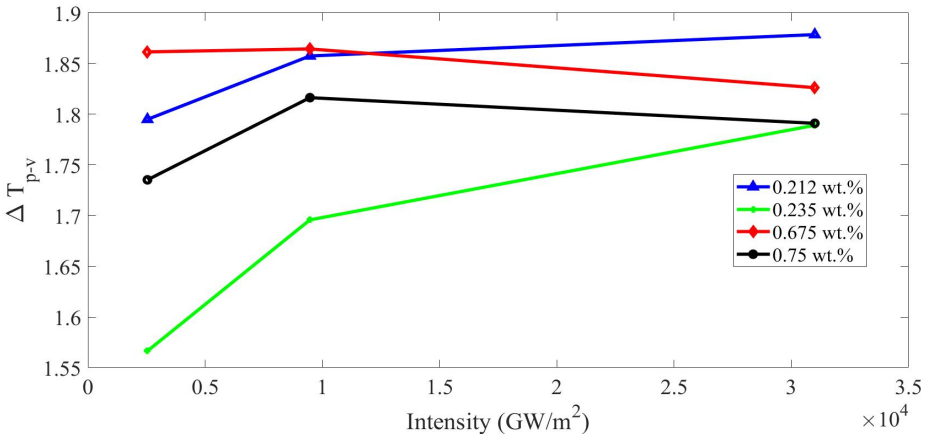


**Figure 4-11**.: Variation of $\Delta T_{p-v}$ vs intensity at different concentrations where it can be seen the non instantaneous behavior and the presence of other nonlinear phenomena.

### Nonlinear absorption

Other important parameter that can be measured from Z-scan trace in open aperture ($S = 1$) is the nonlinear absorption coefficient ($\beta$). First, it was investigated the influence by the incident intensity when the concentration is kept constant, Fig.**4-12**(a), as can be observed for lower concentrations (0.212 and 0.235 wt.%) the behavior is almost constant until $1 \times 10^{13}(W/m^2)$. This is the limit for the two photon absorption (TPA) process, however at higher peak powers $\beta$ starts increasing what indicates the presence of higher nonlinear process. These terms are present from the beginning of the highest concentration (0.75 wt.%), in the same way 0.675 wt.% does it, but with a more smooth slope. In Fig.**4-12**(b) the $\beta$ relationship with pulse width is displayed. Although, for our experimental conditions, broader pulse widths imply lower intensities which make it impossible to study the pulse width influence separately but it is interesting to observe that when the pulse width is wider and the intensity lower, $\beta$ reaches its minimum value for each concentration. This could mean that other phenomena like thermal effects and higher absorption terms are more affected by intensity than by the pulse width, this relation must be investigated more carefully taking into account the laser repetition rate, but it is beyond the scope of this work.
Defining $\eta = \beta/2kn_2$ as the ratio between the imaginary and the real part of the complex nonlinear phase shift [60] one can investigate the nonlinear absorption contribution from the closed aperture Z-scan transmittance. This parameter is presented in Fig.**4-13**, it is worthy to note that for every concentration this contribution increases, except for 0.675 wt.%. The reason for this behavior is not clear yet.

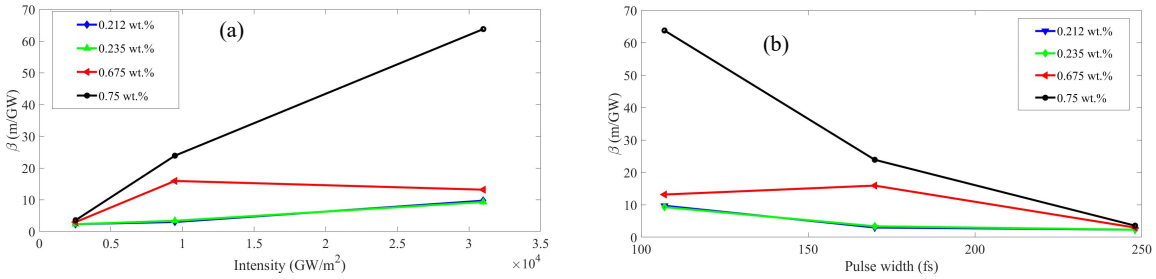


**Figure 4-12**.: Variation of $\beta$ with (a) Intensity and (b) pulse width for different concentrations.

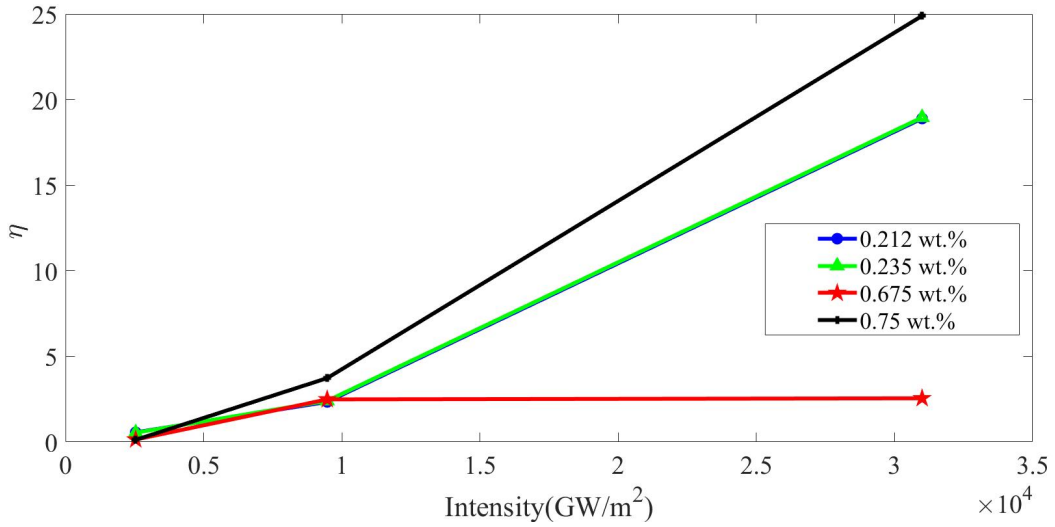


**Figure 4-13**.: Ratio of the imaginary to the real part of the complex nonlinear phase shift as intensity function

### Higher nonlinear effects and thermal contribution

In Fig. 4-14 is shown different Z-scan traces varying the concentration and keeping the energy constant (a and b), and variation in energy at fixed concentrations (c and d), from the figures one can observe a large nonlinear phase shift and the usual level increment before the valley followed by a post focal peak[60]. According to Fig. 4-14a the variation of concentration at low energy does not affect significantly the Z-scan trace and it can be seen like a normal Z-scan transmittance where there is symmetry around $z = 0$. But we have a different picture when the energy is increased, as it is seen in Fig. 4-14b. In this case, the $\Delta T_{p-v}$ is almost the same than 4-14a, but its peak and prefocal valley starts to look asymmetric, which is a good indicator of higher nonlinear terms and contributions.
Figs. 4-14c and 4-14d show that the main parameter responsible for large nonlinear shifts and the asymmetric shape is the pulse energy, as different concentrations all exhibit a symmetric behavior with the lowest energy values.
A good way to see if thermal effects are present, is to relate the normalized peak valley distance[61], these effects can be generated for multi-photon absorption, as a higher number of photons are involved the normalized peak valley distance is lower. In Fig. 4-14 is noted that there is not presence of nonlinear higher effects, only TPA.
Due to repetition rate used (50 MHz) and different pulse widths considered, it is possible to have a thermal effect where it can be proved by the use of different substances instead of

water that posses distinct diffusive thermal coefficient, nonetheless this study can be taken into account in the future. To summarize, the most important measurements are displayed in table4-2.

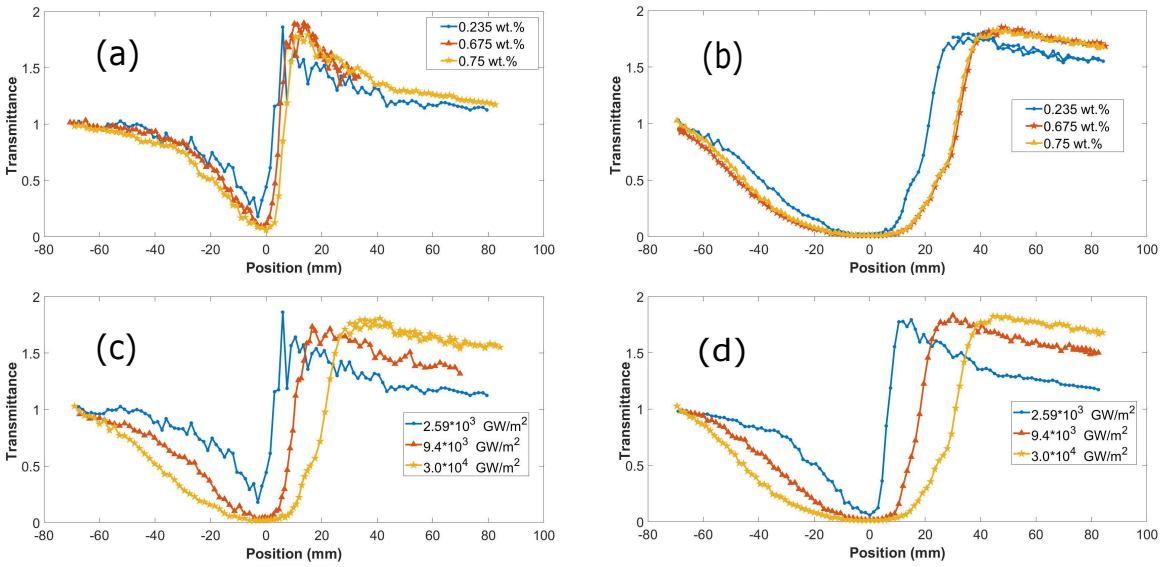


**Figure 4-14**.: Z-scan traces at different MWCNTs concentrations and Intensities. (a) Intensity $2.5 \times 10^{12}\ W/m^2$, (b) Intensity $3 \times 10^{13}\ W/m^2$, (c) concentration 0.235 wt.%, (d) concentration 0.75 wt.%

**Table 4-2**.: Nonlinear parameter measurements for different intensities and concentrations $wt.\%$

| $wt.\%$ | I= $2.54 \times 10^{12}\ W/m^2$ | I= $9.47 \times 10^{12}\ W/m^2$ | I= $3.09 \times 10^{13}\ W/m^2$ |
|---|---|---|---|
| | $n_2(m^2/W)$ , $\beta(m/GW)$ | $n_2(m^2/W)$ , $\beta(m/GW)$ | $n_2(m^2/W)$ , $\beta(m/GW)$ |
| 0.212 | $2.53434 \times 10^{-16}$,2.3071 | $7.9175 \times 10^{-17}$, 2.9867 | $3.1862 \times 10^{-17}$,9.6983 |
| 0.235 | $2.6281 \times 10^{-16}$, 2.3071 | $8.6836 \times 10^{-17}$,3.3617 | $3.0380 \times 10^{-17}$,9.2779 |
| 0.675 | $1.2845 \times 10^{-15}$,2.9551 | $3.9708 \times 10^{-16}$,15.917 | $3.2006 \times 10^{-16}$,13.160 |
| 0.75 | $1.7607 \times 10^{-15}$,3.5529 | $3.9742 \times 10^{-16}$,23.880 | $1.5943 \times 10^{-16}$,63.762 |

### 4.4.3. Non-linear refractive index in Hydrocarbons

We present the theoretical background and the experimental characterization of the non-linear refractive index in a set of hydrocarbon dyes. The analytical approach is based on the free electron model and the measurements of the non-linear refractive index were performed by using the z-scan technique[22]. As it is discussed below, the third order non-linear susceptibility depends directly on the double conjugated $\pi$ bonds and the molecular concentration of the organic compounds, this dependence was empirically evidenced by a linear relationship between the experimental non-linear refractive index and the linear refractive index.

#### Non-Linear Refractive index and Polarizability

In organic materials the polarization vector $\vec{P}$, related to first and higher order of susceptibility, is governed by their corresponding molecular polarizability. For the third order polarizability, this relation can be written as $P_i^{(3)} = \epsilon_0 \chi^{(3)} E^3 = N p_i^{(3)} = \epsilon_0 N \gamma^{(3)} E^3$, where $\gamma^{(3)}$ is the third-order polarizability, $\chi^{(3)}$ the third-order susceptibility, $\epsilon_0$ the vacuum permittivity and $N$ the number of molecules per unit volume. Considering the Free electron model (FE) for describing the organic molecule, where $\sigma$-bounds acts as a potential well and $\pi$-conjugated bounds as free-electrons, the length $L$ of the potential well is given by $L = d(j + \sigma)$, where $d$ is the distance between conjugated atoms, $j$ the quantity of conjugated bonds and $\sigma$ is a correction parameter[65]. In the same model, the transition dipole moment between $m$ and $n$ states at their corresponding transition frequencies is given by [65]:

$$\mu_{mn} = \frac{4eL}{\pi^2 \left[\frac{1}{(m-n)^2} - \frac{1}{(m+n)^2}\right]^{-1}} \tag{4-3}$$

where $e$ is the electron charge. Once the parameters of the molecule structure are known, the nonlinear susceptibility can be estimated according to [66]:

$$\chi^{(3)}_{kjih}(\omega_\sigma, \omega_r, \omega_q, \omega_p) = \frac{N}{\epsilon_0 \hbar^3} \mathbf{P}_f \left[ \sum_{lmn} \frac{\mu_{gn}\mu_{nm}\mu_{ml}\mu_{lg}}{(\omega_{ng} - \omega_\sigma)(\omega_{mg} - \omega_q - \omega_p)(\omega_{lg} - \omega_p)} - \sum_{ln} \frac{\mu_{gn}\mu_{ng}\mu_{gl}\mu_{lh}}{(\omega_{ng} - \omega_\sigma)(\omega_q + \omega_p)(\omega_{lg} - \omega_p)} \right] \tag{4-4}$$

where $\mathbf{P}_f$ denotes the full permutation operator and $\omega_{mn} = (m^2 - n^2)(\hbar\pi^2/8m_0L^2)$ is the transition frequency with $m_0$ the electron mass. Finally, the nonlinear refractive index due to the Kerr-effect can be expressed as $n_2 = (3/4n_0)\,\chi^{(3)}(-\omega, \omega, -\omega, \omega)$, $n_0$ being the linear

refractive index. It is worth noting that this latter expression relates the non-linear and linear refractive indexes through an inverse relationship for a determined molecular concentration. However, as it is stated in Eq. (4-4), the non-linear susceptibility depends proportionally on the molecular density as well as the electronic transitions between energy states so it involves a more complex relationship based on molecular structure.
The Z-scan technique was implemented to measure $n_2$. To accomplish the experimental set-up a lens of 17.5 mm focal distance was utilized, the sample was poured inside a 1 mm cuvette, located on a motorized station controlled by computer for its displacement along the sample-path. Non-linear Kerr phenomenon was excited by using a laser with a total power of 237 kW, a pulse-width of 50 fs, and a wavelength of $\lambda_0 = 780$ nm. The maximum intensity obtained at the waist was of $I = 10.3\ TW/m^2$. Hydrocarbon samples were obtained from *Cargille laboratories, inc., serie AA*. A total number of fifteen hydrocarbon samples were used for measuring $n_2$ and determine its relation to the linear refractive index. Fig.**4-15**(a) plots some of the experimental results of the Z-scan technique and the numerical fitting curves used for the computations.

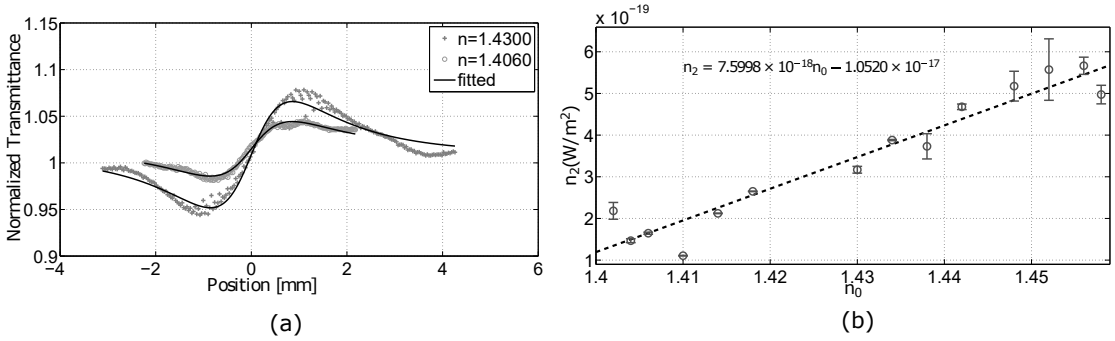


**Figure 4-15**.: Experimental results for non-linear refractive index measurements. (a) Normalized transmittance for Z-Scan on organic dyes (b) Relation between estimated non-linear refractive index and linear refractive index of the tested organic dyes

Once the nonlinear refractive indexes were obtained for each sample, they were related to its linear refractive index resulting in a linear dependence as shown in Fig. **4-15**(b). This behavior is directly connected with the molecular hydrocarbons structure and the per-volume concentration in the sample as described in Eq. (4-4). This must be not confused with the local inverse relationship between $n_2$ and $n_0$ for a particular concentration. The experimental results show explicitly that even if the samples contain the same components, the proportion of each ones could lead to important variations on both linear and nonlinear refractive indexes. Based on these preliminary results, the molecular density could be estimated once $n_2$ and $n_0$ are known, by means of Eq. (4-4) under the assumption of a pure sample.

### 4.4.4. Conclusion

In this chapter we discussed how the Z-scan technique was implemented, and how a code was developed to perform the control, acquisition data and analysis of the Z-scan process. This code was developed from scratch in our laboratory to fulfill measurement requirements and the user has different options to control the process: step size, number of points, normalization variables, power displayed from each power meter, fitting, among others. Many obstacles were overcome, mainly in the initial data gathering for parameters such as beam waist, power at the focal point and Rayleigh distance. The method used to obtain the nonlinear refractive index and nonlinear absorption coefficient was shown to be inside the error margin found in the literature, this was corroborated by making measurements of known substances and comparing them with literature reported values. The implemented technique allowed us to perform different substances measurement, among them: Cs2 was studied and its dependence with energy and pulse width, where it was found that the nature of nonlinear absorption and refractive index is not only determined by third order process but also by higher order processes and thermal effects as well as the repetition rate used. Multi-walled carbon nanotubes were investigated, where they were prepared for different concentrations. A study of the nonlinear parameter dependence with concentration, pulse width and energy were performed. It was found that at higher concentration the nonlinear refractive index increases with the pulse width and the nonlinear absorption coefficient increases with the intensity, it was concluded that this contribution is due to electronic and nuclear responses. Besides, due to the traces a new phenomenon is proposed: the influence of thermal effects, nevertheless a complete analysis is necessary. Finally, some hydrocarbons' nonlinear parameters were measured and reported these substances are of interest as they are widely used in fiber optics applications.

# 5. Nonlinear Pulse Propagation Simulation

## 5.1. Liquid-Core Photonic Crystal Fiber for Supercontinuum Generation Based on Hybrid Soliton Dynamics

The generation of new optical frequencies has attracted attention ever since the laser's invention in the 1960s. Supercontinuum generation covers a broadband spectrum [1] and has been widely studied due to its importance in applications such as spectroscopy, where typically tunable pulsed laser sources are used for material characterization, and telecommunications, where the multiple wavelengths can be beneficial for multiplexing purposes. Current research focuses in the enhancement of SCG by means of increasing nonlinear parameters of the generation medium. Thus, the use of PCF as medium is a good choice due to its high refractive index contrast and small core diameter which allows to obtain higher nonlinear parameters in comparison with standard fibers. Although it is possible to excite nonlinear effects and obtain higher responses with less input power, silica waveguides pose their own limits. On the other hand, using a hollow-core PCF infiltrated with a different material of higher nonlinear properties like carbon disulfide ($CS_2$) can improve the nonlinear effects for SCG, referring to this kind of fiber as liquid-core photonic crystal fiber (LCPCF). The solvent $CS_2$ has a nonlinear refractive index two orders of magnitude higher than silica [68] and it is known that the nonlinear susceptibility coefficients in liquids are 10 to $10^3$ times higher than in solids [67]. The main mechanisms involved in SCG using $CS_2$-LCPCF are: self-phase modulation (which is responsible for phase distortion), soliton fission, dispersive wave generation, four wave mixing, Raman scattering [69] and self-steepening, which is responsible for the distortion in envelope shape. In the case of SCG based on soliton propagation, the anomalous dispersion regime for the geometry used in this work has been found to be of around 1.95 $\mu$m. It was also found that soliton fission is one of the main mechanisms that generate a broadband super continuum. A soliton can be seen as a phase compensation between the group velocity dispertion (GVD) and the phase accumulation due to the Kerr

effect. The soliton number is given by: $N = \sqrt{\gamma_0 P_0 \tau_0^2 \mid {\beta_2}^{-1} \mid}$; where $\gamma_0$ is the nonlinear coefficient, $P_0$ is the input peak power, $T_0$ is the input pulse width and $\beta_2$ is the second derivative of the propagation constant. As a result of the perturbation a soliton experiences as it propagates in a kerr medium due to third order dispertion or Raman scattering, the higher order soliton (N>1) breaks into a series of fundamentals solitons (N=1), each at different optical frequency and followed by a dispersive wave in the normal propagation side.

In case of liquid media, within the Born-Oppenheimer approximation, the nonlinear responses consist of a combination of two responses: an instantaneous response or bound-electron contribution and a non-instantaneous response due to nuclear effects; this nuclei response can also be understood as three independent responses: diffusive reorientation, librational response and collision-induced contribution [70], where each contribution has its own response time [37]. In this work, we present a detailed study, through the simulation of generalized nonlinear Schrödinger equation, of the nonlinear pulse propagation in a commercial hollow-core photonic crystal fiber (PCF), whose core was infiltrated with carbon disulfide ($CS_2$), as shown schematically in the inset of Fig **5-1**. This fiber was reported previously using a similar geometry presented in [69]. However, the response function for the $CS_2$ measured recently by Reichert *et al.* [70], which gives rise to a new so-called hybrid soliton behavior due to a slow response of the material [37],[71], was not included. Here, it is not only take into account this new response function but also study the dependence on several input parameters such as pulse width, energy, and length of the liquid-core PCF (LCPCF). For this particular case ($CS_2$-LCPCF), the zero dispersion wavelength was found around 1.86 $\mu$m Fig**5-1**. Thus, the pump wavelength is chosen to be around 1.95 $\mu$m in order to ensure anomalous dispersion regime propagation.

### Linear parameters

We used the finite elements method to obtain the zero dispersion wavelength according with the geometry and the effective mode area, where it was calculated according to [2] using the Sellmeir equation:

$$n_{CS_2}(\lambda) = 1.580826 + 1.52389 \cdot 10^{-2}/\lambda^2 + 4.8578 \cdot 10^{-4}/\lambda^4 - 8.2863 \cdot 10^{-5}/\lambda^6 + 1.4619 \cdot 10^{-5}/\lambda^8 \quad (5\text{-}1)$$

The effective area was calculated according with the relation

$$A_{eff} = \frac{(\iint_{-\infty}^{\infty} |F(x,y)|^2 \, dxdy)^2}{\iint_{-\infty}^{\infty} |F(x,y)|^4 \, dxdy} \quad (5\text{-}2)$$

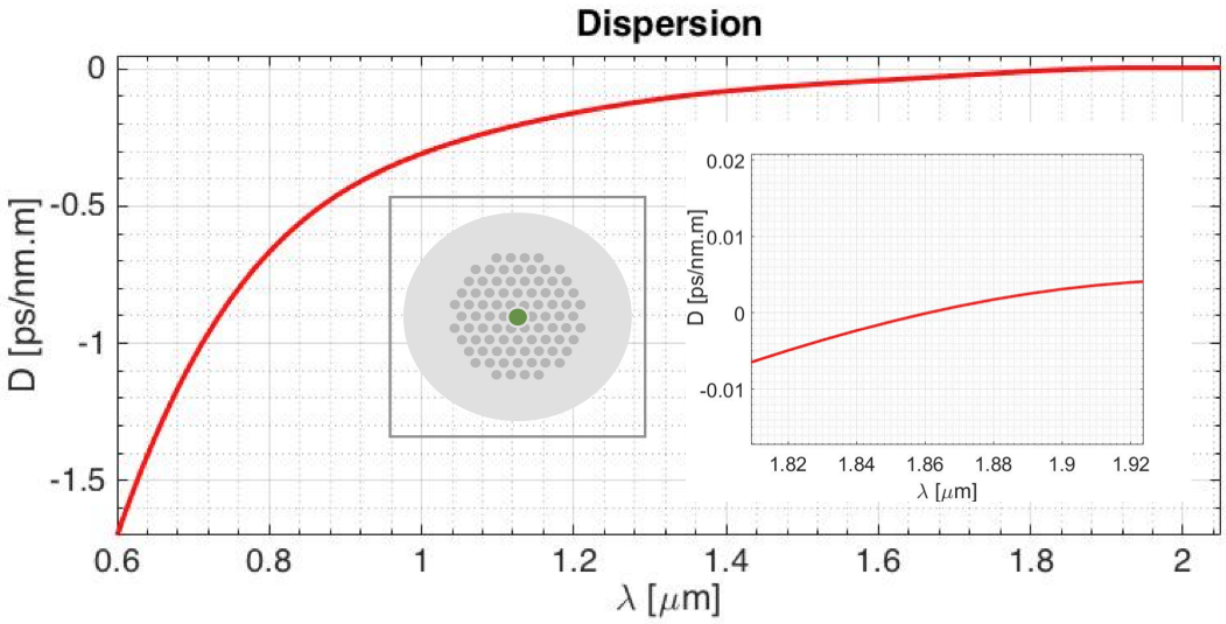


**Figure 5-1**.: Dispersion as wavelength function. Photonic crystal fiber with $CS_2$ in its center

### Nonlinear parameters

To obtain the nonlinear coefficient ($\gamma_0$) the instantaneous and non-instantaneous responses of the change in the refractive index were considered, where the electronic component was set to $1.6 \times 10^{-19}$ [37] and the molecular response varied according to the pulse width at half maximum ($T_{FWHM}$) [37]. The total nonlinear refractive index is defined as $n_{2,cs_2} = n_{2,el} + n_{2,mol}$, where $n_{2,el}$ is the nonlinear refractive index due to the electronic response of the solvent and $n_{2,mol}$ is the nonlinear refractive index due to the molecular contribution. Thus, $\gamma_0$ will be function of pulse width according the relation

$$\gamma(\omega_0, T_0) = \frac{\omega_0 n_2(T_0)}{cA_{eff}} \tag{5-3}$$

### Generalized nonlinear Schrödinger equation

The pulse evolution through the $CS_2$-LCPCF was simulated by the nonlinear schrödinger equation 3-21 [2]. where the second term of the left hand side of the equation (3-21) stands for the losses in the material (not simulated here), the third term involves the medium dispersion. The right hand side of the same equation shows the nonlinear terms inside the material as a result of the high intensity pulse propagation. The nonlinear response

function $R(t)$ includes both the electronic and nuclear contributions. Assuming that the electronic contribution is nearly instantaneous, the functional form of $R(t)$ can be written as $R(t) = (1 - f_m)\delta(t) + f_m h_R(t)$. Here, the molar fraction $f_m$ is calculated as $f_m = n_{2,mol}/(n_{2,el} + n_{2,mol})$. Equation (3-21) was solved by the split step method [2] where we considered up to 10 dispersive orders (see table **5-1**). The $T_{FWHM}$ considered were 0.1 ps, 0.2 ps, 0.3 ps, 0.4 ps, 0.5 ps to each pulse width corresponds to a different molar fraction.

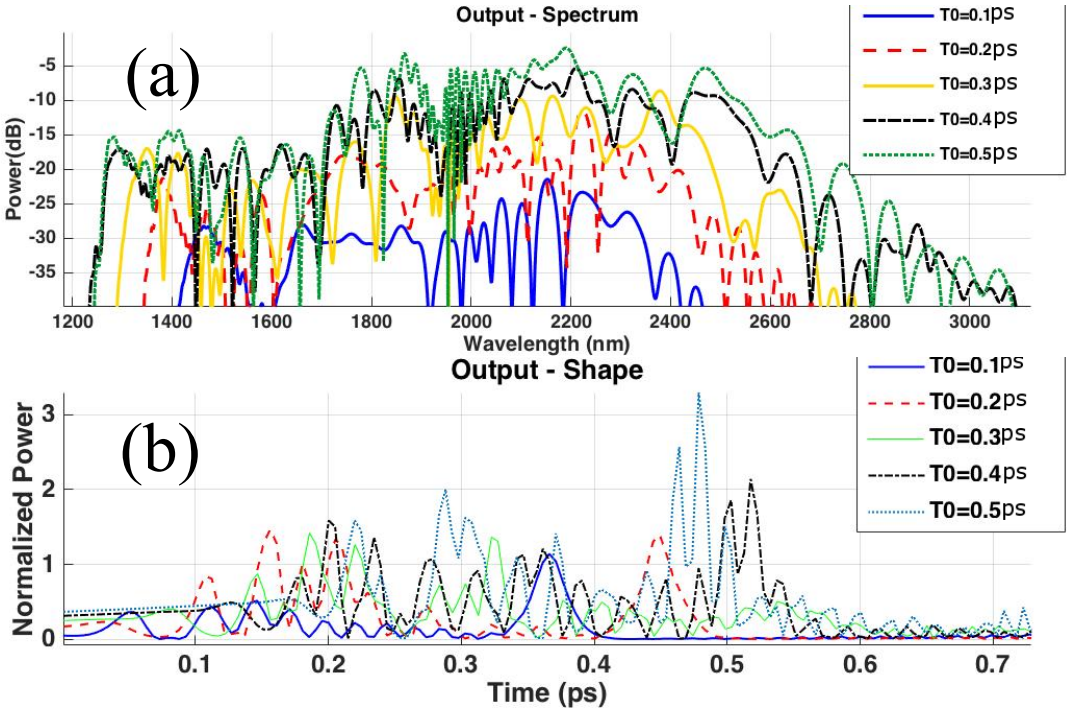


**Figure 5-2**.: simulation at different temporal pulse widths. (a)output spectrum considering $T_0$ between 0.1 ps and 0.5 ps. (b) output shape for the same range of temporal pulse width.

## 5.1.1. Results

### Supercontinuum as pulse width function

The molecular non-linear refractive index has a pulse width dependence, which implies that the nonlinear parameter ($\gamma_0$) have this dependence, according to this it was performed different simulations for distinct pulse widths to examine the bandwidth behavior. Fig.5-2 shows the temporal and spectral behavior, where it can be seen that for a longer pulse width, a wider bandwidth is obtained. Here with $T0 = 0.1$ ps the spectral broadening was close to 100 nm while with $T0 = 0.5$ ps was close to 1800 nm. At the same time, the output power was higher. This is in agreement with what was expected because in the presence of a prolonged pulse the nonlinear molecular refractive index has a higher contribution and this is reflected in the spectral broadening.

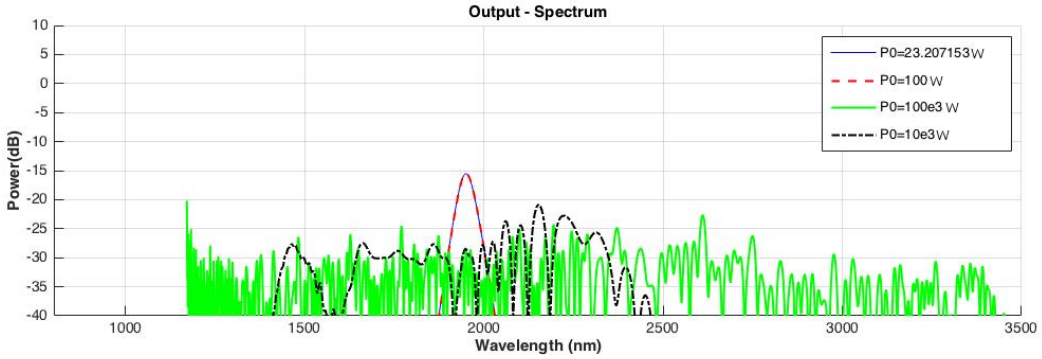


**Figure 5-3**.: spectrum at different input peak powers with pulse width 0.1 ps and propagation distance 0.1 m, the higher spectrum broadening correspond to the higher number of solitons.

### Supercontinuum as a funtion of peak power input

The next parameter to study in order to find the correct response function was the influence of the peak power on supercontinum generation. It is known that one of the main mechanisms through which supercontinuum is generated is soliton fission, the number of solitons is function of the peak power, it was simulated at $T0 = 0.1$ ps, for four different peak powers $P_0 = 23.20$ W, $P_0 = 100$ W, $P_0 = 10e3$ W, $P_0 = 100e3$ W which correspond to N=1, N=3, N=21, N= 66 respectively, all the simulations were set to the same propagation distance d=0.1 m. It can be see how the peak powers corresponding to N=1 and N=3 are almost the same and do not suffer a notable change on their spectra (Fig.**5-3**), the shape is similar to the initial pulse's. However, the pulses with peak power corresponding to N=21 and N=66 suffer spectrum broadening, where the main difference between them is the bandwidth and shape and not the output power, this can be understood as at higher powers ther will be more solitons present that will fission causing that each of them contribute to the creation of new frequencies, and the excess in energy will be distributed to the new frequencies. This result is in accordance with previous reports of soliton fission's influence on supercontinuum generation.

### supercontinuum as propagation distance function

The final parameter to consider in supercontinuum generation is how the propagation distance influences the bandwidth, a set of simulations were performed for different temporal pulse widths ($T_0$) and number of solitons as well as different peak powers. In Fig.**5-4**(a) the initial pulse width was 0.45 ps, with which it we obtained $f_m = 0.85$. With a peak power of $10^3$ W corresponding to N=170, it can be see how the spectral broadening starts early

on and at a distance of 0.1 m the bandwidth is close to 40 kHz; here, 0.1 m corresponds to $0.0053L_D$, $L_D = T_0^2 \mid {\beta_2}^{-1} \mid$. This fast spectral broadening can be obtained due to the high number of solitons. Afterwards, the simulation was done with N=1 soliton, with a temporal pulse width of 0.1 ps and a peak power of 23.207 W, Fig.5-4(b) shows how the pulse shape remains unchanged, even though the total propagation distance under consideration was about $161.29L_D$. Finally, another simulation studied the behavior with N=2 solitons at the same propagation distance than for the case N=1, the pulse shape suffers spectral broadening thanks to the propagation of both solitons which contribute to the creation of new frequencies, however the spectral broadening compared to N=170 is much lower. Even if it we change the peak power to generate a single soliton and keep the temporal pulse width at 0.45 ps, no spectral broadening is seen even at a distance of 5 m, which points out that the main mechanism to generate supercontinuum is soliton fission, in contrast to the molecular fraction involved in the process.

**Table 5-1**.: Dispersive terms used in the simulations

| **Dispersive parameter** | |
|---|---|
| $\beta_{(2)}(ps^2/m)$ | $-0.010381820088725$ |
| $\beta_{(3)}(ps^3/m)$ | $3.947834808010180 * 10^{-04}$ |
| $\beta_{(4)}(ps^4/m)$ | $-1.185333558903076 * 10^{-06}$ |
| $\beta_{(5)}(ps^5/m)$ | $4.818734892992571 * 10^{-09}$ |
| $\beta_{(6)}(ps^6/m)$ | $-1.663101220262766 * 10^{-11}$ |
| $\beta_{(7)}(ps^7/m)$ | $4.382086148498273 * 10^{-14}$ |
| $\beta_{(8)}(ps^8/m)$ | $-7.581647531149060 * 10^{-17}$ |
| $\beta_{(9)}(ps^9/m)$ | $6.391966459637023 * 10^{-20}$ |
| $\beta_{(10)}(ps^{10}/m)$ | $8.101162901563616 * 10^{-31}$ |

## 5.1.2. Conclusions

The temporal and spectral behavior for a hollow-core photonic crystal fiber infiltrated with carbon disulfide was presented, with a more complete model of response function, with which the behavior and dynamics were studied under different circumstances for supercontinuum generation. it was found that is important to take into account the carbon disulfide response functions because it can change the times and distances at which different phenomena occur. In this part of the thesis we also presented how the peak power influenced the spectral broadening, which is closely related to the number of solitons, identifying soliton fission as the main mechanism behind SCG when using this new response function. The propagation

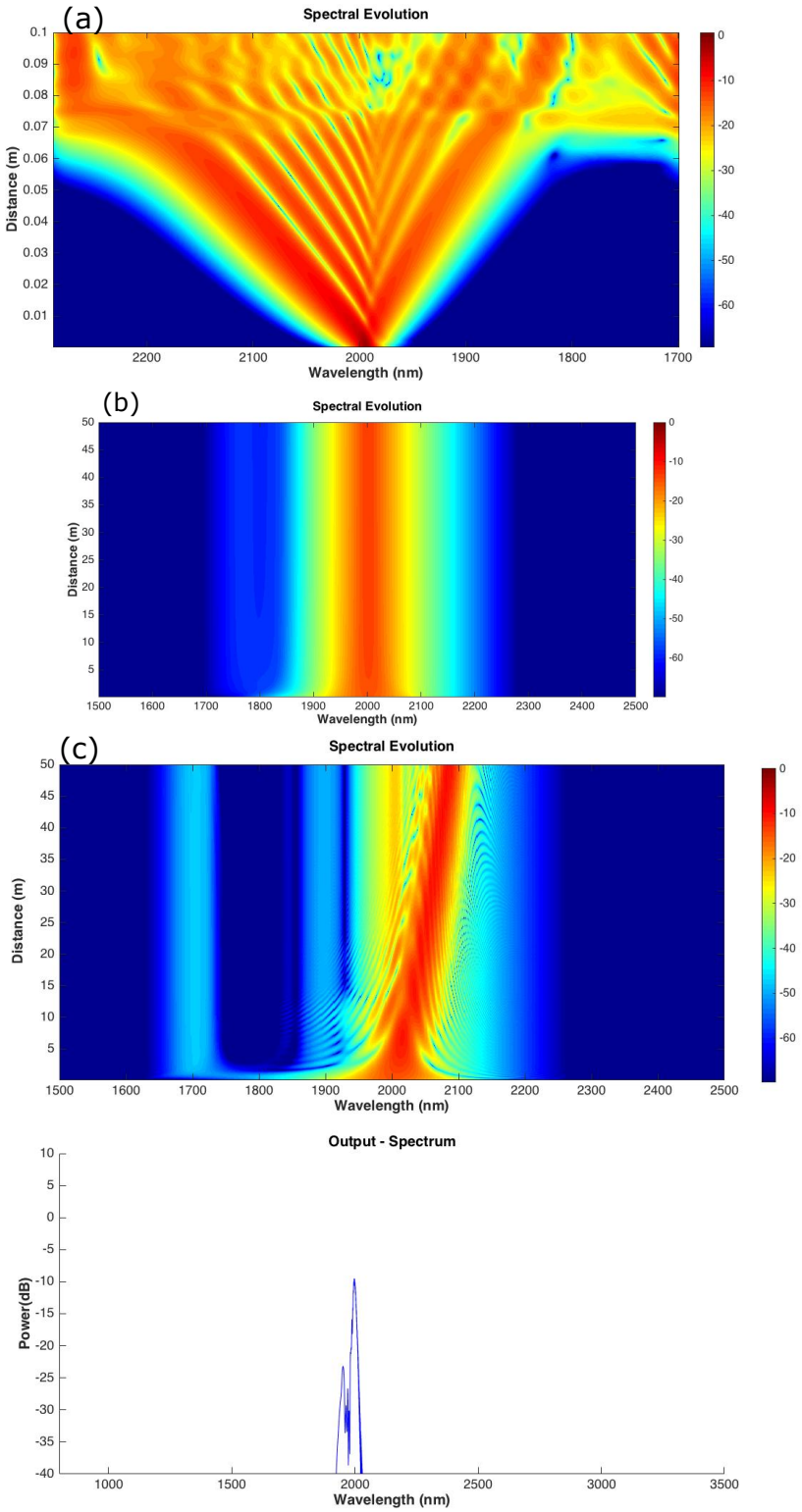


**Figure 5-4**.: Propagation distance dependence for different number of solitons. (a) 170 solitons, with a temporal pulse width of 0.45 ps, $f_m = 0.85$ and $0.0053L_D$. (b) 1 soliton with a temporal pulse width of 0.1 ps, $f_m = 0.5073$. (c) 2 solitons with temporal pulse width of 0.1 ps and $f_m = 0.5073$

distance is another variable under consideration, where it was established that in the distance under consideration with one soliton the spectral broadening was negligible but with two solitons the spectral broadening increased with the propagation distance. Concluding so the main mechanism behind SCG, taking into account the new response function, was soliton fission, where the non-instantaneous response acts by increasing the effective non-linear refractive index and the non-linear parameters.

## 5.2. Dispersive Wave and Four-Wave Mixing Generation in Non-instantaneous Nonlinear Fiber Solitons

This section presents a detailed analysis regarding the generation of a dispersive wave (DW) and four-wave mixing (FWM) in the non-instantaneous, nonlinear response of solvents using a commercial photonic crystal fiber (PCF) filled with carbon disulfide ($CS_2$) where the beam is pumped in the anomalous dispersion domain. The main finding is the fact that the output spectrum changes from coherent DW to incoherent modulation instabilities just by changing from a constant to variable nonlinear parameters. This study can be extended to others solvents including ethanol, methanol, and butanol.

### 5.2.1. Introduction

Nonlinear phenomena occurring in different fiber optic structures have been extensively studied both theoretically and experimentally by both the scientific and engineering communities because they offer the possibility to control and guide light in many ways that differ from conventional approaches [2]. One such structure is a photonic crystal fiber (PCF), which has shown interesting applications in the areas of optical communications, metrology, spectroscopy, microscopy, astronomy, micromachining, biology, and sensing [72, 73]. One effect efficiently produced in PCF is the generation of a supercontinuum (SC), which has allowed the design of broadband and coherent light sources. The SC generation involves various well-known processes, such as self and cross-phase modulation, four-wave mixing, modulation instability, soliton fission, dispersive wave (DW) generation, and Raman scattering. Solitons and DWs are some of the phenomena that have helped contribute to the generation of new wavelengths toward the red and blue sides, respectively. A soliton is a pulse that either does not change its shape along the fiber length or follows a periodic evolution pattern, whereas DW is a type of radiation emitted by solitons, which is also called non-solitonic radiation (NSR)[74]. These effects can be modeled using the scalar nonlinear Schrodinger equation (NLSE)[2], which has been widely applied in numerical simulations.

New types of fiber optic structures have emerged as means to take advantage of the high nonlinear refractive index of some liquids [68]. These include filled liquid-core optical fibers and hollow core PCF (HCPCF), that can be filled with different types of liquids, including organic dyes, as a means to studying the nonlinear optical pulse propagating through them.

One liquid used is carbon disulfide ($CS_2$), which has shown a significant improvement in Super continuum generation (SCG); this type of fiber is referred to as liquid-core photonic crystal fiber (LCPCF).

In the case of liquids, within the Born–Oppenheimer approximation, the nonlinear responses have two components: an instantaneous response or bound-electron contribution, and a non-instantaneous response owing to the nuclei response. The latter of which can be understood as three independent responses, namely, a diffusive reorientation, vibrational response, and collision-induced contribution [70], in which each contribution has its own time response [37]. The theoretical prediction of existence of noninstantaneous soliton-like states in non-instantaneous nonlinear materials, where the molecular response is considered, shows that they are very robust to noise and point out the importance in the output when non-instantaneous response is considered [76]. Besides, it was found in $C_2Cl_4$ that the non-instantaneous effects can significantly reduce the modulation instability limit. i.e., noise driven FWM [77].

Other numerical studies of $CS_2$ filled fiber have not include the correct handling of the non-instantaneous response [78], [79]. In other hand, the pulse shape and pulse width dependence as the beam is propagated inside the medium is taken into account by Chemnitz et al, where they successfully use a propagation variant nonlinear parameter to match the measured DW with the simulation [80].

It is present a detailed theoretical study on dispersive wave and four-wave mixing generation during non-instantaneous nonlinear pulse propagation through a commercial HCPCF, the core of which is infiltrated with carbon disulfide ($CS_2$) and the pump wavelength is in the anomalous dispersion domain. It was demonstrated that there are differences in the nonlinear propagation model when taking into account the fact that the nonlinear refractive index changes as the pulse shape varies during its propagation. This can significantly affect the calculation of the DW and FWM, as demonstrated in the following section.

## 5.2.2. Ultrafast Non-instantaneous Propagation Model

### Nonlinear Propagation

In elongated liquid molecules, such as $CS_2$, the pulse propagation is dominated by non-instantaneous nonlinearities (molecular contributions) when ultrashort pulses are significantly shorter than the nonlinear response time of the liquid [68], and the total nonlinear refractive index can then be expressed as $n_{2,CS_2} = n_{el,CS_2} + n_{mol,CS_2}$, which contains the contributions, owing to the electronic ($n_{el,CS_2} = 2.0 \pm 0.4 \times 10^{-19} m^2/W$) and molecular responses [37].

The pulse evolution through the $CS_2$-LCPCF is simulated using the nonlinear schrödinger equation (NLSE) [2], given by Eq3-21 The second term on the left hand side of equation (3-

21) indicates the material losses, where $\alpha$ and $\alpha_1$ are the coefficients of the Taylor expansion of the total loss $\alpha(\omega)$. Nevertheless, the material losses are not of interest for the scope of this work. The third term of the left side of the equation involves the pulse dispersion in the medium, with $\beta_n$ being the nth dispersion term. The right-hand side shows the nonlinear terms inside the material as a result of the high-intensity pulse propagation, where $\gamma_1 \approx 1/\omega_o$ ($\omega_o$ is the pump frequency). The nonlinear response function $R(t)$ includes both the electronic and nuclear contributions. Assuming that the electronic contribution is nearly instantaneous, the functional form of $R(t)$ can be written as $R(t) = (1 - f_m)\delta(t) + f_m h_R(t)$. The molar fraction $f_m$ is calculated as $f_m = n_{2,mol}/(n_{2,el} + n_{2,mol})$. In addition,

$$h(t) = \frac{h'(t)}{\int_{-\infty}^{+\infty} h'(t)dt}. \tag{5-4}$$

$h'(t) = n_{2,d}r_d(t) + n_{2,l}r_l(t) + n_{2,c}r_c(t)$ is the characteristic response time of the nuclear mechanisms [37], given by the diffusive ($r_d(t)$), librational ($r_l(t)$), and collision ($r_c(t)$) contributions. Here, $n_{2,m}$ is the magnitude of the $mth$ mechanism, where $n_{2,d} = 18 \pm 3 \times 10^{-19} m^2/W$, $n_{2,l} = 7.6 \pm 1.5 \times 10^{-19} m^2/W$, and $n_{2,c} = 1.0 \pm 0.2 \times 10^{-19} m^2/W$ [37]. In addition, $r_m(t)$ is the temporal response function normalized such that $\int_{-\infty}^{+\infty} r_m(t)dt = 1$, as given by the following:

$$r_d(t) = C_d \left(1 - e^{-\frac{t}{\tau_{r,d}}}\right) e^{-\frac{t}{\tau_{f,d}}} \Theta(t) \tag{5-5}$$

$$r_l(t) = C_l e^{-\frac{t}{\tau_{f,l}}} \Theta(t) \int_0^{\infty} \frac{sin(\omega t)}{\omega} g(\omega)d\omega \tag{5-6}$$

$$r_c(t) = C_c \left(1 - e^{-\frac{t}{\tau_{r,c}}}\right) e^{-\frac{t}{\tau_{f,c}}} \Theta(t) \tag{5-7}$$

where $g(\omega) = e^{-\frac{(\omega-\omega_{os})^2}{2\sigma^2}} - e^{-\frac{(\omega+\omega_{os})^2}{2\sigma^2}}$, with $\omega_{os} = 8.5 \pm 1\ ps^{-1}$ and $\sigma = 5 \pm 1 ps^{-1}$ for $CS_2$. The remaining parameters in Eqs. 5-5, 5-6, and 5-7 are as follows: $\tau_{r,d} = 150 \pm 50\ ps^{-1}$, $\tau_{r,c} = 150 \pm 50\ ps^{-1}$, $\tau_{f,d} = 1610 \pm 50\ ps^{-1}$, $\tau_{f,l} = 450 \pm 100\ ps^{-1}$, and $\tau_{f,c} = 140 \pm 50\ ps^{-1}$ [37].

The molecular nonlinear refractive index is computed according to

$$n_{2,mol} = \frac{\int_{-\infty}^{+\infty} P(t,z) \int_{-\infty}^{+\infty} h'(t-t')P(t')dt'dt}{\int_{-\infty}^{+\infty} P^2(t,z)dt}, \tag{5-8}$$

where $P(t,z) = |A(t,z)|^2$ is the pulse power. Equation (3-21) was solved using a split-step Fourier method in which the nonlinear step was solved based on the fourth-order Runge–Kutta method. Finally, the nonlinear coefficient is calculated as follows:

$$\gamma = \gamma(\omega_0, T_0, z) = \frac{\omega_0 n_{2,cs_2}(T_0, z)}{cA_{eff}}, \tag{5-9}$$

where $\omega_0$ is the central pump frequency, $T_0$ is the pulse width, $c$ is the speed of light and $A_{eff}$ is the effective mode area of the fiber. From Eq. 5-9, it can be seen that $\gamma$ generally depends on the $Z$-propagation distance according to Eq. 5-8, a fact that has yet to be previously considered.

### 5.2.3. Dispersive Wave Generation

It is known that a dispersive wave is created by solitons in fiber optics [73], the frequency of which is calculated according the phase matching condition:

$$\sum_{m=2}^{\infty} \frac{\beta_m(\omega_s)}{m!}(\omega_d - \omega_s)^m = \frac{1}{2}\gamma P_s, \tag{5-10}$$

where $\beta_m(\omega_s)$ is the mth-order dispersion parameter at the soliton frequency $\omega_s$, $\omega_d$ is the DW frequency, and $P_s$ the soliton peak power. Considering the second- and third-order dispersion parameters, for the most energetic soliton, Eq. 5-10 can be rewritten as follows:

$$\Delta\nu_d T_o = \frac{1}{4\pi\delta_3}\left[1 + 4\delta_3^2(2N-1)^2\right], \tag{5-11}$$

where $\Delta\nu_d = \nu_d - \nu_s$, $N = N = \sqrt{L_D/L_{NL}}$ is the soliton order, and $T_o$ is the initial pulse width. In addition, $L_D = T_o^2/|\beta_2|$ represents the dispersive length, and $L_{NL} = 1/\gamma P_o$ is the nonlinear length. Here, $P_o$ is the initial peak power of the pump, and $\delta_3 = \beta_3/6|\beta_2|T_o$ is the normalized third-order dispersion. Eq. 5-10 is the most generalized case for calculating the DW frequency in $CS_2$ because $\gamma$ depends on $z$ as a consequence of the nonlinear molecular response. To the best of my knowledge, this situation has previously not been taken into account, and is described in the present study. In addition to Eq. 5-11, the DW peak power

can be calculated according to

$$p_d \approx \left(\frac{5\pi N}{4\delta_3}\right)^2 \left[1 - \frac{2\pi}{5}\left(2N-1\right)\delta_3\right]^2 exp\left[-\frac{\pi}{2\left(2N-1\right)\delta_3}\right] \tag{5-12}$$

Next, we compare the analytical results given by Eqs. 5-11 and 5-12, and the numerical results given based on the simplified and normalized NLSE:

$$\frac{\partial U}{\partial \zeta} + \frac{1}{2}\frac{\partial^2 U}{\partial \tau^2} + N^2|U|^2 U = i\delta_3 \frac{\partial^3 U}{\partial \tau^3}. \tag{5-13}$$

Here, $U(\zeta, \tau)$ is normalized such that $U(0,0) = 1$, and the other variables are $\zeta = z/L_D$ and $\tau = T/T_o$. In Eq. 5-13, $\beta_2$ is negative. In Eq. 5-13, we include $\gamma_1$ and $R(T)$ from Eq. 3-21 in order to study the higher-order nonlinearities and analyze the influence of the molecular response.

### 5.2.4. Four-Wave Mixing

In single-mode fiber optics, FWM can be initiated using a single pump beam, which is the case of a degenerated FWM. A pump beam with a frequency of $\omega_1$ can create two sideband frequencies located symmetrically at $\omega_3$ and $\omega_4$ through the following shift [2]:

$$\Omega_s = \omega_1 - \omega_3 = \omega_4 - \omega_1, \tag{5-14}$$

where $\omega_3 < \omega_4$ is assumed. Here, $\omega_3$ is called the Stokes band, and $\omega_4$ the anti-Stokes band. To efficiently create the FWM, the following phase matching condition needs to be achieved [2]:

$$\kappa = \Delta k_M + \Delta k_W + \Delta k_{NL} = 0, \tag{5-15}$$

where $\Delta k_M$, $\Delta k_W$, and $\Delta k_{NL}$ are mismatches as a consequence of a material dispersion, waveguide dispersion, and the nonlinear effects, respectively.

When the pump wavelength is within the anomalous GVD regime, the frequency shift $\Omega_s$

depends on the input power and is given as

$$\Omega_s = (2\gamma P_0/|\beta_2|) \tag{5-16}$$

## 5.2.5. Geometry and Optical Parameters

For the simulations, we used the commercial HCPCF HC-800B, sold by Thorlabs, with the following parameters: core diameter of 7.5 $\mu$m, cladding pitch of 2.3 $\mu$m, PCF region diameter of 45 $\mu$m, and cladding diameter of 130 $\mu$m. It was assumed that the core is filled with carbon disulfide ($CS_2$), and finite element software was used to obtain the dispersion behavior (see Fig. **5-1**) and the effective area; the Sellmeir equation for $CS_2$ is required for these calculations, which is given by [81]

$$\begin{aligned} n_{CS_2}(\lambda) = 1.580826 + 1.52389 \times 10^{-2}/\lambda^2 + \\ 4.8578 \times 10^{-4}/\lambda^4 - 8.2863 \times 10^{-5}/\lambda^6 + \\ 1.4619 \times 10^{-5}/\lambda^8. \end{aligned} \tag{5-17}$$

The effective area was calculated according to the relation [2]:

$$A_{eff} = \frac{(\iint_{-\infty}^{\infty} |F(x,y)|^2 \, dxdy)^2}{\iint_{-\infty}^{\infty} |F(x,y)|^4 \, dxdy}, \tag{5-18}$$

where $F(x, y)$ is in general the modal distribution function of the beam. After calculating the effective area, Eq. 5-9 is used to compute $\gamma$. We found that the zero-dispersion wavelength of the $CS_2$ filled fiber is 1.86 $\mu$m (see Fig. **5-1**). The pump wavelength was set to 1.95 $\mu$m in order to ensure anomalous dispersion regime propagation with the aim of generating optical solitons.

## 5.2.6. Numerical Simulations

For the present study, it was solved the nonlinear Schrödinger equation 3-21 by implementing the typical split-step Fourier method (SSFM) [2]. For a case in which $\gamma$ is considered to be dependent on the shape and width of the pulse, we recalculated the nonlinear refractive

index $n_{2,cs_2} = n_{el,CS_2} + n_{mol,CS_2}$ at each step in the SSFM using Eq. 5-8. In Fig. **5-5**, the difference in the nonlinear temporal evolution vs. distance with $\gamma$ both as a constant and as a variable using Eq. 5-13 is shown as an example. In this figure, the power is represented by a color scale between orange and black, the brighter the color the higher the power. It can be clearly observed that, when $\gamma$ is considered a variable, the DW travels slower with respect to when it is considered a constant. This makes sense because the non-instantaneous response of $CS_2$ molecules increases as the pulse width widens and the pulse shape changes, which verifies the assumption that $\gamma$ should be considered a variable for materials with a non-instantaneous response.

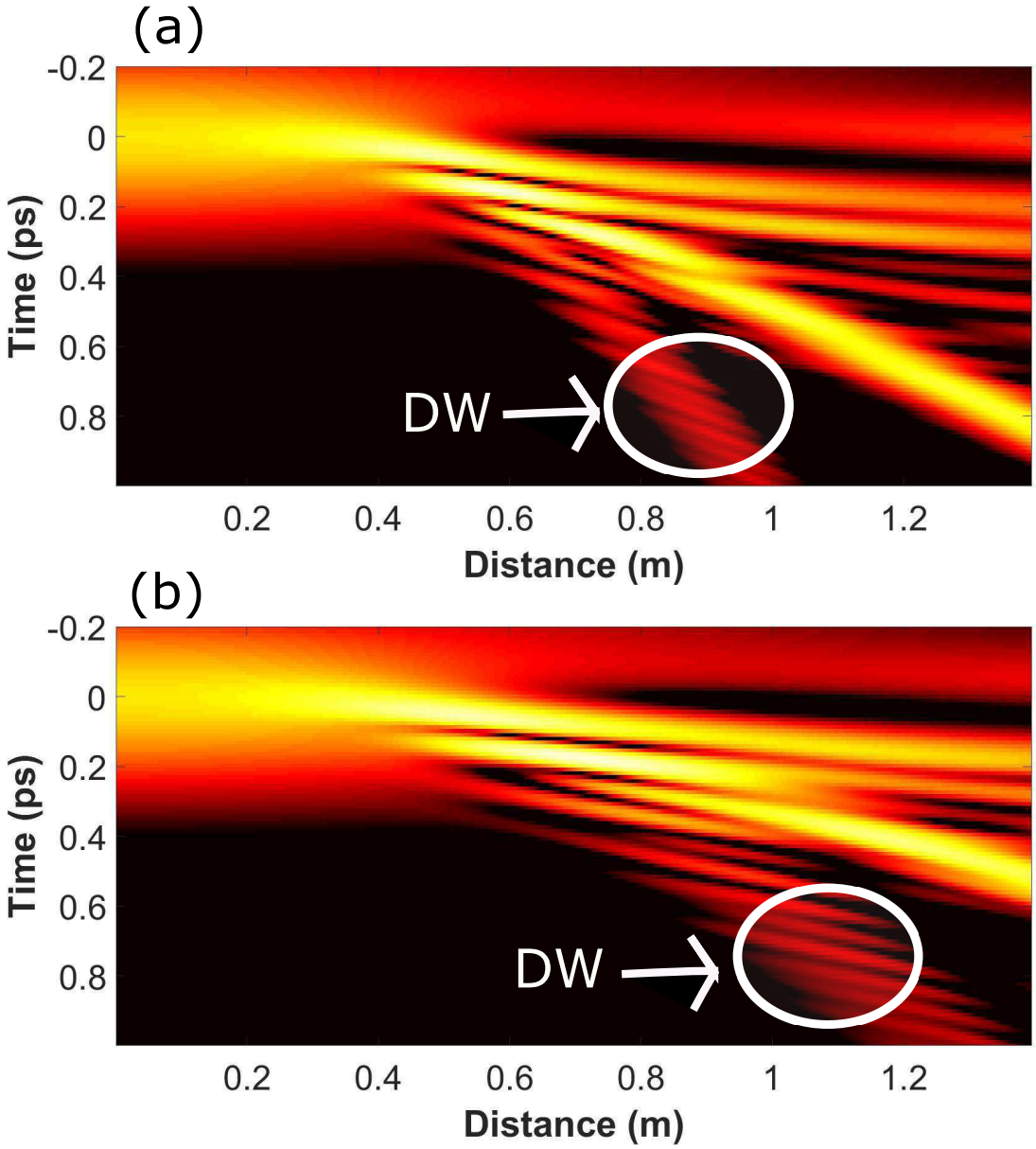


**Figure 5-5**.: Nonlinear time evolution considering $\gamma$ as (a) a constant and (b) a variable, and is set to $T_0 = 0.17$ ps, with a propagation length of $0.5L_D$, $\delta_3 = 0.08$, and $N = 3$

For the following simulations, it was considered different pulse widths: $T_{FWHM} = 107$ fs, 200 fs, 300 fs, and 500 fs, as well as variations of $\delta_3$ from 0.01 to 0.1. Here, $T_{FWHM}$ is the full width at half maximum of the pulse, which relates to $T_0$ according to the expression $T_{FWHM} = 1.763T_0$ for the "*sech*" pulses.

### 5.2.7. Dispersive Wave Calculations

Using Eq. 5-12, it was investigated the DW power behavior as a function of $\delta_3$ and $N$ when $\gamma$ is either a constant or a variable for different pulse widths. For the figures where the power is expressed in dB, 0 dB is reached when the output power is equal to the input power. Fig. **5-6** shows the power behavior for different pulse widths, where (a) and (c) correspond to $T_{FWHM} = 107$ fs, (b) and (d) correspond to 200 fs, and the theoretical prediction is given in Eq. 5-12 with $\gamma$ as a constant. It is worth noting that the theoretical prediction does not fit well with the simulations in which, at higher pulse widths, Eq. 5-12 fails more significantly. Another important point is the fact that an appreciable DW is generated when the output power is higher than -80 dB, which varies according to pulse width, soliton number, whether $\gamma$ is considered a constant or variable and the presence of nonlinear terms (NT) such as a shock wave and Raman response. Here, the absence of Raman response could be interpreted as a system in the likes of a glass core fiber or noble gas-filled fiber, whereas a system which presents a Raman response at the output corresponds to a realistic liquid-core fiber. The pulse width has an important role in the DW generation, as indicated based on the comparison between Fig. **5-6**(a) and Fig. **5-6**(b), and Fig. **5-6**(c) and Fig. **5-6**(d), where, at lower pulse widths, a stronger DW with a lower $\delta_3$ can be obtained for the same soliton number. In the presence of NT, the DW power decreases, as expected, because the Raman effect shifts the solitons toward longer wavelengths. The match between the theoretically calculated DW power and the simulations (either with $\gamma$ as constant or variable as well as with or without NT) can be seen as a balance between energy ($N$) and pulse width, for example Fig. **5-6** (a) and Fig. **5-6** (d) are different from the theoretical prediction but (b) and (c) differ only slightly. In addition, between cases (a) and (d) and cases (b) and (c) there are similarities in behavior: in (b) the pulse width is increased in comparison with (a), in the same way in (c) the pulse width is decreased in comparison with (d).

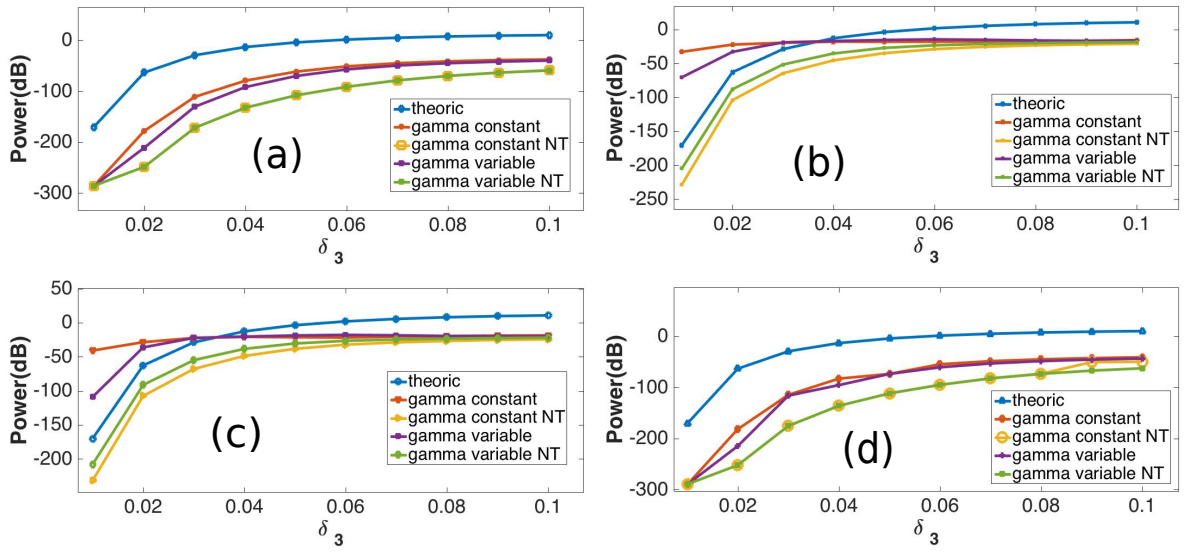


**Figure 5-6**.: DW Power (dB) as a function of $\delta_3$ for different $N$ and $T_{FWHM}$: (a) $N = 2$, $T_{FWHM} = 107$ fs, (b) $N = 2$, $T_{FWHM} = 200$ fs, (c) $N = 3$, $T_{FWHM} = 107$ fs, and (d) $N = 3$, $T_{FWHM} = 200$ fs

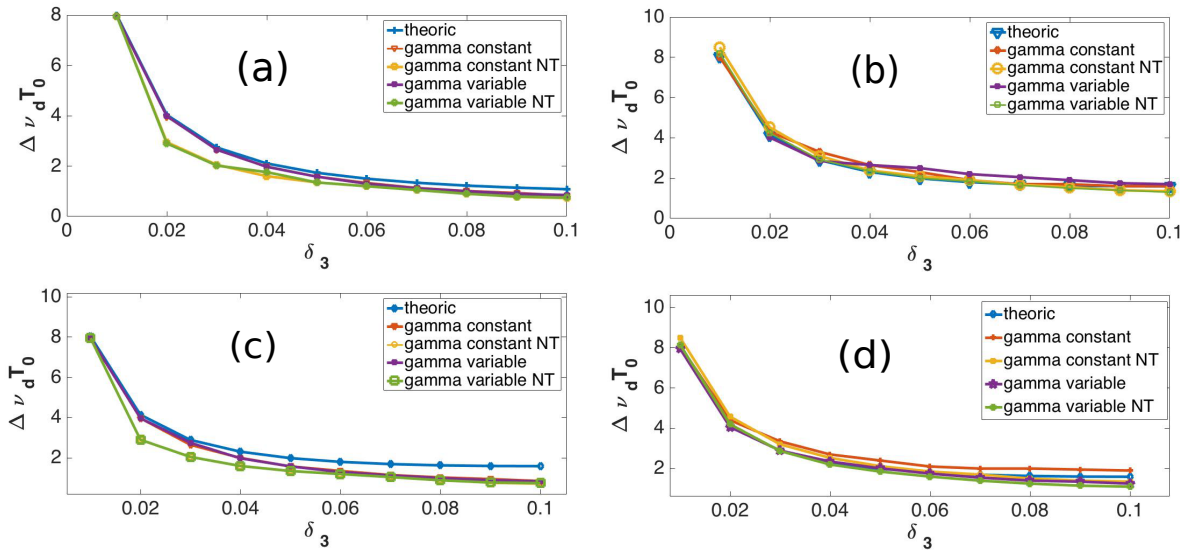


**Figure 5-7**.: DW frequency as function of $\delta_3$ for (a) $N = 2$ and $T_{FWHM} = 107$ fs, (b) $N = 2$ and $T_{FWHM} = 200$ fs, (c) $N = 3$ and $T_{FWHM} = 107$ fs, (d) $N = 3$ and $T_{FWHM} = 200$ fs

Next, it was examined what will happen if the pulse width is wider compared with the previous cases and if the soliton number is increased. Fig. 5-8 shows how the DW power

is affected by the soliton number as a function of $\delta_3$. Two scenarios are taken into account, namely, $N = 3$ and $N = 9$, and the pulse width is set to 300 fs. The major difference between Fig. 5-8(a) and Fig. 5-8(b) is the fact that for $N = 9$, there is more discrepancy with the theoretical results. As mentioned, in Fig. 5-6 it can be seen that, at higher pulse widths, the DW powers are almost the same for $\gamma$ and $\gamma(z)$, which does not exactly occur in Fig. 5-8, only after the values of $\delta_3$ are higher than 0.03.

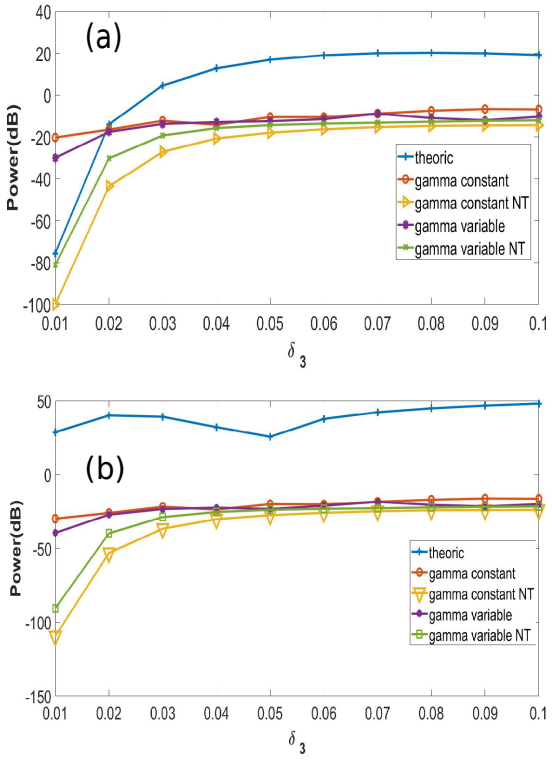


**Figure 5-8**.: DW Power (dB) as a function of $\delta_3$ for (a) $N = 3$ and (b) $N = 9$ at $T_{FWHM} =$ 300 fs

Continuing the study with the wavelength at which the DW is generated; according to Eq. 5-11, this value depends on $\gamma$ and $\delta_3$. The Z-dependence of $\gamma$ opens the possibility to investigate how this parameter affects the DW behavior. Fig. 5-7 shows how the DW frequency varies as a function of $\delta_3$ for different pulse widths and numbers of solitons when the nonlinear terms are, or are not, included.

Although the theoretical expression cannot exactly predict the values obtained in the simulations, it does work better with lower values of $\delta_3$. No particular differences are shown in the DW frequencies when $\gamma$ is considered a variable or constant, although differences do occur when the nonlinear terms are considered, mostly for values of approximately 0.02 and 0.06; different situations were reported in ref. [74], which uses a constant $\gamma$ and silica fiber, although the geometry and response function of the material are different. The previous

analysis suggests that the dispersive wave depends not only on the energy of the soliton, but also on the shape of the propagating pulse.

Although the DW phase matching condition ($\Delta\nu_d T_o$) is almost the same in Fig. **5-7** for $\gamma$ and $\gamma(z)$, it is interesting to see how $\gamma(z)$ influences the DW frequency. To study this, fig. **5-9** illustrates this dependence. One important feature regarding how $\gamma$ as a constant or variable affects the spectrum can be seen in figs. **5-9**(a) and **5-9**(c), respectively, where the difference in the DW generation is clear: whereas in (a), where $\gamma$ is a constant, and the DW starts to appear, in (b) no DW generation has yet occurred, and the coherent DW change to incoherent modulation instability. Another important aspect regarding these two spectra is related to the fission process. In fig. **5-9**(a), the spectrum exhibits little fission, and there are two main peaks, whereas in fig. **5-9**(c), the spectrum has two lateral frequencies with respect to the central one, and the fission process is clearly more important when $\gamma$ is a variable. A similar behavior is demonstrated when $\beta_3 = 0$ and only $\beta_4$ are considered in Eq. 5-13. If higher-order nonlinear terms are taken into account in Eq. 5-13, the fission process disappears in both cases, as shown in figs. **5-9**(b) and **5-9**(d) for $\gamma$ as both a constant and a variable, respectively; additionally, it can be seen that the spectral responses are similar.

However, we found that, at narrower pulse widths ($T_o$), the differences between the spectra are smaller, and the influence on the variation of $\gamma$ based on the position is negligible; however, for wider pulse widths, the differences are more remarkable and the symmetrical behavior found in fig. **5-9** is no longer present. Similarly, the DW disappears when higher-order nonlinear terms are considered. Another notable finding was the influence of the $\delta_3$ parameter. As it is increased, the output spectra become the same regardless of the pulse width or higher-order nonlinear terms.

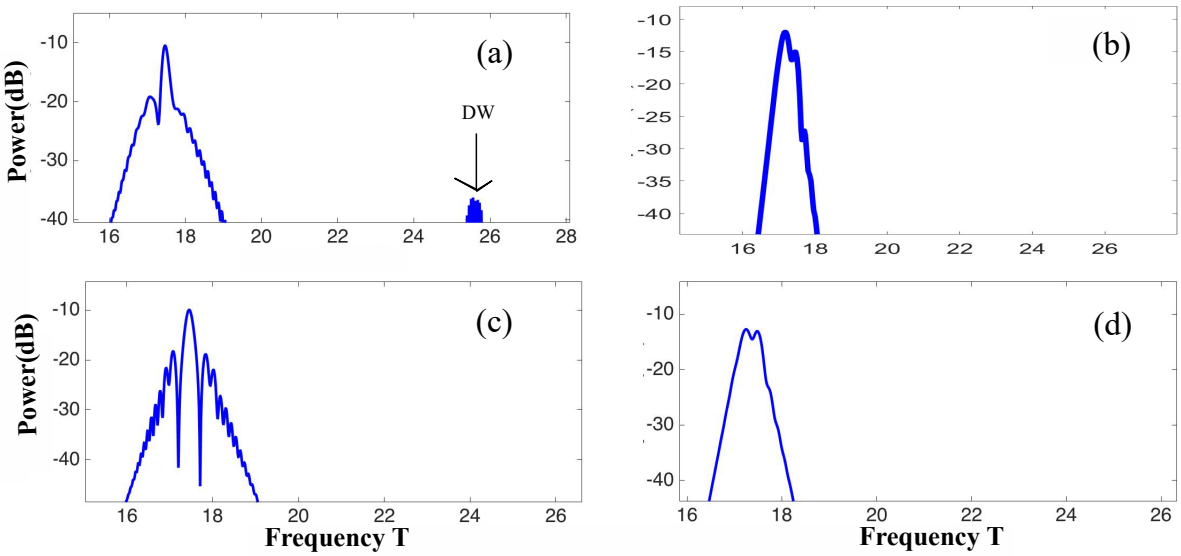


**Figure 5-9**.: Output spectrum at $T_{FWHM} = 200$ fs, $\delta_3 = 0.01$, and $N = 3$ for (a) $\gamma$ as a constant without higher-order nonlinear terms, (b) $\gamma$ as a constant with higher-order nonlinear terms, (c) $\gamma$ as a variable without higher-order nonlinear terms, and (d) $\gamma$ as a variable with higher-order nonlinear terms.

When the pulse width remains constant at $T_{FWHM} = 300fs$ and the soliton order is increased up to $N = 9$, an interesting behavior appears, that is, the differences in the spectra between $\gamma$ and $\gamma(z)$ are presented again, even for the largest values of $\delta_3$, and when considering higher-order nonlinear terms.

In summary, there are different parameters that affect the dispersive wave generation under the assumption of a constant or variable $\gamma$. Increasing both the pulse width and $N$, the spectra present differences, whereas increasing $\delta_3$ makes both spectra the same.

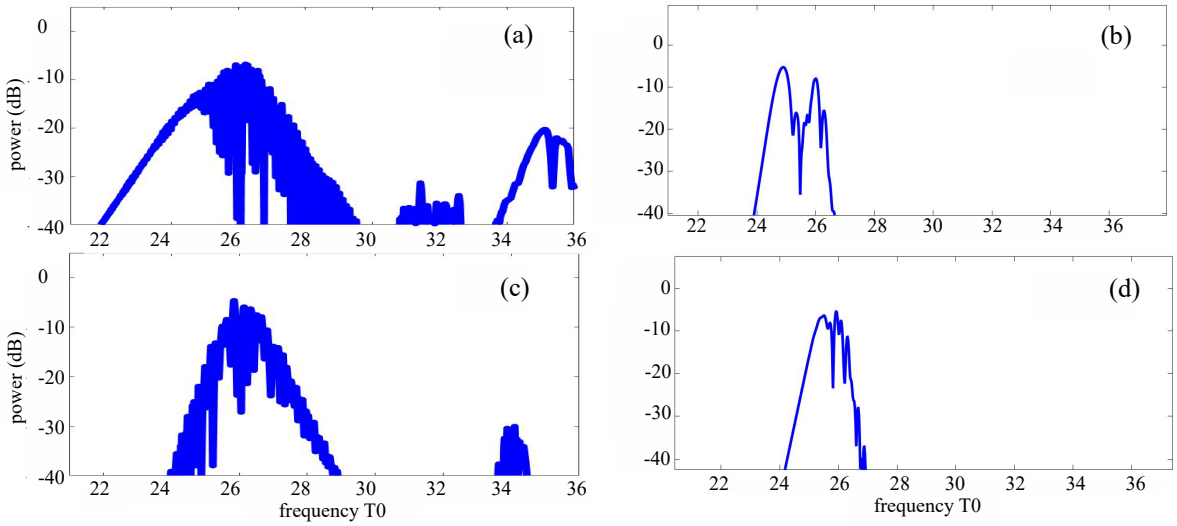


**Figure 5-10**.: Output spectrum at $T_{FWHM} = 300$ fs, $\delta_3 = 0.01$, and $N = 3$ for (a) $\gamma$ as a constant without additional nonlinear terms, (b) $\gamma$ as a constant with additional nonlinear terms, (c) $\gamma$ as a variable without additional nonlinear terms, and (d) $\gamma$ as a variable with additional nonlinear terms

The variation in the dispersive wave can be explained as a consequence of the dependence of $\gamma$ as a function of the shape of the pulse when propagating, and therefore the soliton order changes as well. Fig. 5-11 shows the behavior of $\gamma(z)$ and $N(z)$ for the initial values of $N = 3$ and $N = 9$ at $T_{FWHM} = 300$ fs, where we can observe that initially $\gamma(z)$ decreases dramatically to a certain distance, and after reaching a minimum value, increases rapidly. This is due to $n_2$ depends on the shape of the pulse and that before the fission of the solitons, the pulse is compressed and then widened.

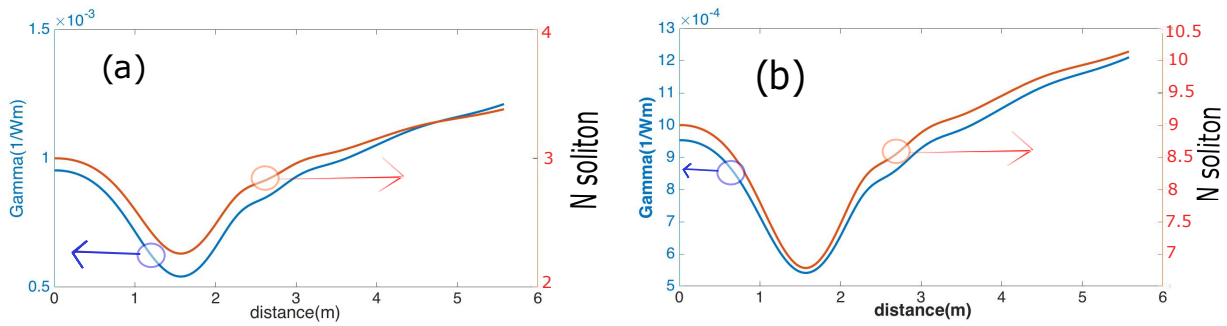


**Figure 5-11**.: $\gamma(z)$ and $N(z)$ evolution as a function of propagation distance at $T_{FWHM} = 300$ fs with initial soliton order of (a) $N = 3$ and (b) $N = 9$. The blue curve corresponds to gamma whereas the red one corresponds to soliton number N

According to Eq. 5-11, the DW frequency can be controlled using $\delta_3$, $T_0$, $\beta_2$, $\gamma$, and the initial power $P_o$. Typically, the only way to change the frequency externally to the fiber optic structure is to manipulate the initial power of the pulse. Thus, if a solvent material, such as $CS_2$, is used, where $\gamma$ depends on the propagation distance, we can also manipulate the length of the fiber structure infiltrated with $CS_2$ and thereby select the DW frequency.

Fig. **5-12** shows $\Delta\nu_d$ as a function of distance for different cases of $\gamma$ as a variable. It is worth noting in Fig. **5-12**(c) that the DW frequency was unaltered; however, the situation is different in Fig. **5-12**(a), where the only change made was in the pulse width $T_{FWHM} = 107$ fs. This indicates the possibility of finding balance among the different parameters so as to create the desired spectrum. A second notable finding on the influence of the $\delta_3$ parameter is that for the highest value of $\delta_3$ considered ($\delta_3 = 0.1$), the mismatch between the theoretical and simulated values of $\Delta\nu_d$ was also the highest. Similarly, at $\delta_3 = 0.1$ for a propagation distance lower than 3 meters the DW power was the lowest. This can be considered the initial point when designing a tunable DW frequency device, where we can control the wavelength and power, and when experimenting with both the parameters mentioned above and the propagation distance.

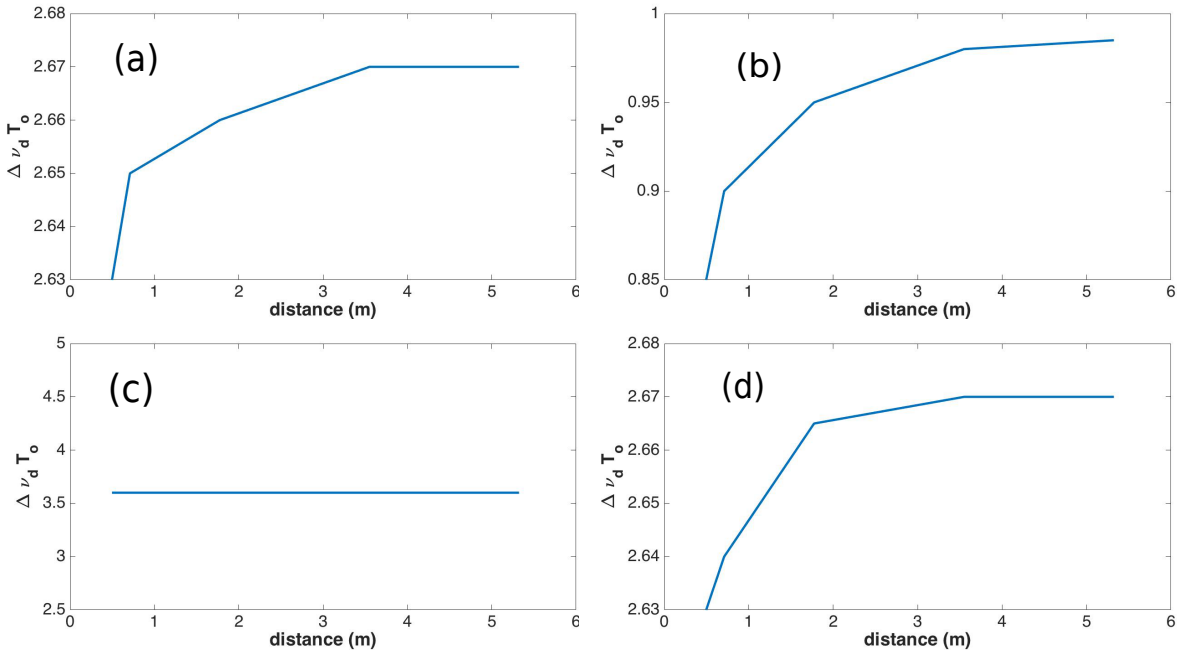


**Figure 5-12**.: Variation of $\Delta\nu_d$ with distance for (a) $N = 2$, $T_{FWHM} = 107fs$, and $\delta_3 = 0,03$, (b) $N = 2$, $T_{FWHM} = 107$ fs, and $\delta_3 = 0,09$, (c) $N = 2$, $T_{FWHM} = 300$ fs, and $\delta_3 = 0,03$, and (d) $N = 9$, $T_{FWHM} = 107$ fs, and $\delta_3 = 0,03$.

### 5.2.8. Four-Wave Mixing

An interesting fact occurs when the pulse width is set to 500 fs, namely, the output spectrum is very broad, making it very difficult to identify the DW, soliton fission, or other phenomena. For this reason, it was followed the pulse evolution for different propagation distances to see how it behaves and to determine the main differences with its counterparts, $\gamma$ and $\gamma(z)$. In this case, we neglected higher-order nonlinear terms. In Fig.**5-13**, at a propagation length of $0.02L_D$ the output spectral shape was almost the same for each case under consideration. It is until a propagation distance of $0.067L_D$ that significant differences occur with $\delta_3 = 0.1$, where stoke and anti-stoke waves start to appear, the difference can be appreciated between Fig.**5-13** (c.4) and Fig.**5-13**(d.4). For the remaining figures, it can be seen that the frequency of the stoke and anti-stoke waves are at the same position, independent of whether $\gamma$ is a constant or variable, and these frequencies agree with Eq. 5-14 and Eq. 5-16. However, the form of the spectral responses are dependent on whether $\gamma$ is a variable or constant, even for certain situations in which one or both of the waves disappear.

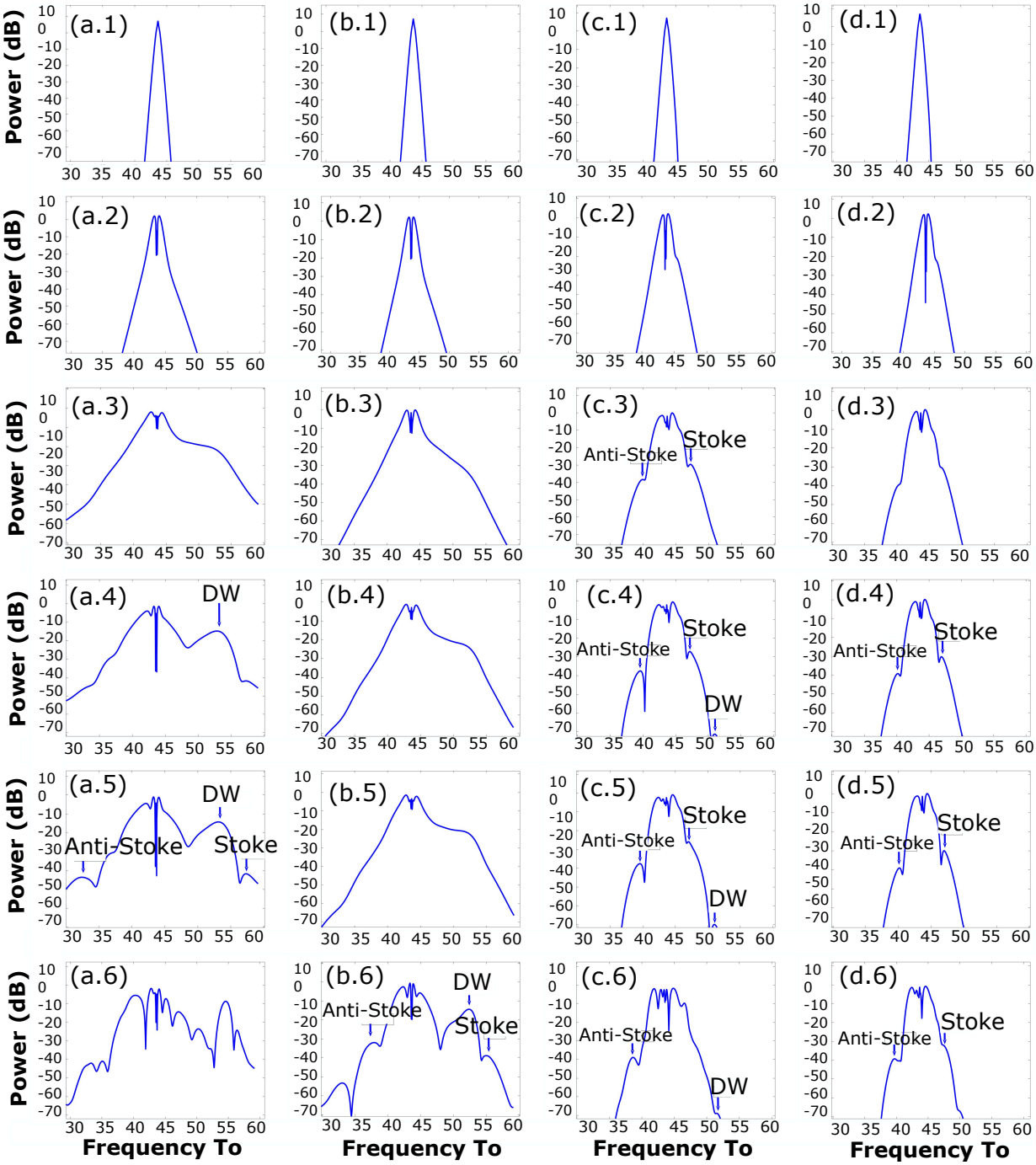


**Figure 5-13**.: Output spectrum shape for different propagation distances: (a) $\delta_3 = 0,01$, and $\gamma$ as a constant, (b) $\delta_3 = 0,01$, and $\gamma$ as a variable, (c) $\delta_3 = 0,1$, and $\gamma$ as a constant, and (d) $\delta_3 = 0,1$, and $\gamma$ as a variable. Where the first row until the last go as: $0.02L_D$, $0.05L_D$, $0.067L_D$, $0.069L_D$, $0.07L_D$, $0.08L_D$

## 5.3. Hollow Core Photonic Crystal Fiber Simulation

Hollow-core photonic crystal fibers infiltrated with Argon, Krypton and Xenon were simulated, for this purpose the GNLSE (Eq 3-21) was numerically solved. We considered different pulse widths: $50fs$ and $500fs$ as well as peak power as a function of critical power: $\frac{1}{8}P_{cr}$, $\frac{1}{50}P_{cr}$, $\frac{1}{100}P_{cr}$ and $\frac{1}{100}P_{cr}$, where:

$$P_{cr} = \frac{\lambda^2}{2\pi n_0 n_2} \tag{5-19}$$

$\lambda$, $n_0$ and $n_2$ are input wavelength, linear and non-linear refractive index, respectively. The Critical power is defined as the threshold necessary to start the ionization of the gas, in this way, ensuring a lower power than the critical, it is not necessary to include a new nonlinear term in Eq 3-21 to take into account this new phenomenon, where new effects are generated. The pressure under consideration was varied: 1 bar, 25 bar, 90 bar, 140 bar. The input wavelength was set to 800 nm, with a unchirped Gaussian profile. The HCPCF geometry considered is shown in Fig **5-1** and the beam inside power distribution was solved by a finite element modeling.

### Argon

The dispersion profile of Argon for each pressure level is shown in Fig **5-14** where it can appreciated how it varies according to pressure, an interesting fact is the presence of multiple zeros at different wavelengths. These zeros are shifted with the change in pressure. Due to the method used to calculate the dispersion profile, the values close to the boundaries are not trustworthy.

Although in some cases the pump wavelength was not in the anomalous dispersion regime, the dispersion shape was of special interest as in some cases a spectral broadening can be achieved, this is when the pulse width is broad enough to reach wavelengths were the dispersion is negative and a soliton can be generated. Fig **5-15** presents how the nonlinear parameter $\gamma$ and $\beta_2$ varies according to pressure level. The behavior presented by $\gamma$ is expected due to the increase in nonlinear refractive index ($n_2$) and density of the gas with pressure [3], besides the shape of the graph coincides at the pressure at which the gas changes to supercritical state. However, in Fig **5-15**(b) the $\beta_2$ parameter calculated at 800 nm has not a clear dependence with pressure, but it is demonstrated how this value can be shifted through positive and negative values (normal and anomalous dispersion). It opens the possibility to generate optical solitons with the same fiber structure and laser, only with the change of pressure, a relatively simple and low cost implementation.

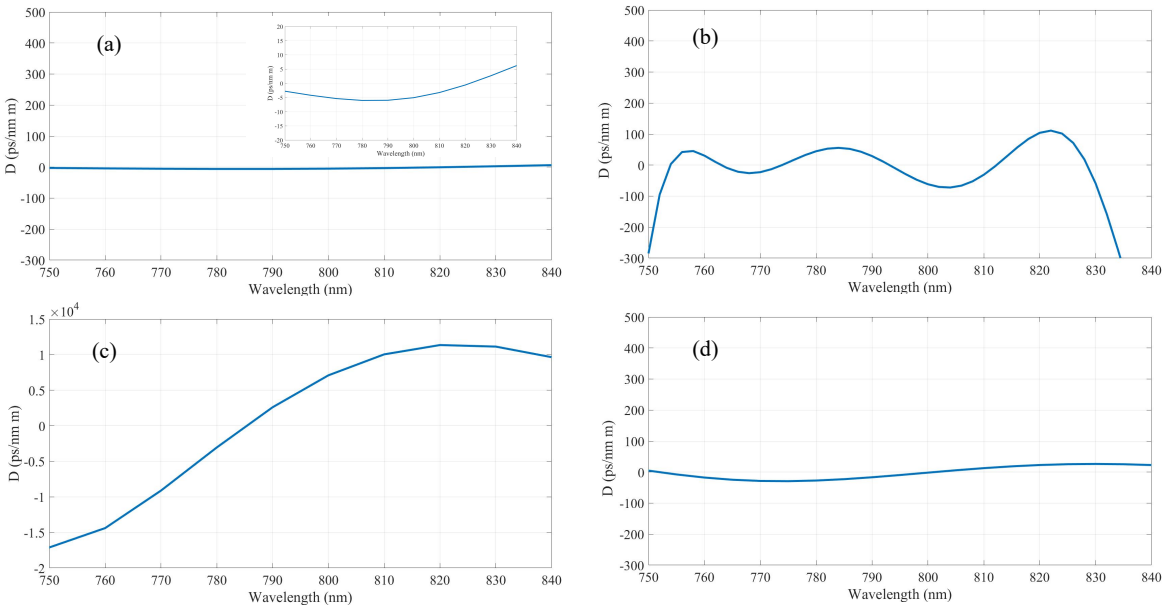


**Figure 5-14**.: Argon dispersion profile. (a) 1 bar, (b) 25 bar, (c) 90 bar, (d) 140 bar

For 140 bar there was no confinement inside the fiber at 800 nm, for this reason simulations were perform until 90 bar. For 50 fs pulse width the output spectrum was nearly the same that the input for every pressure and input power, this situation is presented in Fig **5-16**(b). At the same pulse width the temporal output get distorted, where it lost its initial profile and it extends for more than 80 ps without principal shape. A total different picture occurs when the pulse width is change to 500 fs, an interesting pulse shift and compress take place at 90 bar, where the pulse breaks into two main pulse: one travel at almost the same velocity that the input pulse and the other traveling slower, but with a temporal compression, where its Gaussian shape is conserved **5-16** (a). At 25 bar and 1 bar the temporal output is broader and no specific pulse or shape is formed. In other hand, at 90 bar occurs the most significant spectrum change, where it can be observed two main peaks, at 775 nm and 835 nm. The first one can be attributed to DW generation(Eq 3-39) , whereas the second (835 nm) can not be due to Raman effect because in noble gases this effect is not present, so the most probably reason is dispersive terms that act to form this new wave, as was reported in previous works [13],[74]. The reason why in (c) the output spectrum at 1 bar suffers such deformation with different peaks along different wavelengths whereas at 25 bar the pulse remains almost the same is due to the value of $\beta_2$ and $\gamma$. For both pressures $\beta_2$ is positive, but for 1 bar the value is lower than for 25 bar (table **5-2**), whereas the opposite situation occurs for $\gamma$, where the value corresponding to 25 bar exceeds to 1 bar. In this way, for 1 bar $L_{NL}$ is lower than for 25 bar making the nonlinear phenomena the main effects over the pulse propagation. For 25 bar $L_D$ is shorter than $L_{NL}$ and the interplay between these two effects enable the compensation to keep the pulse narrowed.

| Argon | | | | | | | | | |
|---|---|---|---|---|---|---|---|---|---|
| **Pressure** | $\beta_2$ $ps^2/m$ | $\beta_3$ $ps^3/m$ | $\beta_4$ $ps^4/m$ | $\beta_5$ $ps^5/m$ | $\beta_6$ $ps^6/m$ | $\beta_7$ $ps^7/m$ | $\beta_8$ $ps^8/m$ | $\beta_9$ $ps^9/m$ | $\beta_{10}$ $ps^{10}/m$ |
| **1 bar** | 1.548 | 0.038 | $-4.435\cdot 10^{-04}$ | $-4.773\cdot 10^{-06}$ | $9.849\cdot 10^{-08}$ | $1.407\cdot 10^{-10}$ | $-1.260\cdot 10^{-11}$ | $7.510\cdot 10^{-14}$ | $-1.537\cdot 10^{-22}$ |
| **25 bar** | 21, 528 | $-0.264$ | $-0.060$ | 0.001 | $1.328\cdot 10^{-04}$ | $-5.303\cdot 10^{-06}$ | $-1.537\cdot 10^{-07}$ | $8.692\cdot 10^{-09}$ | $-1.046\cdot 10^{-12}$ |
| **90 bar** | $-1, 096$ | 0.045 | $2.137\cdot 10^{-04}$ | $-8.182\cdot 10^{-06}$ | $-7.276\cdot 10^{-08}$ | $8.703\cdot 10^{-10}$ | $1.645\cdot 10^{-11}$ | $7.477\cdot 10^{-14}$ | $-1.481\cdot 10^{-23}$ |

**Table 5-2**.: Dispersion parameters used to simulated Argon filled HCPCF

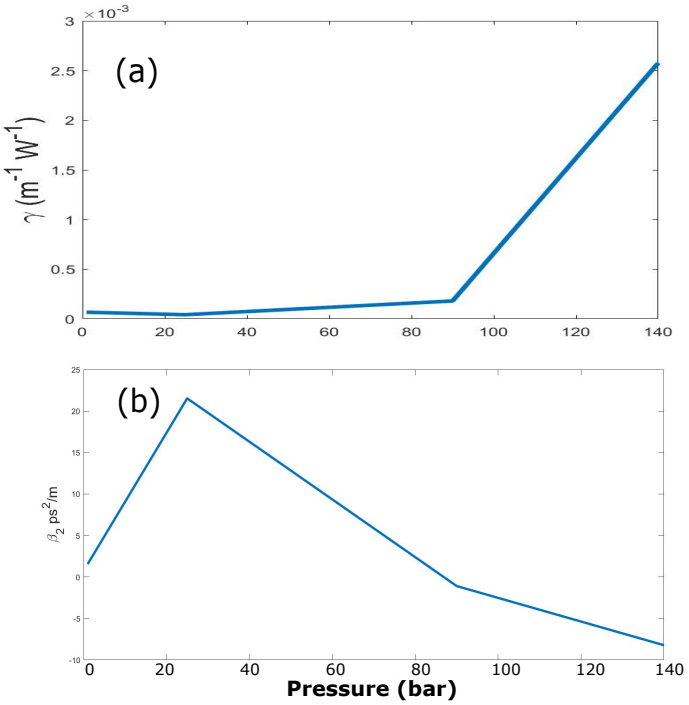


**Figure 5-15**.: (a)$\gamma$, (b) $\beta_2$ in function on pressure for Argon in HCPCF

It is interesting to see that the most important effects on the pulse occur at 90 bar, where $\gamma$ reaches its maximum value and $\beta 2$ is negative, enabling the soliton formation and a subsequent DW formation. It is at this pressure that the gas changes its linear behavior to enter in the supercritical zone. Despite that the temporal width was increased, this was not enough to excite other wavelengths in which a wave could be propagated in anomalous dispersion for the pressures where $\beta_2$ was positive at 800 nm. Nevertheless, the dispersion profile associated to this fiber geometry could be further explorer with the intention of spectral broadening at normal dispersion wavelength.

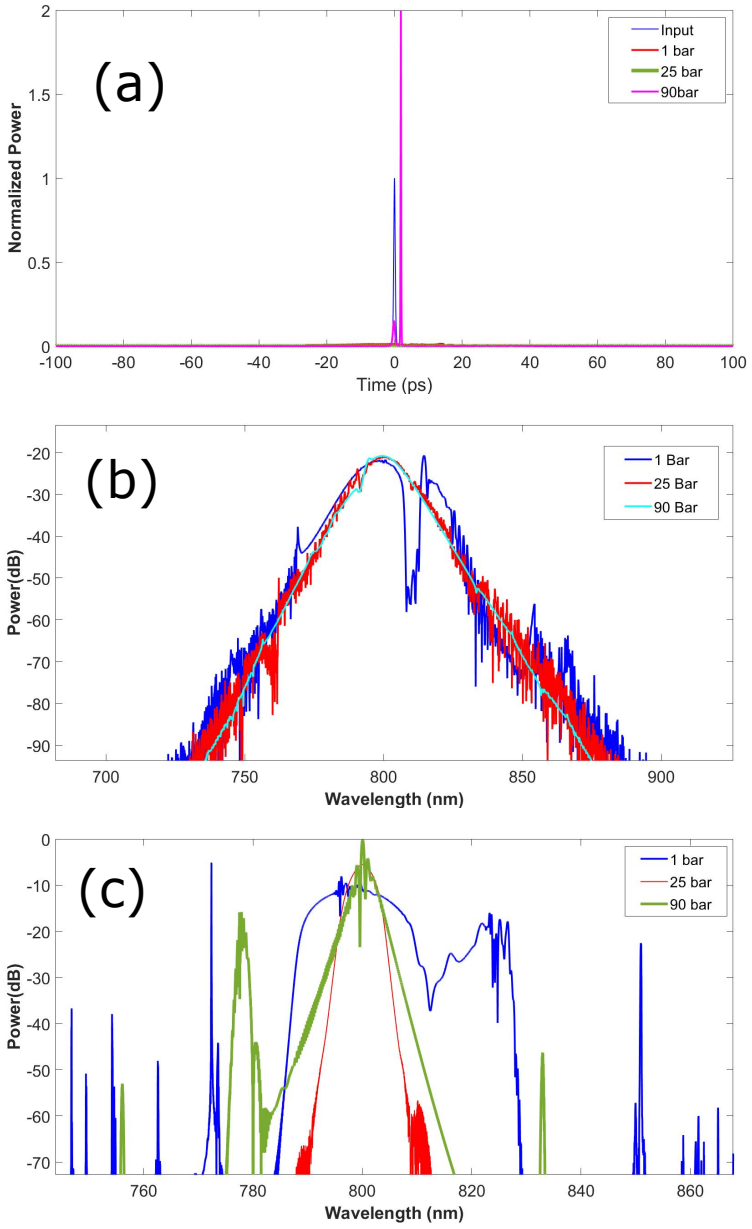


**Figure 5-16**.: output response in Argon filled HCPCF for different pressures and pulse widths after 1 m of propagation distance and 1/50 Pcr. (a) Output time response at 500 fs pulse width. (b) output spectrum at 50 fs pulse width. (c) output spectrum at 500 fs pulse width

### Xenon and Krypton

The Xenon and Krypton dispersion profile was investigated, where it was found that both gases are not confined by the HCPCF geometry considered for pressures higher than 40 bar. In the same way, the profile exhibited by both gases was similar to Argon where multiple ZDW were found. According to this, a study in function of power, pulse width and pressure was done.
At 50 fs neither Xenon and Krypton exhibited a significant change in their output spectrum or temporal response, despite the fact that $\beta_2 < 0$ and optical soliton could be formed, but the dispersive terms turn out to exceed the nonlinear ones, making a low nonlinear interaction. It was only when the pulse width was change to 500 fs that changes in the output pulse occurs. In Fig **5-19** (a) and (c) is shown the output spectrum for Xenon and Krypton respectively, where a similar behavior was found: at 1 bar occurs broader spectral broadening that at 25 bar, nevertheless the pulse shape presents a lot of picks around the initial pulse shape. The reason for this behavior is found when the $\gamma$ and $\beta_m$ dependence with pressure is considered. In the case of Xenon at $1bar$, $N = 4$ and $L_{NL}$ is ten times lower than $L_D$, which implies the nonlinear phenomena preponderance over dispersive ones, nevertheless in the propagation distance considered (1 m), both effects have impact on the final shape.

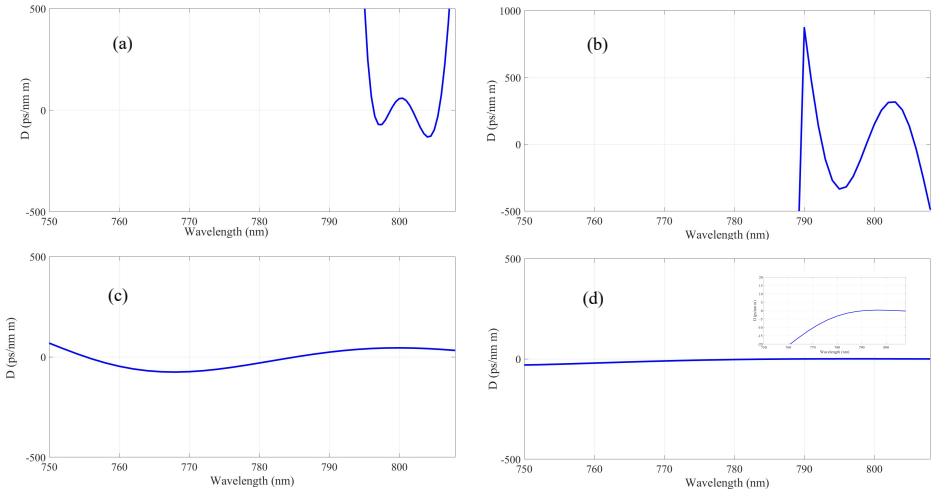


**Figure 5-17**.: Xenon Dispersion profile in HCPCF. (a) 1 bar. (b) 25 bar. (c)90 bar. (d)140 bar

So, first the pulse undergoes nonlinear effects, such as soliton fission, modulation instability, among others, and then the higher dispersive terms acts in each pulse produced by the first action. Explaining the number of peaks around a central shape, where the soliton fission can be appreciated. In the same way for Krypton, at 1 bar $L_{NL}$ is shorter than $L_D$, but

this difference is lower than Xenon, which it explains the lower number of peaks around the main shape, with the addition of a small soliton order, $N = 2$.

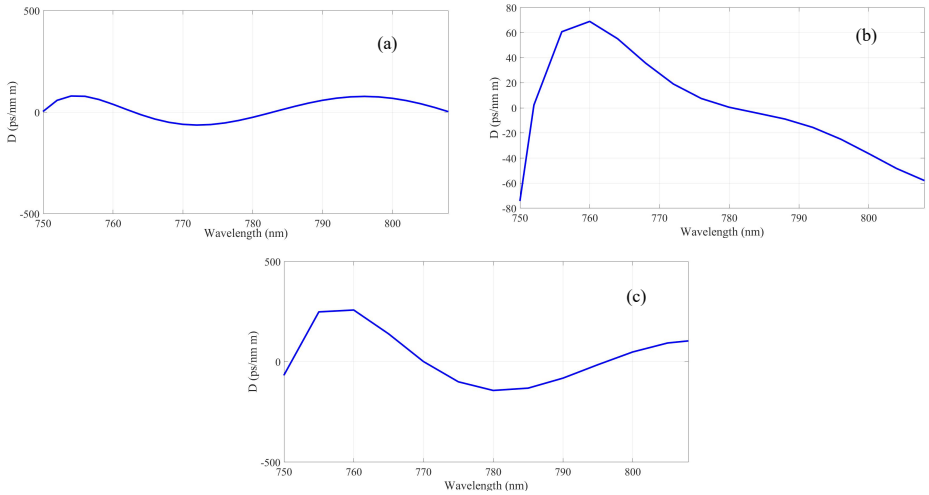


**Figure 5-18**.: Krypton dispersion profile in HCPCF. (a) 1 bar. (b) 25 bar. (c)90 bar.

The influence of soliton number in the final pulse shape can be evidenced in Fig **5-19**(a) at 25 bar, where $N = 1$, under this situation soliton fission does not happen and a DW is generated at 795 nm. For this parameters, $L_{NL}$ and $L_D$ has the same value, which it means that dispersive and nonlinear terms act at the same time, where one of them overcomes the other, according to the pulse shape, nonlinear effects exceed the dispersion. In the case of Krypton at 25 bar, Fig **5-19**(b), $L_{NL}$ turns out to be smaller than $L_D$ and with a low soliton number, $N = 2$, the pulse shape presents an expected behavior.
In other way, the temporal response presents shifting, where the pulse propagates slower or faster than the input, in Fig **5-19**(d) at 25 bar, there is a temporal compression, with almost none of energy lost.
In summary, the spectrum and temporal output response can be tunned according to pressure, where the dispersion profile presented multiple ZDW, which can be used to lunch an optical pulse at normal dispersion and if it travels some wavelengths reaches anomalous dispersion for the optical soliton formation. The HCPCF geometry considered presented several limitations, where one of the most important was the no pulse confinement at higher pressures for Xenon and Krypton. Xenon is one of the most promising gases due to high nonlinear refractive index at high pressures, which results in a high $\gamma$, how can be seen in table **5-3**, but this property could not be exploited. In this way, the HCPCF presented here is not recommended to be used for spectral broadening as supercontinuum generation, but it presented a novel and, according to my knowledge, unknown property to compress the intial pulse width with low energy lost and the control over the propagation speed, more studies in this filed are necessary to know the exact dependence with pressure.

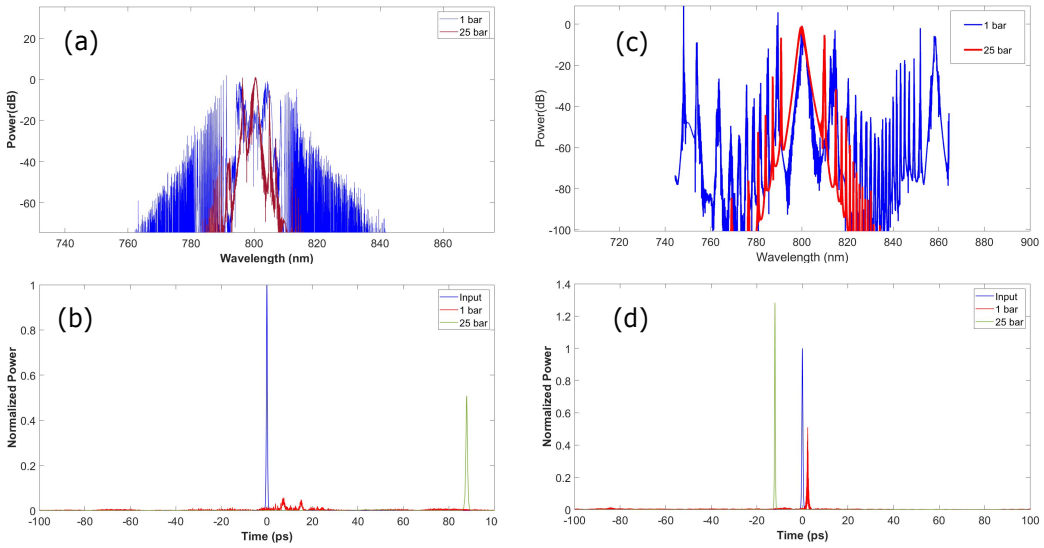


**Figure 5-19**.: output response for Xenon and Krypton filled HCPCF at 800 nm, 1/50 $P_{cr}$ and 500 fs pulse width for 1 and 25 bar after 1 m propagation distance. (a) Xenon output spectrum. (b) Xenon output temporal response. (c) Krypton output spectrum. (d) Krypton output temporal response

**Table 5-3**.: $\gamma$ value for Xenon and Krypton at different pressures

| $\gamma(W^{-1}m^{-1})$ | | |
|---|---|---|
| **Pressure (bar)** | **Xenon** | **Krypton** |
| 1 | $2,83 \cdot 10^{-04}$ | $1,03 \cdot 10^{-05}$ |
| 25 | $3,29 \cdot 10^{-04}$ | $4,43 \cdot 10^{-05}$ |

| **Xenon** | | | | | | | | | |
|---|---|---|---|---|---|---|---|---|---|
| **Pressure (bar)** | $\beta_2$ $ps^2/m$ | $\beta_3$ $ps^3/m$ | $\beta_4$ $ps^4/m$ | $\beta_5$ $ps^5/m$ | $\beta_6$ $ps^6/m$ | $\beta_7$ $ps^7/m$ | $\beta_8$ $ps^8/m$ | $\beta_9$ $ps^9/m$ | $\beta_{10}$ $ps^{10}/m$ |
| **1** | −3.168 | 0.834 | 0.676 | −0.147 | −0.040 | 0.005 | $4.887 \cdot 10^{-6}$ | $-2.654 \cdot 10^{-8}$ | $-9.751 \cdot 10^{-11}$ |
| **25** | −44.347 | 17.681 | 0.756 | −0.383 | −0.021 | 0.003 | $2.484 \cdot 10^{-4}$ | $5.185 \cdot 10^{-7}$ | $5.267 \cdot 10^{-10}$ |
| **Krypton** | | | | | | | | | |
| **1** | −12.082 | −0.745 | 0.023 | $7.768 \cdot 10^{-4}$ | $-2.788 \cdot 10^{-5}$ | $-7.511 \cdot 10^{-7}$ | $1.853 \cdot 10^{-8}$ | $5.208 \cdot 10^{-10}$ | $-1.182 \cdot 10^{-15}$ |
| **25** | −17.163 | −1.529 | 0.072 | 0.003 | $-1.599 \cdot 10^{-4}$ | $-5.969 \cdot 10^{-6}$ | $1.845 \cdot 10^{-7}$ | $7.789 \cdot 10^{-9}$ | $8.076 \cdot 10^{-14}$ |

**Table 5-4**.: Xenon and krypton dispersive terms at 1 bar and 25 bar in HCPCF

## 5.4. Negative Curvature Hollow Core Fiber Simulation

### Argon

The first parameter under study was the Argon dispersion profile, in Fig 5-20 are presented the different traces at 1 bar, 25 bar, 90 bar and 140 bar, where the ZDW is within the wavelength window under study for 25 bar and 90 bar. An interesting property was the possibility to shift the dispersion trace with pressure, where each wavelength is shifted towards lower values of $D$, making possible the control of normal and anomalous dispersion. Despite there is no a clear dependence of dispersion with pressure due each wavelength is moved a different quantity, it is possible a characterization of the fiber to know the ZDW in function of pressure. A complete different picture is displayed for NHCPCF in comparison with HCPCF where there are multiple ZDW. The optical pulse confinement was reached for every pressure considered. Anomalous dispersion was achieved at pressures of 1 bar and 25 bar.

Fig 5-21(a) presents the output spectrum for two different levels of energy and propagation distance. With 1/8 Pcr and $z = 1$ m the final pulse results in a spectrum broadening from 400 nm up to 1900 nm with a flat shape, where the energy is almost evenly distributed. Nevertheless, in Fig 5-21(b) its temporal shape is presented, where it can be see how the initial pulse suffers compression and presents a number of different peak, indicating the presence of soliton fission, where each one moves at distinct velocities. Besides, it was found a DW generated at 400 nm.

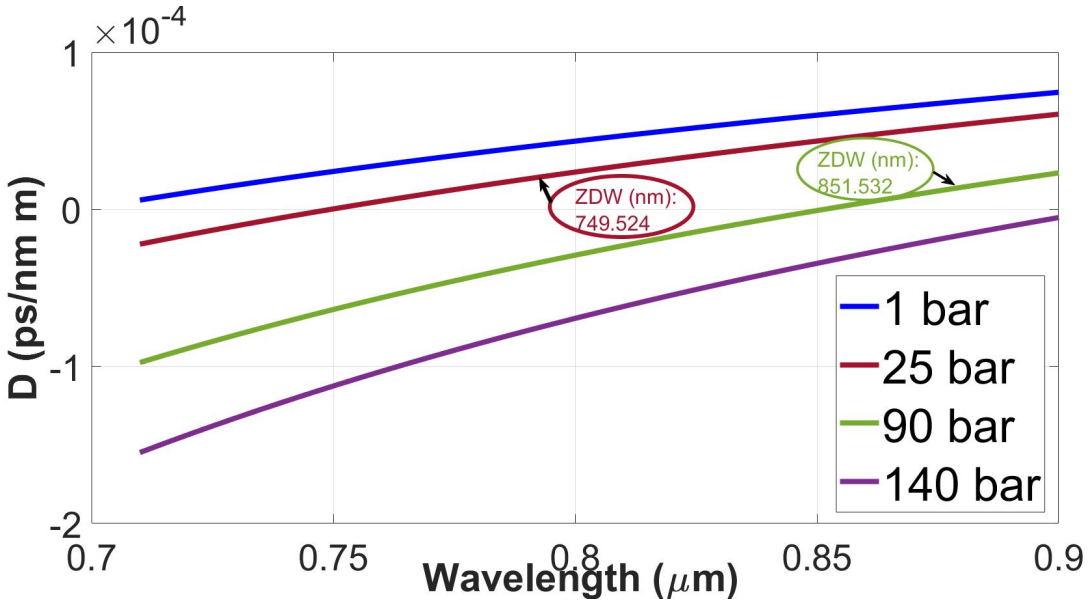


**Figure 5-20**.: Profile dispersion for Argon filled NHCPCF at different pressures.

Once the power stars to decrease: 1/50 Pcr, 1/100 pcr and 1/1000 Pcr the output pulse remains unaltered over 1 m of propagation distance. But even with the lowest power is possible to obtain a change in the output when the propagation distance is increased, in this case it was set to 100 m, a lower spectal broadening can be observed with the formation of a DW around 500 m (Fig **5-21**(a)), in the other hand its temporal output presents several differences with the case at 1 bar, where the pulse is divide in two, both get narrowed and one travels more fast that the input, whereas the other travels slower. The difference at change the power was in the soliton number, for the higher level of energy $N$ corresponds to 30 and for the lower one $N = 3$. The spectrum achieved with the change of the propagation distance was due to that the nonlinear terms could have more interaction and they were preponderant over the dispersion, thanks to $L_{NL} < L_D$.
In Fig **5-21**(c) and (d) are presented the spectral and temporal output at 25 bar, where for 1/8 Pcr and $z = 1$ m the spectral broadening and shape were very similar to 1 bar at the same conditions, despite the fact that at 25 bar $N$ was equal to 41. The principal difference with respect to Fig **5-21**(a) was about $L_{NL}$ and$L_D$, where for (a) the dispersive and nonlinear distance were close to each other, but in (c) only nonlinear terms interact, pointing out soliton fission and modulation instability like the principal reason behind the spectral broadening.

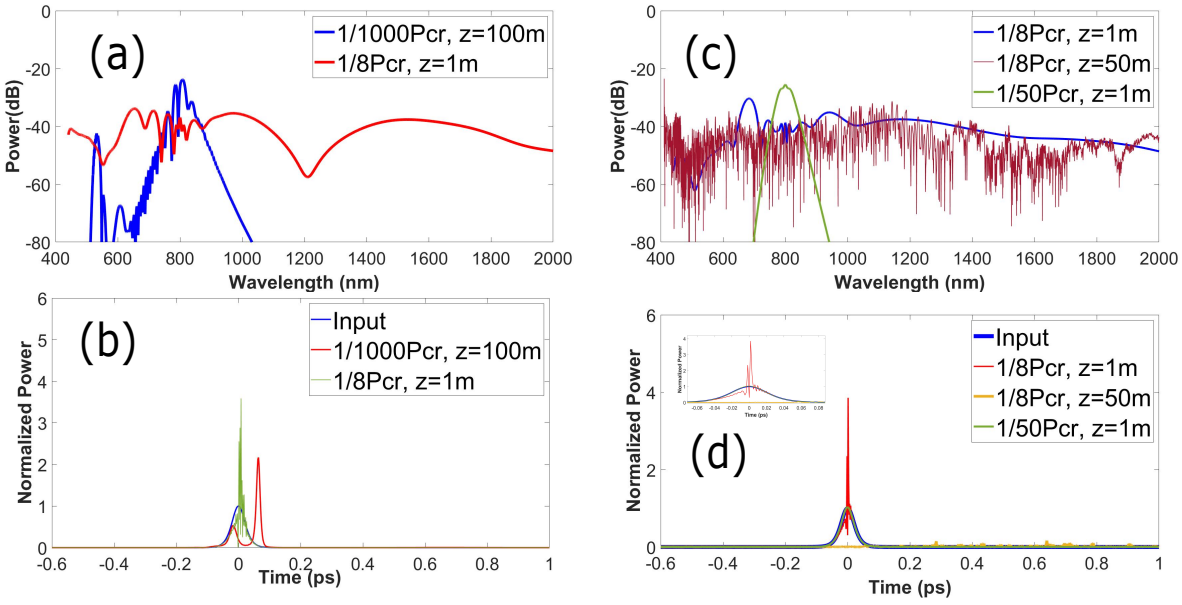


**Figure 5-21**.: temporal and spectral output response for Argon NHCPCF filled. (a) Spectrum output at 1 bar. (b)Temporal output at 1 bar. (c)Spectrum output at 25 bar. (d)Temporal output at 25 bar.

This assumption is confirmed by extending the propagation distance up to $z = 50$ m keeping the same power, making the dispersive terms have influence in the propagated pulse, it can be seen like the pulse extension is conserved, but the shape is degraded with the appearance of many peaks. The time response (**5-21**(d)) is consistent with the results and the influence of nonlinear and dispersive terms, where nonlinear terms have the action of pulse compression, whereas the dispersive terms break this shape into multiple sub-pulses traveling at different velocities. Once the nonlinear interaction is reduced by lowering the power, 1/50 Pcr, the pulse remains almost the same as the input for 1 m propagation distance.
In Fig **5-22** is found the simulation performed at 90 bar and 140 bar. Despite $\gamma$ increases with pressure, Fig **5-23**, the output spectrum at 90 bar and 1/8 Pcr propagated 1 m is shorter in comparison with the same parameters but at 1 bar or 25 bar, even though at 90 bar the soliton number is higher than at 1 bar. The reason of this behavior is attributed to $\beta_2$, where for higher pressures than 25 bar it reaches positive values, table **5-6**. Another remarkable characteristic is the similitude in the temporal and spectral output shape at 90 bar and 140 bar, a similar situation happens with 1 bar and 25 bar, this can be explained due to $L_{NL}$, where this pressures share similar values, table **5-6**. In this way, soliton fission is one of the most important effects to reach a wide spectral broadening, but it is not the only phenomenon contributing to this purpose, where others like modulation stability can broad the spectrum, another feature about the pulse response is the broad tendency towards higher wavelengths. An interesting characteristic due to the nonexistence of Raman effect. A disadvantage is the low power at the output, less than $-30$ dB, nonetheless the spectral broadening and temporal compression could be promising to be used in many applications.

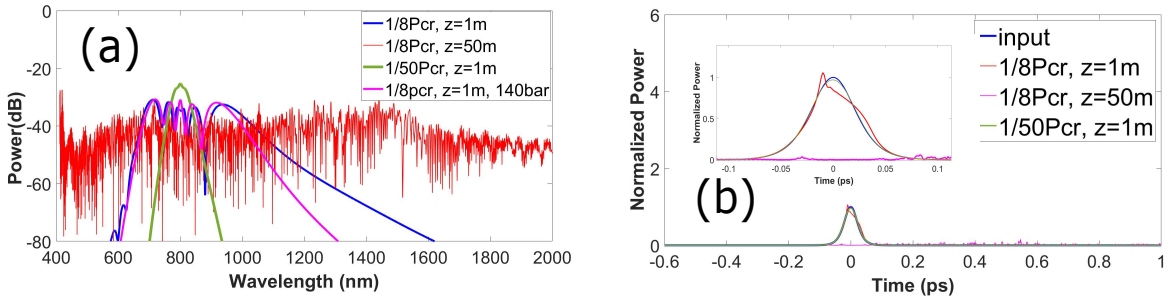


**Figure 5-22**.: output response for Argon NHCPCF filled at 90 bar and 140 bar. (a)Spectrum output. (b)Temporal output

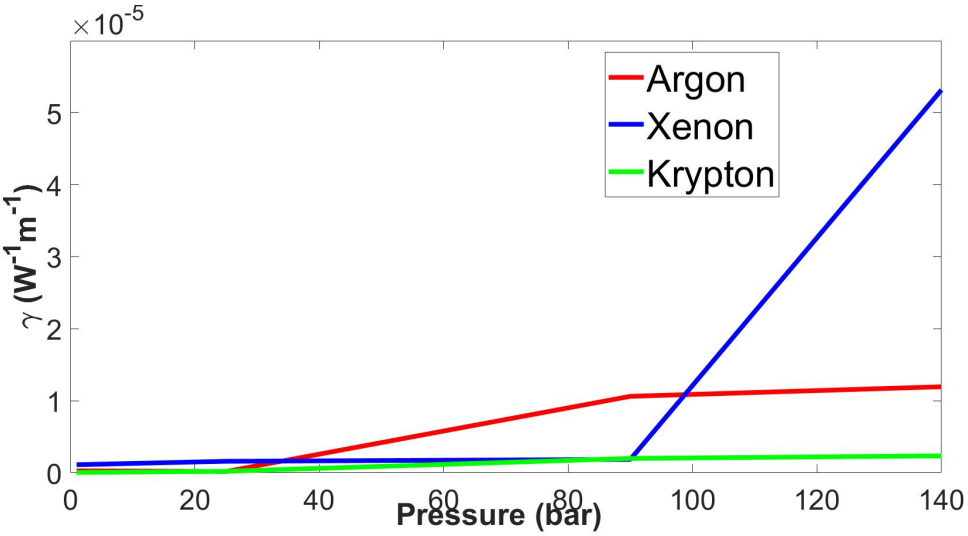


**Figure 5-23**.: $\gamma$ in function of pressure for: Argon, Xenon and Krypton

**Table 5-5**.: $L_D$ and $L_{NL}$ for Argon at different pressures, for 1/8 Pcr at 50 fs

| **Argon** | | |
|---|---|---|
| **Pressure (bar)** | $L_D(m)$ | $L_{NL}(m)$ |
| 1 | $54,612$ | $0,0592$ |
| 25 | 100 | $0,0596$ |
| 90 | $81,148$ | 0.061 |
| 140 | $34,135$ | 0.061 |

| Argon | | | | | | | | | |
|---|---|---|---|---|---|---|---|---|---|
| **Pressure (bar)** | $\beta_2$ $ps^2/m$ | $\beta_3$ $ps^3/m$ | $\beta_4$ $ps^4/m$ | $\beta_5$ $ps^5/m$ | $\beta_6$ $ps^6/m$ | $\beta_7$ $ps^7/m$ | $\beta_8$ $ps^8/m$ | $\beta_9$ $ps^9/m$ | $\beta_{10}$ $ps^{10}/m$ |
| **1** | $-1.473$ $10^{-5}$ | 5.341 $10^{-8}$ | $-7.718$ $10^{-11}$ | 1.768 $10^{-13}$ | $-5.022$ $10^{-16}$ | 1.848 $10^{-18}$ | $-9.546$ $10^{-21}$ | 4.956 $10^{-23}$ | $-5.696$ $10^{-29}$ |
| **25** | $-8.042$ $10^{-6}$ | 5.612 $10^{-8}$ | $-7.703$ $10^{-11}$ | 1.767 $10^{-13}$ | $-5.027$ $10^{-16}$ | 1.847 $10^{-18}$ | $-9.662$ $10^{-21}$ | 5.407 $10^{-23}$ | 5.338 $10^{-28}$ |
| **90** | 9.915 $10^{-6}$ | 6.341 $10^{-8}$ | $-7.665$ $10^{-11}$ | 1.762 $10^{-13}$ | $-5.039$ $10^{-16}$ | 1.875 $10^{-18}$ | $-1.000$ $10^{-20}$ | 5.571 $10^{-23}$ | $-8.566$ $10^{-28}$ |
| **140** | 2.357 $10^{-5}$ | 6.896 $10^{-8}$ | $-7.637$ $10^{-11}$ | 1.759 $10^{-13}$ | $-5.055$ $10^{-16}$ | 1.895 $10^{-18}$ | $-1.015$ $10^{-20}$ | 5.809 $10^{-23}$ | $-1.404$ $10^{-27}$ |

**Table 5-6**.: Dispersive terms for Argon at 1 bar,25 bar, 90 bar, 140 bar

### Xenon

Fig **5-24** presents the dispersion parameter in function of pressure, it is worth noting that at 1 bar all the wavelengths considered present $\beta_2 < 0$, once the pressure starts to increase the dispersion profile undergoes a down shift, where at pressures higher than 40 bar, $\beta_2 > 0$. This means that at lower pressures it is possible obtain anomalous dispersion for a wide spectral windows, with increasing pressure more wavelengths go into normal dispersion, making it necessary to increase the wavelength to reach optical soliton.

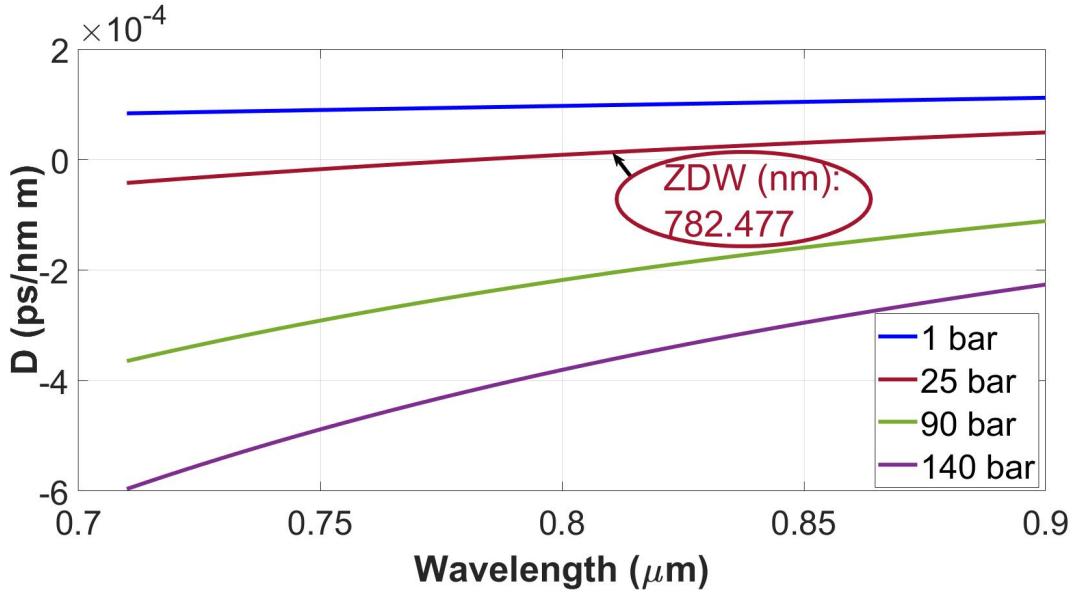


**Figure 5-24**.: Profile dispersion for Xenon filled NHCPCF at different pressures.

The spectrum output behavior with the change of pressure, peak power, propagation distance and pulse width are presented in Fig **5-25**, where the most remarkable results are shown. Starting at 1 bar the most broadest spectrum is reached at 1/8 Pcr which corresponds to the higher energy considered, with 1 m propagation distance. This is expected due to the higher soliton number, $N = 20$, and the short nonlinear distance, $L_{NL} = 0.059$ m. So, the pulse has broadening nearly to 800 nm, but with low power. As the peak power is decreased the spectral broadening too, but it is possible to extend this widening if the propagation distance is increased Fig **5-25**(a), but at cost of the pulse detriment. A very similar behavior is found at 25 bar, Fig **5-25**(b): same spectral broadening. the reason for this is due to $L_D$, $L_{NL}$ does not change so much (table **5-7**), despite the fact that at 25 bar $N$ increases to 68. When the linear gas region is exceeds, the output spectrum starts to change, as can be seen at 90 bar and 140 bar, **5-25**(c) and (d). At 25 bar the spectrum broadening is much lower than at 1 bar with the same peak power, it is necessary to increase the propagation distance to increase the broadening, reaching more than 1600 nm, where a possible DW is generated at 490 nm, nevertheless this DW wavelength does not match with the theory, Eq 3-39. In this way, the pressure increment give place to a higher $\gamma$, enabling more spectral broadening, but making necessary a longer propagation distance, which causes the appearance of multiple peaks.

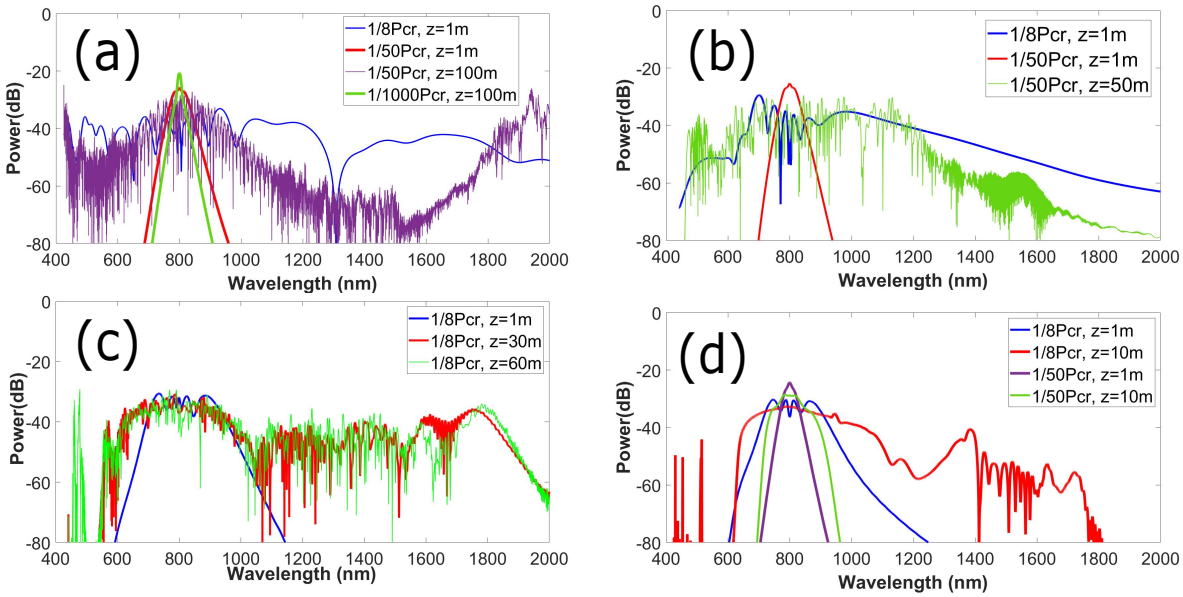


**Figure 5-25**.: Spectrum output for Xenon filled NHCPCF at (a)1 bar, (b) 25 bar, (c) 90 bar and (d) 140 bar, with different peak power and propagation distance at 50 fs pulse width.

A relative flat and broad spectrum is achieved with lower pressure, where although gamma is lower, the soliton number is higher, this is thanks to $Pcr$, where its value is higher enabling

the use of most powerful laser without enter in ionization region. This is not a advantage or disadvantage because the ionization term has been proved to contribute with numerous new phenomena [10] [19] [75], so the situation and use must been considered. The power necessary to reach a similar spectral broadening at 1 bar with 140 bar is two orders of magnitude lower.

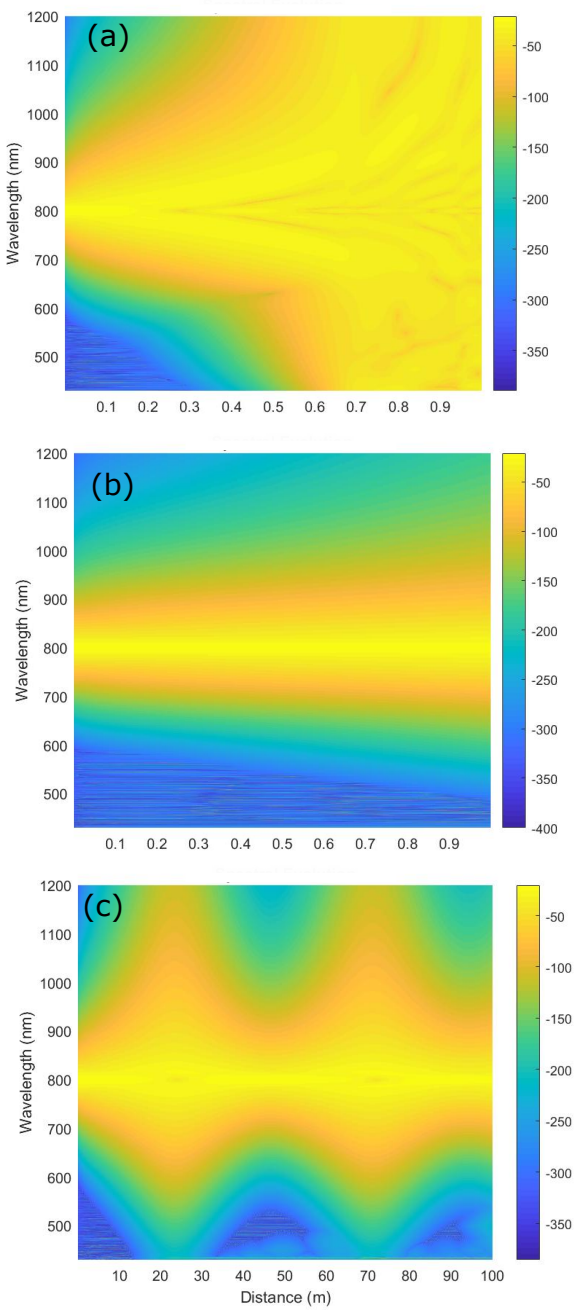


**Figure 5-26**.: Spectrum evolution in Xenon filled NHCPCF at 1 bar and 50 fs. (a) $z = 1$ m, 1/8 Pcr. (b) $z = 1$ m, 1/50 Pcr. (c) $z = 100$ m, 1/50 Pcr

Fig 5-26 presents how the spectrum pulse evolves as it propagates, in (a) and (b) can be appreciated the velocity at which the spectral broads, in (c) the conditions are the same than in (b), but the propagation distance was increasing. Here a periodic evolution of the spectrum broadening is presented, where the more probably reason is the balance between nonlinear and dispersion terms. Indicating the possibility of the spectral broadening control with propagation distance.

Observing the temporal output at each pressure, Fig 5-27, it can be noted that at the higher peak power the pulse is compressed when the pressure is set to 1 bar, as the pressure is increased the compression starts to disappears and this behavior is no longer present for any combination of power, pulse width or propagation distance ,Fig 5-27 (c) and (d). The reason for this can be found in table 5-7 and table 5-8, where $L_D$ is more shorter at higher pressures, making that the dispersive terms have more impact over the pulse, with the addition that at this pressures no soliton formation is achieved.

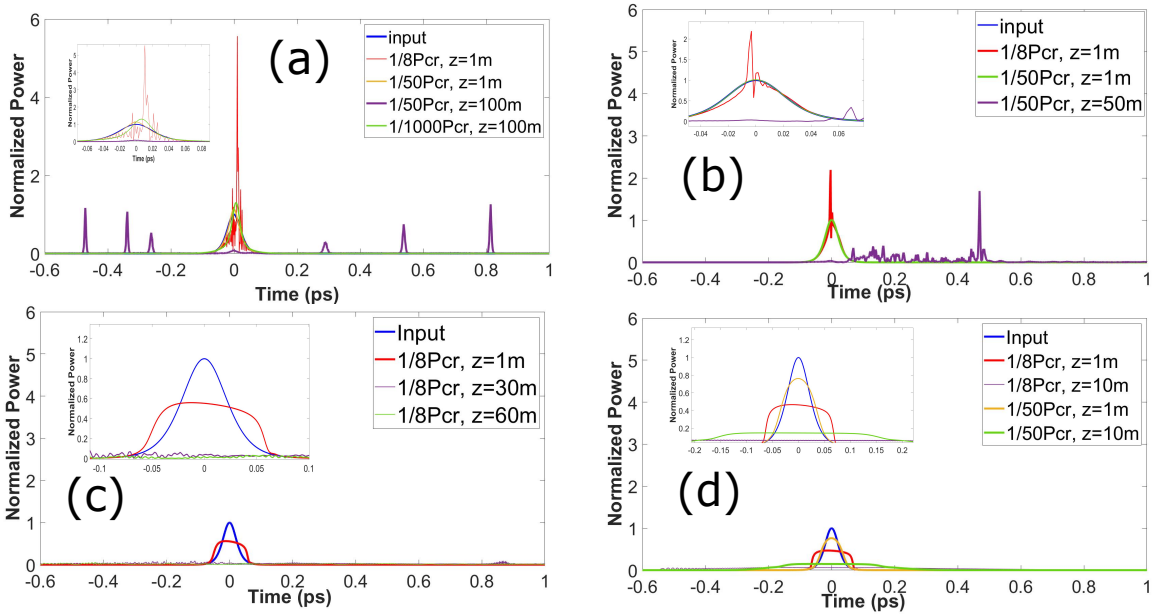


**Figure 5-27**.: Temporal output for Xenon filled NHCPCF at (a)1 bar, (b) 25 bar, (c) 90 bar and (d) 140 bar, with different peak power and propagation distance at 50 fs pulse width.

**Table 5-7**.: $L_D$ and $L_{NL}$ for Xenon at different pressures, for 1/8 Pcr at 50 fs pulse width

| **Xenon** | | |
|---|---|---|
| **Pressure (bar)** | $L_D(m)$ | $L_{NL}(m)$ |
| 1 | 24.4050 | 0.0592 |
| 25 | 27.7047 | 0.0601 |
| 90 | 10.8700 | 0.0626 |
| 145 | 6.2250 | 0.0644 |

**Table 5-8**.: Xenon filled NHCPCF dispersion parameters at 1 bar, 25 bar, 90 bar and 140 bar

| **Xenon** | | | | | | | | | |
|---|---|---|---|---|---|---|---|---|---|
| **Pressure (bar)** | $\beta_2$ $ps^2/m$ | $\beta_3$ $ps^3/m$ | $\beta_4$ $ps^4/m$ | $\beta_5$ $ps^5/m$ | $\beta_6$ $ps^6/m$ | $\beta_7$ $ps^7/m$ | $\beta_8$ $ps^8/m$ | $\beta_9$ $ps^9/m$ | $\beta_{10}$ $ps^{10}/m$ |
| **1** | $-3.297$ $10^{-5}$ | 4.496 $10^{-8}$ | $-7.807$ $10^{-11}$ | 1.763 $10^{-13}$ | $-5.025$ $10^{-16}$ | 1.850 $10^{-18}$ | $-9.556$ $10^{-21}$ | 5.050 $10^{-23}$ | $'-4.257$ $10^{-28}$ |
| **25** | $-2.904$ $10^{-6}$ | 5.696 $10^{-8}$ | $-7.710$ $10^{-11}$ | 1.754 $10^{-13}$ | $-5.060$ $10^{-16}$ | 1.909 $10^{-18}$ | $-1.039$ $10^{-20}$ | 5.812 $10^{-23}$ | 2.736 $10^{-28}$ |
| **90** | 7.402 $10^{-5}$ | 8.778 $10^{-8}$ | $-7.502$ $10^{-11}$ | 1.752 $10^{-13}$ | $-5.300$ $10^{-16}$ | 2.198 $10^{-18}$ | $-1.426$ $10^{-20}$ | 9.479 $10^{-23}$ | 5.795 $10^{-30}$ |
| **140** | 1.292 $10^{-4}$ | 1.101 $10^{-7}$ | $-7.406$ $10^{-11}$ | 1.784 $10^{-13}$ | $-5.718$ $10^{-16}$ | 2.646 $10^{-18}$ | $-2.075$ $10^{-20}$ | 1.604 $10^{-22}$ | $-8.375$ $10^{-29}$ |

### Krypton

The dispersion profile for Krypton in function of pressure can be found in Fig **5-28**, where at 800 nm $\beta_2$ was always greater than zero, making the soliton formation no possible. Likewise, dispersion shift goes towards lower values with the increase of pressure. An interesting fact was the high $\beta_2$ value for 90 bar and 140 bar, table **5-10**.
At the lower pressure, which correspond to the highest nonlinear parameter value, was reached the wider spectral broadening, where a similar behavior with respect to before gases: Argon and Xenon was found, for 1/8 Pcr and $z = 1$ m there is output spectrum relatively flat, but once the propagation distance is increased there are a lot of peaks due to the dispersive parameters action, Fig **5-29**(a). in the time domain can be seen how propagation makes the pulse travels at different speeds, and only at 1 bar and 1/8 Pcr,$z = 1$ m the pulse undergoes temporal compression due to $L_{NL}$ overcomes dispersion.
Once the pressure starts to be increased, the spectral broadening is lower and dispersion effects are less significant is its shape, this behavior is due to the balance between $L_{NL}$ and $L_D$ reached, as can be seen in table **5-9** and the absence of soliton formation. So, as the kerr effect acts the dispersion effects act in the opposite manner, making little spectrum broadening as can be corroborated in Fig **5-29** (b) and (c). The high $\beta_2$ value implies a wider temporal output, where temporal compression is no longer present Fig **5-30**. At 140 bar the temporal and spectral response was nearly the same as at 90 bar, where no significant effects could be appreciated.

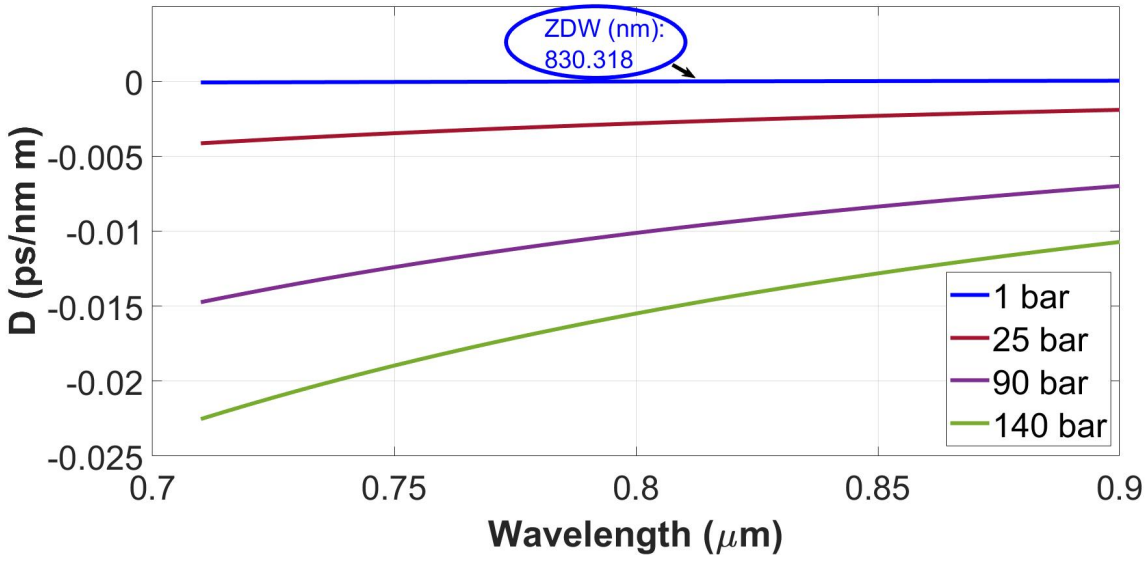


**Figure 5-28**.: Profile dispersion for Krypton filled NHCPCF at different pressures.

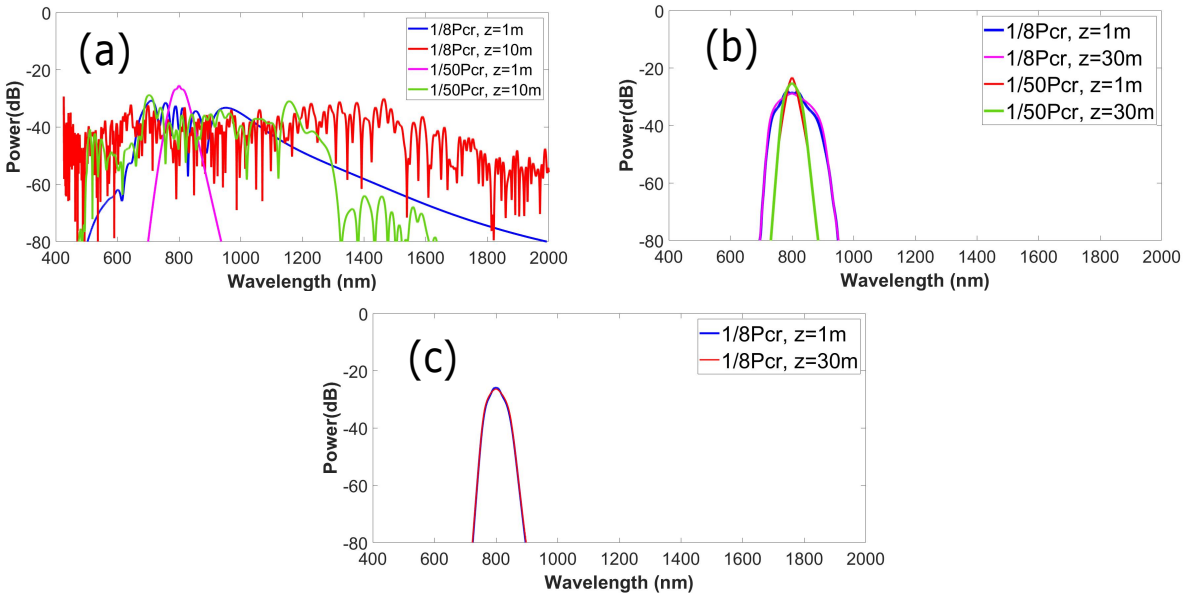


**Figure 5-29**.: Spectrum output for Krypton filled NHCPCF at (a)1 bar, (b) 25 bar, (c) 90 bar, with different peak power and propagation distance at 50 fs pulse width.

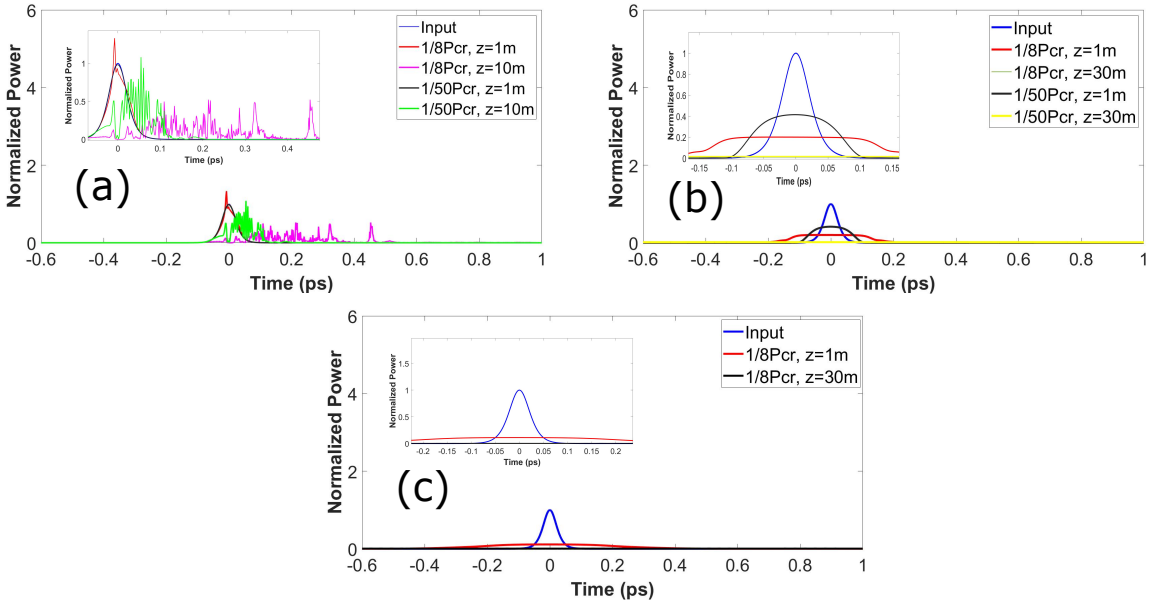


**Figure 5-30**.: Temporal output for Krypton filled NHCPCF at (a)1 bar, (b) 25 bar, (c) 90 bar , with different peak power and propagation distance at 50 fs pulse width.

**Table 5-9**.: $L_D$ and $L_{NL}$ for Krypton at different pressures, for 1/8 Pcr at 50 fs pulse width

| **Krypton** | | |
|---|---|---|
| **Pressure (bar)** | $L_D(m)$ | $L_{NL}(m)$ |
| 1 | 1.4025 | 0.0592 |
| 25 | 0.8422 | 0.0597 |
| 90 | 0.2341 | 0.0613 |
| 145 | 0.1529 | 0.0673 |

| **Krypton** | | | | | | | | | |
|---|---|---|---|---|---|---|---|---|---|
| **Pressure (bar)** | $\beta_2$ $ps^2/m$ | $\beta_3$ $ps^3/m$ | $\beta_4$ $ps^4/m$ | $\beta_5$ $ps^5/m$ | $\beta_6$ $ps^6/m$ | $\beta_7$ $ps^7/m$ | $\beta_8$ $ps^8/m$ | $\beta_9$ $ps^9/m$ | $\beta_{10}$ $ps^{10}/m$ |
| **1** | 5.736 $10^{-6}$ | 6.319 $10^{-8}$ | $-7.569$ $10^{-11}$ | 1.776 $10^{-13}$ | $-5.019$ $10^{-16}$ | 1.834 $10^{-18}$ | $-9.619$ $10^{-21}$ | 5.619 $10^{-23}$ | $-6.133$ $10^{-28}$ |
| **25** | 9.552 $10^{-4}$ | 5.082 $10^{-7}$ | $-1.854$ $10^{-11}$ | 2.063 $10^{-13}$ | $-4.968$ $10^{-16}$ | 1.887 $10^{-18}$ | $-1.002$ $10^{-20}$ | 5.467 $10^{-23}$ | $-1.181$ $10^{-27}$ |
| **90** | 0.003 | 1.669 $10^{-6}$ | 1.288 $10^{-10}$ | 2.808 $10^{-13}$ | $-4.886$ $10^{-16}$ | 2.032 $10^{-18}$ | $-1.176$ $10^{-20}$ | 7.062 $10^{-23}$ | $-1.454$ $10^{-28}$ |
| **140** | 0.005 | 2.523 $10^{-6}$ | 2.354 $10^{-10}$ | 3.356 $10^{-13}$ | $-4.888$ $10^{-16}$ | 2.197 $10^{-18}$ | $-1.405$ $10^{-20}$ | 9.293 $10^{-23}$ | $-3.957$ $10^{-28}$ |

**Table 5-10**.: Krypton filled NHCPCF dispersion parameters at 1 bar, 25 bar, 90 bar and 140 bar

### 5.4.1. Conclusions

Using the GNLSE code were numerically simulated different substances under different geometrical parameters and input conditions. The first geometrical fiber studied was the Hollow core photonic crystal fiber filled with $CS_2$ known as liquid core crystal fiber. Where it was presented the temporal and spectral behavior for a hollow-core photonic crystal fiber infiltrated with carbon disulfide with its correct response function, where it was studied this new behavior and dynamics under different circumstances. It was also presented how the peak power influences the spectral broadening which is closely related to the number of solitons, identifying soliton fission as main mechanism in this new response function. The propagation

distance is another variable under consideration, where it was established that in the distance under consideration with one soliton the spectral broadening was negligibly, but with two solitons the spectral broadening increase with more propagation distance. Concluding so the main mechanism, taking into account the new response function, was soliton fission, where the non-instantaneous response acts increasing the effective non-linear refractive index and the non-linear parameter. In other way, by studying the influence of $\gamma$ as a constant and $\gamma$ as a variable in the time and frequency domains outputs when different parameters are tweaked such as: pulse width, input power, third-order dispersion, higher-order nonlinear terms and propagation distance it was possible to observe the effect of considering $\gamma$ as a variable on the pulse and how its inclusion allowed to reach more accurate results.
For instance, when the pulse width widens, the DW responses are similar, whereas for a narrower pulse width, the DW power becomes stronger at a lower $\delta_3$. Another interesting result was the appearance of a DW at an early propagation distance when $\gamma$ was considered a constant, which does not occur when $\gamma$ is Z-dependent, but modulation instabilities start showing up under this condition what represents a great difference between constant and variable nonlinear parameters. Through the study of number of solitons and pulse width a balance can be observed, when this balance is reached the $\gamma$ variation with position has low impact on the final results, but when this balance is broken the output is very different from when $\gamma$ is set constant. Similarly, it can be seen that not all parameters (DW wavelength and DW power) are affected equally, DW power turned out to be especially more sensitive to the variation of $\delta$ and the consideration of $\gamma$ as either a constant or z-function, whereas DW wavelength is especially less sensitive to the dependence on propagation of the pulse. Another fact worth pointing out is the need of a new DW power expression that can better fit with the simulation results and in which the influence of propagation is taken into account. Because the output has a dependence on the observed balance, the influence of parameters like $\delta$, $N$ and pulse width in the final result either of DW generation or of FWM is difficult to determine. Nevertheless we can conclude that $\gamma$ must be necessarily considered as function of the position.

In general, $\gamma$ must be considered a variable despite the fact that, under certain circumstances, the results are similar to when $\gamma$ is considered a constant, which may explain why the experimental and simulation results showed some discrepancies in some previous studies, such as in [68].

Finally, the HCPCF and NHCPCF geometries presents different characteristics when they are filled with the same gases: Argon, Xenon and Krypton. In HCPCF the shifted dispersion with pressure gave a trace that always have ZDW in the window frequency considered. One of the most notorious difference between HCPCF and NHCPCF, were the temporal and spectral output change with pulse width, where in HCPCF this change has significance in the temporal and spectral response, but in NHCPCF does not represent a significant

change, The main reason is due to the dispersion profile: multiple ZDW. It was found that HCPCF is good for temporal compression, whereas in NHCPCF the major characteristic was spectral broadening towards longer wavelengths. The most promising gas (Xenon), could not be exploited due to the $\beta_2$ behavior, where the anomalous dispersion goes to longer wavelengths at high pressures, and it is in this region where Xenon reaches its higher values on $n_2$, comparable with fused silica. In this way, it is conclude that for NHCPCF it is necessary the use of laser beyond 1000 nm as input wavelength in order to reach wide spectral broadening at low peak powers.

# 6. Conclusions

The scope of this work covered an experimental, a theoretical and a numerical approach to the modeling of nonlinear pulse propagation in optical fibers and characterization of nonlinear optical material parameters.
For the experimental approach, the Z-scan was implemented. This technique implementation was a new step for the optics laboratory in which this work was developed and now our campus has joined a group of only few others worldwide that use the technique. It is a powerful, fast and reliable tool for material nonlinear parameter characterization. Many substances were characterized in the scope of this work, both nonlinear refractive index and nonlinear absorption coefficient were reported and presented in different international congresses. The Z-scan system implemented paves the way for future works in nonlinear optics for the laboratory and the university, where future students and faculty can make use of it, helping position the laboratory as a reference in nonlinear characterization.
The numerical and theoretical approach were cover more significantly in chapter 3, where different simulations were performed with the new results found in the literature, to make a more precise description of the nonlinear pulse propagation inside fiber optics. New geometries and material response functions were considered. Moreover, an exhaustive analysis was executed in different regimes: pulse width, input power, nonlinear parameters involved. The exploration of such geometries and materials is crucial for the development of new tools for sensing and applications in many fields, as it was demonstrated along this thesis. The contributions made to the field of nonlinear optics were reflected in different works: international congresses and papers. Among the most significant results were the study of the new $CS_2$ response function and the proposal about the nonlinear response dependence with distance in non-instantaneous materials, which gives rise to new behaviors and unexpected results, besides the control of dispersive wave generation and four wave mixing by changing the propagation length. The exploration of new geometries such as negative hollow core photonic crystal fibers filled with noble gases and tuning its properties by pressure have demonstrated be a promissory way to generate a broad band flat spectrum.

# A. Nonlinear optical fiber infiltration implementation

This section is dedicated to the develop of the technique to obtain a successful infiltration of liquids into fiber. The objective is to implement a system in which hollow core photonic crystal fiber (HCPCF) is infiltrated in its core and the remaining holes remain the same. For this purpose a system as is shown in Fig**A-1** was created. From left to right, the light encounters with a 20X objective which focus the light into a single mode fiber which has been cut diagonally in the other border and spliced with a capillary. The HCPCF is spliced between two capillaries, the right border of the HCPCF is spliced to other capillary which is joined to a single mode, (diagonally cut as the previous one) and finally the light comes out towards a detector. The purpose of the gap between the single mode fiber and the capillary is opening a way of entrance for the liquid. The capillary is used to guide the liquid into the core hole of the HCPCF and the cladding holes remain untouched, this is possible because the capillary size and the HCPCF core are selected in such a way that their dimensions matched. The single mode fiber enables the coupling between light and capillary, where it follows its way into the HCPCF core where the nonlinear interaction occurs. The reason for two angled single mode fibers is because in this way a more homogeneous filled is guaranteed and avoid other problems such as materials with high volatility.

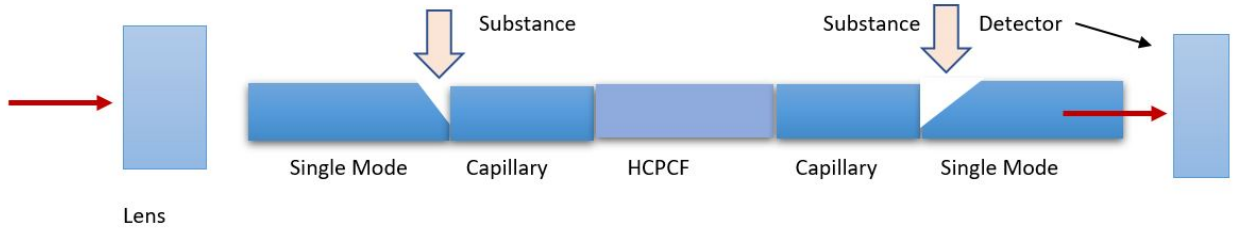


**Figure A-1**.: Light coming from left to right (red arrow), in its path it encounters a lens: 20X Olympus Plan Fluorite objective. Single mode. Capillary with 10$\mu$m inner diameter . Hollow core photonic crystal fiber (HCPCF). capillary. single mode and detector.

At first it was thought the possibility of a more elemental system in which only the HCPCF was necessary. This implementation required the collapsing of the cladding holes, while the central core hole remains open [82]. To do this, it was necessary to apply an electric arc with the right parameters, after many different attempts and approaches [83] this option was discarded because its complexity and difficult parameters control. The best approach to solve the problem about fiber infiltration was found as is proposed in Fig **A-1**, where a similar set up was implemented in [84]. To achieve the single mode fiber cutting at a certain angle, it was considered and explored the acid burning in which the fiber is placed in a pool of acid and after a time of exposure the fiber is reduced by the action of the acid. Several difficulties were found with this approach, among them: no time repeatability: the time necessary to obtain certain angle varies, hard control of the desire angle and poor finished in the fiber. For this reason another option was used, where the fiber is cleaved with the angle of choice, due to the limitations in the laboratory equipment, a variable angle cleaved station was developed, where the angle can be varied between 0 and 90 degrees. For the fiber infiltration the optimal angle goes between 10 and 20 degrees (small angles), this is due that it is necessary enough surface that guarantees a stable spliced but at the same time enables the infiltration of the liquid. In Fig **A-2** can be seen how it is possible controlling the angle at which the fiber is cleaved and perform a satisfactory splicing.

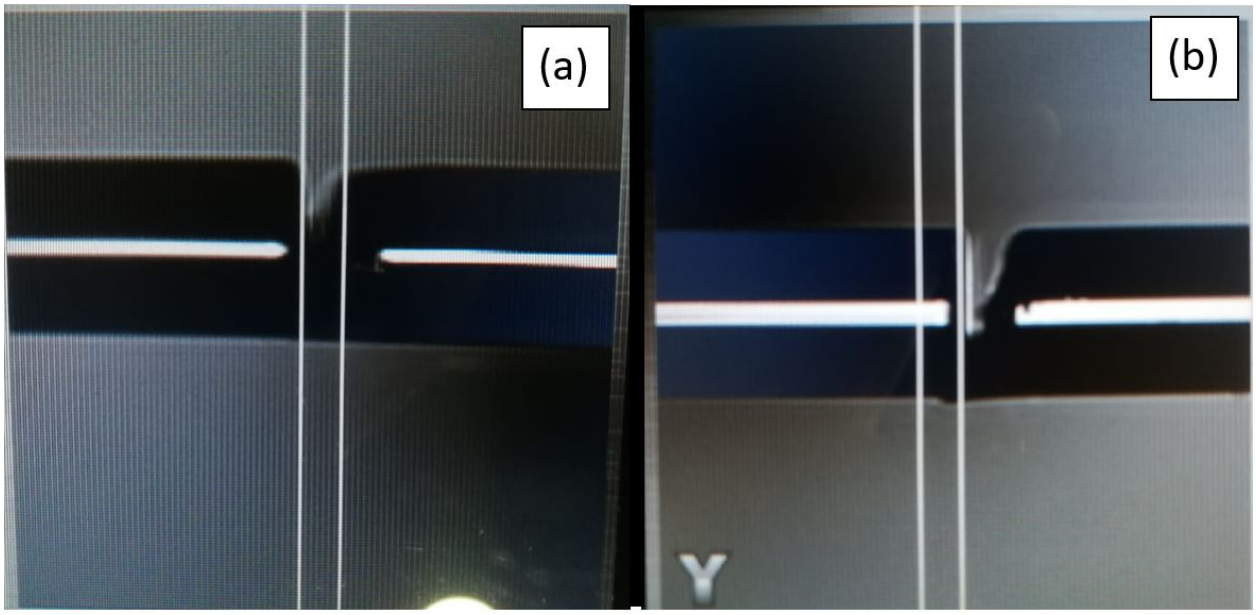


**Figure A-2**.: Fiber cleaved at two different angles: (a) and (b) and spliced successfully

Once the fiber is spliced, it is crucial be able to extract the fiber from the splicer machine without damage, due to its small area the fiber is very fragile and can be broken easily, to avoid this a piece was designed and made in a 3D printer which ensures the robustness of

the splicing.
Both the HCPCF and capillary infiltration was corroborated. In Fig **A-3** is shown the HCPCF before and after the liquid infiltration where it can be seen how the core is only filled and the cladding holes remain untouched.

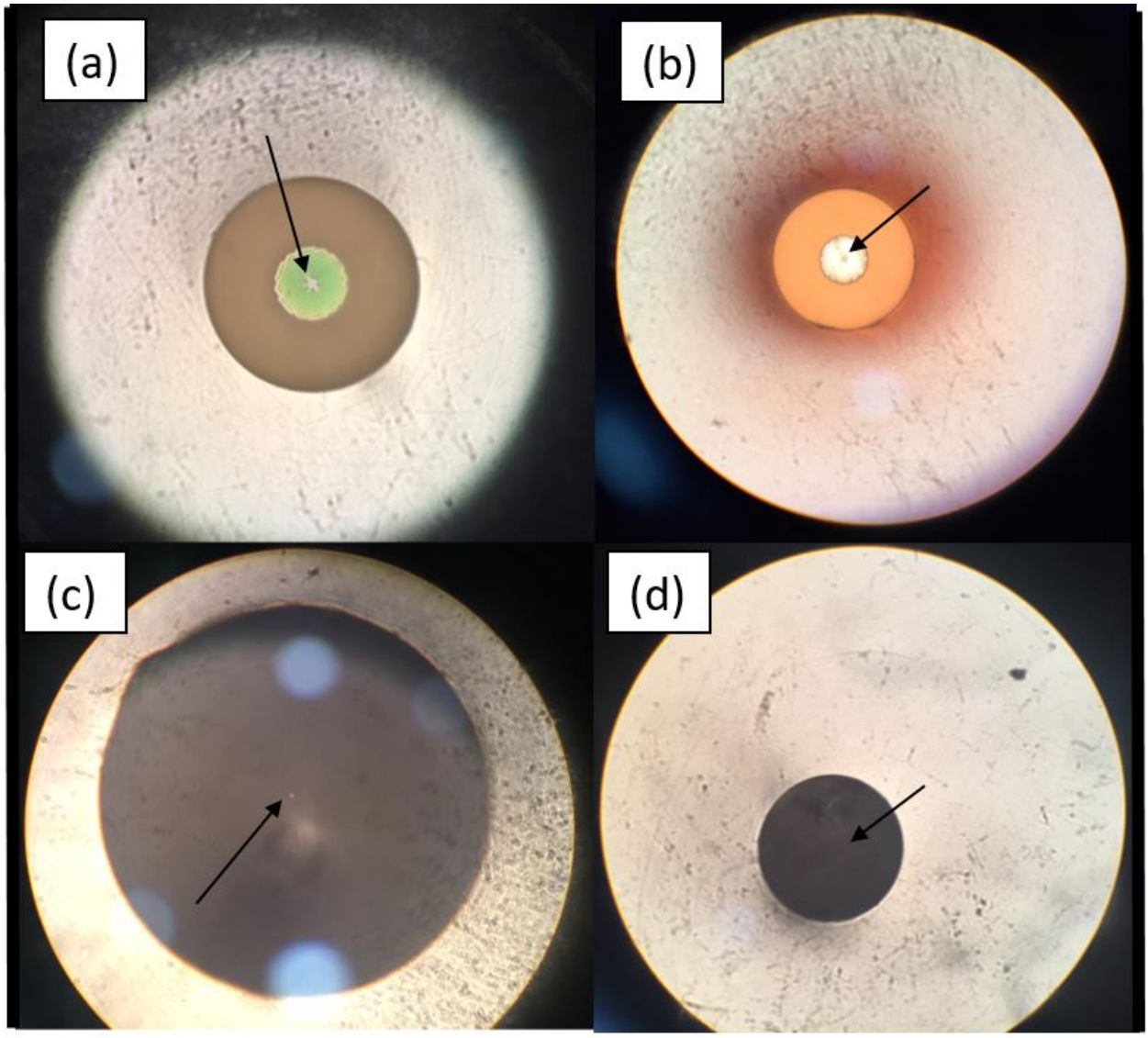


**Figure A-3**.: a and b: HCPCF before and after infiltration respectively. C and d capillary fiber before and after infiltration. Where the arrows indicate the core.

In this way, a successfully station of liquid infiltration into fiber was developed and implemented where the angle of splicing can be controlled. Enabling the versatility in its use with other fiber geometries and sizes, as well different liquids with distinct viscosities and characteristics.

# B. Numerical implementation of the nonlinear envelope equation

This chapter is dedicated to the explanation and implementation of the nonlinear envelope equation code presented before. For this purpose a code written on Octave or MatLab is presented. The technique and methods used here are shown in more details in ref: [33] and [34].

## B.1. Diffraction

The first thing to do is the input data definition, in Fig **B-1** is presented the data definition for a Gaussian beam of $\lambda = 800nm$, in a medium with refractive index of 3. Propagation distance of $0.0001m$

```
%%%%%Program to solve diffraction%%%%%%%
%%%%%Made by Sebastian V.Palacio%%%%%%%%
clear all
clc
%%%Definition of initial data
w0=1*10^-4;%Beam width
lambda=1*10^-2;%Wavelength in m
c=3*10^8;%spedd of light m/s
n=1.3;%refractive index
k0=(2*n*pi)/lambda;%wave vector
z1=0.0001;%propagation distance Z=K*M in m
z=z1;
E0=1;%in W inital power
z_0=(k0*(w0^2))/2;%rayleight distance
Mp=4*10^4;%maximum steps in z
deltaz=z/(Mp+1);
w_z=w0*sqrt(1 + (z^2)/(z_0^2));%beam with
F=z*(1 + (z_0/z)^2);%focusing length
M=Mp;%30;%how many distance between diagnostics
K=0;%z/M;%output loop, outer diagnostic
```

**Figure B-1**.: Definition of initial data

After the initial parameters definition it is necessary the grids definition, where the radial axis and the propagation axis are discretized. It is defined the radial axis windows and the number of steps in this axis.

```
%%%Grids definition
N1=9*10^2;%Number of steps in radial axis, of this size will be the matrix deltaj
r= 0.005;%distance in radial axis in m
rmin=1*10^-16;
j=0:1:(N1+1);%defining j
N=size(j,2); %Number of steps in radial axis, of this size will be the matrix deltaj
deltar=(r-rmin)/(N1+1);%1*10^-5;%defining deltar

r_j=j*deltar;%radial grid
```

**Figure B-2**.: Grid definition

Once the grids are defined, the matrices $L_+$ and $L_-$ are created. in line 39 is created $\Delta j$, then from line 43 to 52 is created $L_+$. Lines 50 and 51 presented the option to make the code second order accurate, in which case these lines must be uncomment. The only difference between $L_+$ and $L_-$ is a minus sign, the implementation of $L_-$ is shown in Fig **B-4**. In these

two matrices are consigned the boundary conditions, for this case: $\frac{\partial E}{\partial r} = 0$ at $r = 0$ and $E = 0$ at $r_{max}$. In line 66 is calculated the product: $L_{-}^{-} \cdot L_{+}$, necessary to obtain the final pulse.

```
34 -  v_j= 1 + 1./(2.*(j(2:N-1))); %The size is given by j
35 -  v_jm=[0,v_j];%add a zero to obtain a square matrix and the boundary conditions
36 -  u_j= 1 - 1./(2.*j(2:N));
37 -  two=-2*ones(N,1);%creating the central diagonal of the tridiagonal matrix
38
39 -  deltaj= diag(two,0) + diag(u_j',-1) + diag(v_jm',1); %creating the matrix
40    %deltaz=1;%how resolution will have each propagation step
41 -  delta= deltaz/(4*k0*(deltar^2));
42
43 -  Lpluscentral= 1 + (i*(delta/2)).*diag(deltaj,0);% L+ necessary to solve the matrix, central diagonal
44 -  Lplusup=(i*(delta/2)).*diag(deltaj,1);%upper diagonal
45 -  Lplusdown=(i*(delta/2)).*diag(deltaj,-1);%down diagonal
46 -  Lplus= diag(Lpluscentral,0) + diag(Lplusup,1) + diag(Lplusdown,-1);
47
48    % Lplus=1 + ((i*(delta/2)).*deltaj);
49 -  Lplus(1,:)=0; %to meet boundary condition dE/dr=0 at r=0 E=0 at r_max
50    % Lplus(1,1)=1 - 4*i*delta;%second order accuracy
51    % Lplus(1,2)=4*i*delta;%second order accuracy
52 -  Lplus(N,:)=0; %to meet boundary condition E=0 at r_max dE/dr=0
53
```

**Figure B-3**.: $L_{+}$ implementation

```
53
54 -  Lminuscentral= 1 - (i*(delta/2)).*diag(deltaj,0);% L- necessaty to solve the matrix
55 -  Lminusup= -(i*(delta/2)).*diag(deltaj,1);
56 -  Lminusdown= -(i*(delta/2)).*diag(deltaj,-1);
57 -  Lminus= diag(Lminuscentral,0) + diag(Lminusup,1) + diag(Lminusdown,-1);
58
59
60 -  Lminus(1,:)=0;%to meet boundary condition E=0 at r_max dE/dr=0
61 -  Lminus(N,:)=0;%to meet boundary condition E=0 at r_max dE/dr=0
62 -  Lminus(1,1)=1 ;%+4*i*delta;%to meet boundary condition E=0 at r_max dE/dr=0
63 -  Lminus(1,2)=-1;%*4*i*delta;%to meet boundary condition E=0 at r_max dE/dr=0
64 -  Lminus(N,N)=1;%to meet boundary condition E=0 at r_max dE/dr=0
65
66 -  L=Lminus\Lplus; %L is equal to the inverse of L- times L+ (a better way to calculate the product)
67
```

**Figure B-4**.: $L_{-}$ implementation

Finally, it is necessary to define the discretized input field, line 70. In lines 71 and 72 the input field is plotted. The for loop, Lines 76 to 85 solve the equation. where the values of the outer loop and the inner loop must match with the propagation distance $z$. The inner loop is thinking to make low cost diagnostics, whereas the outer loop is for making more consuming diagnostics. The variable c1 and c are auxiliary variables for seen in which loop the code is. n is the discretized propagation.

```
69    %%%Definition of the initial field
70 -  E(j+1,1)=E0.*exp(-((r_j.^2)./(w0^2)));%.*exp( ((-1i*k0*(r_j.^2))/(2*f) ) );% initial field at z=0,
71 -  figure
72 -  plot(r_j,abs(E(:,1)).^2)
73    %%%Loop of propagation
74 -  c=0;
75 -  c1=0;
76 -  for k=0:K
77
78 -      c1=c1+1;
79 -      for m=1:M
80 -          n=k*M + m;
81 -          c=c+1;
82
83 -          E(j+1,n+1)=L*E(j+1,n);
84 -      end
85 -  end
86
87    %hold on
88 -  figure
89 -  hold on
90 -  plot(r j,abs(E(:,c)).^2,'o')
```

**Figure B-5**.: Input pulse and loop to solve the equation

### Diffraction and nonlinear terms

Considering now the equation presented in section 1.4.4., the code implementation requires the addition of new variables to the diffraction code as follows. The speed of light, the pulse chirp, nonlinear coefficient and nonlinear refractive index, absorption coefficient, multi-photon absorption, group velocity, pulse width and molar contribution are some of the new variables required to simulated nonlinear terms with a new discretized dimension: time, as can be seen in Fig **B-6**.
The next step is the grid definition, for $z$ and $r$ axis.
In Fig **B-8** are presented two different ways to discretized the radial axis, $r_j$, in line 50 and 51. In the following lines are the temporal and frequency discretization, where 2 different approach are considered. It is recommended read the section dedicated to this discretization or the references mentioned before for a good understanding. The nonlinear tables are presented in Fig **B-9**, where dispersive terms were considered only up to second order. In this case the pulse is moving in the laboratory framework, but a change of variable of the kind presented in [2] can be done in order to change it. For the creation of $L_+$ and $L_-$ there are two alternatives: to minimize simulation time, but at cost of memory the matrices can be precomputed or recomputed at each step, to minimize memory usage. The first approach was chosen and in Fig **B-10** are $\nu_j$ and $\mu_j$, and the initializing vectors to form $L_+$ and $L_-$. The creation of $L_+$ and $L_-$ were made inside a for loop where, they were created for each discretized frequency and the new operators were added, Fig **B-10**. After this a definition of the initial field is necessary, where now it is discretized in the radial and time coordinate. Finally the solution of the GNLSE is presented in Fig **B-12**, where in the lines from 170 to 172 is account the dispersion parameters, in 173 the Raman contribution. Through the lines 178 to 192 some useful vectors are initialized and at the line 195 starts the nonlinear and propagation solution. To solve the differential equations the Runge Kutta fourth order was used, lines 205 to 216, after that the kerr term is introduced and in the next lines the Fourier transform of the before tables and the incident field are taken to solve the problem in frequency domain. Once the respective matrices are created, ref [34], the inverse Fourier transform is taken to obtain the final solution at that propagation step, and the loop is repeated until $z$ reaches its final value.

```
w0=100*10^-6;%Beam width
lambda=800*10^-9;%Wavelength in m
l0=800*10^-9;%Wavelength in m
clight=3*10^8;%speed of light m/s
c=3*10^8;%speed of light m/s
Chirp=-1;
n0=1.328;%refractive index
n2=1.6*10^-20;%nonlinear refractive index m^2/W
gama=5*10^3;%nonlinear coefficient (Wm)^-1
betasorp=0;%nonlinear absorption coefficient
frequency=clight/lambda; %1/s
omega0=2*pi*frequency;%rad/s
kappa=1;% multiphoton asoprtion order
k0=(2*n0*pi)/lambda;%wave vector
Pcr=(3.77*pi*n0)/(2*(k0^2)*n2);%W
vg=0;%-7*10^3;%30*10^2; %group velocity, vg=beta1
beta2=241*10^-27;
T_FWHM=50*10^-15;% in s
T0=T_FWHM/(2*log(1+sqrt(2)));% for gaussian pulse, pulse width
fR=0;% molar contribution to kerr effect

```

**Figure B-6**.: Initial variables to perform simulation in diffraction and nonlinear code

```
%%%Distance and grid distance
z=1.5*10^-2;%propagation distance Z=K*M in m
E0=(10*Pcr);%in W inital power
z_0=(k0*(w0^2))/2;%rayleight distance
Mp=1*10^3;%maximum steps in z
deltaz=z/(Mp+1);
w_z=w0*sqrt(1 + (z^2)/(z_0^2));%beam with
F=z*(1 + (z_0/z)^2);%focusing length
M=Mp;%30;%how many distance between diagnostics
K=0;%z/M;%output loop, outer diagnostic

%%%Grids definition
N1=2^8;%Number of steps in radial axis, of this size will be the matrix deltaj
r= (0.00025)*2;%distance in radial axis in m
rmin=1*10^-16;
j=0:1:(N1+1);%defining j
N=size(j,2); %Number of steps in radial axis, of this size will be the matrix deltaj
deltar=(r-rmin)/(N1+1);%1*10^-5;%defining deltar

```

**Figure B-7**.: Diffraction and nonlinear terms grid definition

```
% r_j=j*deltar;%radial grid
r_j = [-r + (((N1/2):(N1))*deltar), (0:(N1/2))*deltar];%linspace(-r, r, N1+2);
%%%%%%%%Frequency and time grids, l is for both
method=1;
%%%method 1
if method==1
nt=N;%number of points in the temporal grid
t_mult=4;
t_range = 200*10^-15;%.5*t_mult*T_FWHM;
tau = linspace(-t_range, t_range, nt+1); % temporal grid
tau = tau(1:end-1); %%% tau = T relative time,
dt = tau(2)-tau(1);
fs = 1/dt;% Sampling frequency
domega = 2*pi/nt*fs;
omega = [-2*pi*fs + (((nt/2):(nt-1))*domega), (0:(nt/2-1))*domega];% frequency grid
f = omega/2/pi;
% Shift the frequency domain to match MATLAB's shifted domain
omegal = fftshift(omega);
omega0 = 2*pi*c/l0;
l=1:1:nt;
else
%%%method 2
nt=N;%The number of steps in the time must be the same in the radial axis, the matrix dimention must match
time=4*T_FWHM;% windows time in seconds, is multiplyed by T_FHWM because the zero time correspond to maximum power
timehalf=0.5*time;
tau=linspace(0,timehalf,nt);%linspace(-timehalf,timehalf,nt);%time discretization
dt=time/nt;%delta time
l=1:1:nt;
domega=(2*pi)/(nt*dt);
omegal=(omega0 + ((l) - ((nt)/2))*domega); %frequency grid
% Shift the frequency domain to match MATLAB's shifted domain
omegal = (omegal);
end

f = omega/2/pi;
f_tot=frequency+f;%
l_lambda=clight./(f_tot); %%

```

**Figure B-8**.: Frequency and time discretization.

```

%%%Calculation and storage the tables in frequency domain
%K_l
K_l=k0 - vg.*omegal;
%T_l
T_l= ones(1,258);%1- (omegal./omega0);
%T_l^2
T_l2=T_l.^2;
%d_l, here goes the dispersion parameters beta2, beta3, ...
d_l= deltaz*(((beta2*(omegal).^2)/2) );
%delta_l
delta_l=(deltaz)./(2*(deltar^2).*(k0 - vg.*omegal));

```

**Figure B-9**.: Time operator and nonlinear operators discretization

```
%%%creating L+,l and L-,l

v_j= 1 + 1./(2.*(j(2:N-1))); %The size is given by j
v_jm=[0,v_j];%add a zero to obtain a square matrix and the boundary conditions
u_j= 1 - 1./(2.*j(2:N));
two=-2*ones(N,1);%creating the central diagonal of the tridiagonal matrix

deltaj= diag(two,0) + diag(u_j',-1) + diag(v_jm',1); %creating the matrix
%initializing vectors
Lpluscentral=zeros(N,1);
Lplusup=zeros(N-1,1);
Lplusdown=zeros(N-1,1);
Lplus=zeros(N,N);
Lminuscentral=zeros(N,1);
Lminusup=zeros(N-1,1);
Lminusdown=zeros(N-1,1);
Lminus=zeros(N,N);
```

**Figure B-10**.: $\nu_j$ and $\mu_j$ creation and $L_+$ and $L_-$ vectors initialization

```
for lk=1:N %for to walk trhough the different spectral components
delta= deltaz/(4*k0*(deltar^2));%if delta=0 there is no diffraction
delta_l=(deltaz)/(2*(deltar^2)*(k0 - vg*omegal(lk)));




Lpluscentral= 1 + (i*(delta_l/2)).*diag(deltaj,0) + ((1i/2)*d_l(lk));% L+ necessary to solve the matrix, central diagonali/
Lplusup=(i*(delta_l/2)).*diag(deltaj,1);%upper diagonal
Lplusdown=(i*(delta_l/2)).*diag(deltaj,-1);%down diagonal
Lplus(j+1,j+1,lk)= diag(Lpluscentral,0) + diag(Lplusup,1) + diag(Lplusdown,-1);%I have created L+ without the frequency terms and dl

% Lplus=1 + ((i*(delta/2)).*deltaj);
Lplus(1,:,lk)=0; %to meet boundary condition dE/dr=0 at r=0 E=0 at r_max
% Lplus(1,1)=1 - 4*i*delta;%second order accuracy
% Lplus(1,2)=4*i*delta;%second order accuracy
Lplus(N,:,lk)=0; %to meet boundary condition E=0 at r_max dE/dr=0

Lminuscentral= 1 - (i*(delta_l/2)).*diag(deltaj,0) - ((1i/2)*d_l(lk));% L- necessaty to solve the matrix
Lminusup= -(i*(delta_l/2)).*diag(deltaj,1);
Lminusdown= -(i*(delta_l/2)).*diag(deltaj,-1);
Lminus(j+1,j+1,lk)= diag(Lminuscentral,0) + diag(Lminusup,1) + diag(Lminusdown,-1);

% Lminus=1 - ((i*(delta/2)).*deltaj);

Lminus(1,:,lk)=0;%to meet boundary condition E=0 at r_max dE/dr=0
Lminus(N,:,lk)=0;%to meet boundary condition E=0 at r_max dE/dr=0
Lminus(1,1,lk)=1 ;%+4*i*delta;%to meet boundary condition E=0 at r_max dE/dr=0
Lminus(1,2,lk)=-1;%*4*i*delta;%to meet boundary condition E=0 at r_max dE/dr=0
Lminus(N,N,lk)=1;%to meet boundary condition E=0 at r_max dE/dr=0

 end
```

**Figure B-11**.: $L_+$ and $L_-$ matrices for each frequency creation

```
%% Loop of propagation
% A=E;
for kk=1:nt
          hRl(kk)=hR(tau(kk));
end
f_R=((1-fR)+fR*fft(fftshift(hRl)));%%%Raman - Frequency Domain
c2=0;
c1=0;

%initializing vectors
K1=zeros(N,N,M);
A_half2=zeros(N,N,M);
k2=zeros(N,N,M);
A_half3=zeros(N,N,M);
k3=zeros(N,N,M);
A_full=zeros(N,N,M);
k4=zeros(N,N,M);
A=zeros(N,N,M);
Q=zeros(N,N,M);
N kerr=zeros(N,N,M);
N_kerrf=zeros(N,N,M);
EF=zeros(N,N,M);
Nf=zeros(N,N,M);
V=zeros(N,N,M);
S=zeros(N,N,M);


for k=0:K
    %k_sfhit=k-1;%to start the loop in zero, the k+1 is because the loop needs to reach K
    c1=c1+1;
    for m=1:M
        n=k*M + m;
        c2=c2+1;

        %Here goes the electron density calculation
        %Here goes raman Kerr effect calculation
        %%%%%% Non-linear step using Runga-Kutta, 4th order
       for jj=1:N

         k1(jj,:,n) = NLT(E(jj,:,n));
         A_half2(jj,:,n) = E(jj,:,n) + k1(jj,:,n)*deltaz/2;
         k2(jj,:,n) = NLT(A_half2(jj,:,n));
         A_half3(jj,:,n) = E(jj,:,n) + k2(jj,:,n)*deltaz/2;
         k3(jj,:,n) = NLT(A_half3(jj,:,n));
         A_full(jj,:,n) = E(jj,:,n) + k3(jj,:,n)*deltaz;
         k4(jj,:,n) = NLT(A_full(jj,:,n));
         A(jj,:,n) = E(jj,:,n) + deltaz/6*(k1(jj,:,n) + 2*k2(jj,:,n) + 2*k3(jj,:,n) + k4(jj,:,n));
         Q(jj,:,n)=A(jj,:,n);
       end

       for jjj=1:N
           for kkk=1:N
               N_kerr(jjj,kkk,n)=((1i*w0*n2)/(c))*Q(jjj,kkk,n)*E(jjj,kkk,n);%(1i*gama)
           end
       end
       %fourier transform of the above tables and E as well
       for jd=1:N
       N_kerrf(jd,:,n)=(fft((N_kerr(jd,:,n))));%to make the fft along the rows where the radial position is fixed, but the time varies
       EF(jd,:,n)=(fft((E(jd,:,n))));%the result of the fft: each coulmn has the fft of the rows
       %EF(:,:,n)=EF(:,:,n)';
        %Calculate and storage table N
       end
        Nf(:,:,n)=((k0*deltaz)./(K_l)')*( T_l2*fftshift(N_kerrf(:,:,n)) );

        %loop on frequencies
        for ll=1:N
            V(:,ll,n)=(Lplus(:,:,ll))*((EF(:,ll,n)));

             if n-1==0
            S(:,ll,n)= V(:,ll,n) + (3/2)*Nf(:,ll,n);
        else
            S(:,ll,n)= V(:,ll,n) + (3*Nf(1,ll,n) - Nf(1,ll,n-1))/2;
             end
        EF(:,ll,n+1)=inv(Lminus(:,:,ll))*S(:,ll,n);
        end

        for jdd=1:N
        E(jdd,:,n+1)=(ifft(EF(jdd,:,n+1)));
        end
        %E(:,:,n+1)=E(:,:,n+1)';

        distan(n)=deltaz*n;%%%%Recording the steps


    end
end
```

**Figure B-12**.: Solution of the GNLSE with diffraction, dispersion and nonlinear terms.

# C. Publications

## C.1. List of publications

1. Palacio, S. V., & Herrera, R. A. (2019). Dispersive wave and four-wave mixing generation in noninstantaneous nonlinear fiber solitons. Applied Optics, 58(10), 2736-2744.

## C.2. Conferences (Oral presentation)

1. International Conference on Electromagnetics in advanced Applications IEEE, Cartagena, Colombia, 2018.

## C.3. Conferences (Poster presentation)

1. Frontiers in Optics/Laser science conference (FiO/LS), Washington DC 2017.
2. SPIE Optics + Photonics, Optical Engineering + Applications, San Diego, USA, 2018

## C.4. Awards

1. SPIE Student Author Travel Grant and MKS Instruments Award.

# Bibliography


[1] HANSSON, T.; MODOTTO, D.; WABNITZ, S. On the numerical simulation of Kerr frequency combs using coupled mode equations. Optics Communications, 2014, vol. 312, p. 134-136.

[2] Agrawal, G. P. (2000). Nonlinear fiber optics. In Nonlinear Science at the Dawn of the 21st Century (pp. 195-211). Springer, Berlin, Heidelberg.

[3] Azhar, M., Wong, G., Chang, W., Joly, N., & Russell, P. (2012). High pressure gases in hollow core photonic crystal fiber: A new nonlinear medium. arXiv preprint arXiv:1210.3482.

[4] Börzsönyi, A., Heiner, Z., Kalashnikov, M. P., Kovács, A. P., & Osvay, K. (2008). Dispersion measurement of inert gases and gas mixtures at 800 nm. Applied optics, 47(27), 4856-4863.

[5] Brée, C., Demircan, A., & Steinmeyer, G. (2011). Saturation of the all-optical Kerr effect. Physical review letters, 106(18), 183902.

[6] Azhar, M. (2013). Tunable using dense noble gases.

[7] Couairon, A., & Mysyrowicz, A. (2007). Femtosecond filamentation in transparent media. Physics reports, 441(2-4), 47-189.

[8] Li C. (2017) Optical Kerr Effect and Self-focusing. In: Nonlinear Optics. Springer, Singapore

[9] Azhar, M., Wong, G., Chang, W., Joly, N., & Russell, P. (2012). High pressure gases in hollow core photonic crystal fiber: A new nonlinear medium. arXiv preprint arXiv:1210.3482.

[10] Chang, W., Nazarkin, A., Travers, J. C., Nold, J., Hölzer, P., Joly, N. Y., & Russell, P. S. J. (2011). Influence of ionization on ultrafast gas-based nonlinear fiber optics. Optics express, 19(21), 21018-21027.

[11] Ermolov, A., Mak, K. F., Frosz, M. H., Travers, J. C., & Russell, P. S. J. (2015). Supercontinuum generation in the vacuum ultraviolet through dispersive-wave and soliton-plasma interaction in a noble-gas-filled hollow-core photonic crystal fiber. Physical Review A, 92(3), 033821.

[12] Akhmediev, N., & Karlsson, M. (1995). Cherenkov radiation emitted by solitons in optical fibers. Physical Review A, 51(3), 2602.

[13] Roy, S., Bhadra, S. K., & Agrawal, G. P. (2011). Dispersive wave generation in supercontinuum process inside nonlinear microstructured fibre. Current Science, 321-342.

[14] AUSTIN, Dane R., et al. Dispersive wave blue-shift in supercontinuum generation. Optics express, 2006, vol. 14, no 25, p.11997-12007.

[15] KÖTTIG, F., et al. Mid-infrared dispersive wave generation in gas- filled photonic crystal fibre by transient ionization-driven changes in dispersion. Nature communications, 2017, vol. 8, no 1, p. 813.

[16] Kasztelanic, R., Anuszkiewicz, A., Stepniewski, G., Filipkowski, A., Ertman, S., Pysz, D., ... & Buczynski, R. (2018). All-normal dispersion supercontinuum generation in photonic crystal fibers with large hollow cores infiltrated with toluene. Optical Materials Express, 8(11), 3568-3582.

[17] Dudley, J. M., Genty, G., & Coen, S. (2006). Supercontinuum generation in photonic crystal fiber. Reviews of modern physics, 78(4), 1135.

[18] Rostami, S., Chini, M., Lim, K., Palastro, J. P., Durand, M., Diels, J. C., ... & Richardson, M. (2016). Dramatic enhancement of supercontinuum generation in elliptically-polarized laser filaments. Scientific reports, 6, 20363.

[19] Shanor, C., Ensley, T., Hagan, D. J., Van Stryland, E. W., Wright, E. M., & Kolesik, M. (2016). Numerical investigation of enhanced femtosecond supercontinuum via a weak seed in noble gases. Optics express, 24(13), 15110-15119.

[20] Ermolov, A., Mak, K. F., Frosz, M. H., Travers, J. C., & Russell, P. S. J. (2015). Supercontinuum generation in the vacuum ultraviolet through dispersive-wave and soliton-plasma interaction in a noble-gas-filled hollow-core photonic crystal fiber. Physical Review A, 92(3), 033821.

[21] Zhao, P., Reichert, M., Benis, S., Hagan, D. J., & Van Stryland, E. W. (2018). Temporal and polarization dependence of the nonlinear optical response of solvents. Optica, 5(5), 583-594.

[22] Sheik-Bahae, M., Said, A. A., Wei, T. H., Hagan, D. J., & Van Stryland, E. W. (1990). Sensitive measurement of optical nonlinearities using a single beam. IEEE journal of quantum electronics, 26(4), 760-769.

[23] YIN, M., et al. Determination of nonlinear absorption and refraction by single Z-scan method. Applied Physics B, 2000, vol. 70, no 4, p.587-591.

[24] VAN STRYLAND, Eric W.; SHEIK-BAHAE, Mansoor. Z-scan measurements of optical nonlinearities. Characterization techniques and tabulations for organic nonlinear materials, 1998, vol. 18, no 3, p.655-692.

[25] YU, Jing; LI, Shaohui; WANG, Jinghua. The application of femtosecond lidar in atmosphere remote sensing. 2015.

[26] POTEMKIN, F. V.; MAREEV, E. I.; SMETANINA, E. O. Influence of wave-front curvature on supercontinuum energy during filamentation of femtosecond laser pulses in water. Physical Review A, 2018, vol. 97, no 3, p. 033801.

[27] D. Weaire, B. S. Wherrett, D . A. B. Miller, and S . D . Smith, "Effect of low-power nonlinear refraction on laser beam propagation in InSb," Opt. Letr.. vol. 4. pp. 331-333, 1974

[28] "Photonic Crystal Fibers - NKT Photonics." LASERS & FIBERS,www.nktphotonics.com/lasers-fibers/technology/photonic-crystal-fibers/.

[29] F. Benabid, J. C. Knight, G. Antonopoulos, and P. St. J. Russell, "Stimulated Raman scattering in hydrogen-filled hollow-core photonic crystal fiber," Science 298, 399–402 (2002)

[30] Travers, J. C., Chang, W., Nold, J., Joly, N. Y., & Russell, P. S. J. (2011). Ultrafast nonlinear optics in gas-filled hollow-core photonic crystal fibers. JOSA B, 28(12), A11-A26.

[31] Zhang, J., Wang, Z., & Chen, J. (2014). Simulations of Negative Curvature Hollow-core Fiber. In COMSOL Conference in Shanghai.

[32] Kolyadin, A. N., Kosolapov, A. F., Pryamikov, A. D., Biriukov, A. S., Plotnichenko, V. G., & Dianov, E. M. (2013). Light transmission in negative curvature hollow core fiber in extremely high material loss region. Optics express, 21(8), 9514-9519.

[33] Faccio, D., Couairon, A., & Di Trapani, P. (2007). Conical Waves, Filaments and Nonlinear Filamentation Optics. Aracne.

[34] Couairon, A., Brambilla, E., Corti, T., Majus, D., Ramírez-Góngora, O. D. J., & Kole-

sik, M. (2011). Practitioner's guide to laser pulse propagation models and simulation. The European Physical Journal Special Topics, 199(1), 5-76.

[35] Couris, S., Renard, M., Faucher, O., Lavorel, B., Chaux, R., Koudoumas, E., & Michaut, X. (2003). An experimental investigation of the nonlinear refractive index (n2) of carbon disulfide and toluene by spectral shearing interferometry and z-scan techniques. Chemical Physics Letters, 369(3-4), 318-324.

[36] Ganeev, R. A., Ryasnyanskiĭ, A. I., & Kuroda, H. (2006). Nonlinear optical characteristics of carbon disulfide. Optics and spectroscopy, 100(1), 108-118.

[37] Reichert, M., Hu, H., Ferdinandus, M. R., Seidel, M., Zhao, P., Ensley, T. R., ... & Hagan, D. J. (2014). Temporal, spectral, and polarization dependence of the nonlinear optical response of carbon disulfide. Optica, 1(6), 436-445.

[38] Wang, J. X., Jiang, D. Q., Gu, Z. Y., Yan, X. P. (2006). Multiwalled carbon nanotubes coated fibers for solid-phase microextraction of polybrominated diphenyl ethers in water and milk samples before gas chromatography with electron-capture detection. Journal of Chromatography A, 1137(1), 8-14.

[39] Chen, Y., O'Flaherty, S., Fujitsuka, M., Hanack, M., Subramanian, L. R., Ito, O., Blau, W. J. (2002). Synthesis, characterization, and optical-limiting properties of axially substituted gallium (III) naphthalocyanines. Chemistry of materials, 14(12), 5163-5168.

[40] Dong, X., Chen, J., Ma, Y., Wang, J., Chan-Park, M. B., Liu, X., Chen, P. (2012). Superhydrophobic and superoleophilic hybrid foam of graphene and carbon nanotube for selective removal of oils or organic solvents from the surface of water. Chemical communications, 48(86), 10660-10662.

[41] Vialla, F., Chassagneux, Y., Ferreira, R., Roquelet, C., Diederichs, C., Cassabois, G., Voisin, C. (2014). Unifying the low-temperature photoluminescence spectra of carbon nanotubes: The role of acoustic phonon confinement. Physical review letters, 113(5), 057402.

[42] Iiima S. Helical microtubules of graphitic carbon. Nature. 1991;354(6348):56-8.

[43] Vishalli, Singh C, Dharamvir K, Singhal S, Bhardwaj S, Shekhawat MS, et al. Production of carbon nanotubes by AC arc discharge method. AIP Conference Proceedings: AIP; 2013. p. 287-8.

[44] Niu K-Y, Sun J, Yang J, Du X-W. The synthesis of carbon nanotubes by pulsed-laser ablation of a nickel/carbon composite target in ethanol or ambient air. Science of Advanced Materials.2012;4(3-4):463-6.

[45] Thurakitseree T, Einarsson E, Xiang R, Zhao P, Aikawa S, Chiashi S, et al. Diameter controlled chemical vapor deposition synthesis of single-walled carbon nanotubes. Journal of nanoscience and nanotechnology. 2012;12(1):370-6.

[46] Chiodarelli N, Richard O, Bender H, Heyns M, De Gendt S, Groeseneken G, et al. Correlation between number of walls and diameter in multiwall carbon nanotubes grown by chemical vapor deposition. Carbon. 2012;50(5):1748-52.

[47] Yang H, Zhang L, Dong X, Zhu W, Zhu J, Nelson B, et al. Precise control of the number of walls formed during carbon nanotube growth using chemical vapor deposition. Nanotechnology. 2012;23(6):065604.

[48] Isaza M CA, Herrera Ramírez J, Ledezma Sillas J, Meza J. Dispersion and alignment quantification of carbon nanotubes in a polyvinyl alcohol matrix. Journal of Composite Materials. 2018;52(12):1617-26.

[49] Medina Escobar SA, Isaza Merino CA, Meza Meza JM. Mechanical and thermal behavior of polyvinyl alcohol reinforced with aligned carbon nanotubes. Matéria (Rio de Janeiro). 2015;20(3):794-802.

[50] Ruoff RS, Qian D, Liu WK. Mechanical properties of carbon nanotubes: theoretical predictions and experimental measurements. Comptes Rendus Physique. 2003;4(9):993-1008.

[51] Che J, Cagin T, Goddard III WA. Thermal conductivity of carbon nanotubes. Nanotechnology. 2000;11(2):65.

[52] Kholmanov IN, Magnuson CW, Piner R, Kim JY, Aliev AE, Tan C, et al. Optical, electrical, and electromechanical properties of hybrid graphene/carbon nanotube films. Advanced Materials. 2015;27(19):3053-9.

[53] Wan X, Dong J, Xing D. Optical properties of carbon nanotubes. Physical Review B. 1998;58(11):6756.

[54] Chen, Y. C., Raravikar, N. R., Schadler, L. S., Ajayan, P. M., Zhao, Y. P., Lu, T. M., Zhang, X. C. (2002). Ultrafast optical switching properties of single-wall carbon nanotube polymer composites at $1.55\mu m$. Applied Physics Letters, 81(6), 975-977.

[55] Guo, G. Y., Chu, K. C., Wang, D. S., Duan, C. G. (2004). Linear and nonlinear optical properties of carbon nanotubes from first-principles calculations. Physical Review B, 69(20), 205416.

[56] Chen, P., Wu, X., Sun, X., Lin, J., Ji, W., Tan, K. L. (1999). Electronic structure and

optical limiting behavior of carbon nanotubes. Physical review letters, 82(12), 2548.

[57] Liu, X., Si, J., Chang, B., Xu, G., Yang, Q., Pan, Z., Wan, M. (1999). Third-order optical nonlinearity of the carbon nanotubes. Applied physics letters, 74(2), 164-166.

[58] JIN, Zhaoxia, et al. Nonlinear optical properties of some polymer/multi-walled carbon nanotube composites. Chemical Physics Letters, 2000, vol. 318, no 6, p. 505-510.

[59] Chen, S. Q., Liu, Z. B., Zang, W. P., Tian, J. G., Zhou, W. Y., Song, F., Zhang, C. P. (2005). Study on Z-scan characteristics for a large nonlinear phase shift. JOSA B, 22(9), 1911-1916.

[60] Kwak, C. H., Lee, Y. L., Kim, S. G. (1999). Analysis of asymmetric Z-scan measurement for large optical nonlinearities in an amorphous As 2 S 3 thin film. JOSA B, 16(4), 600-604.

[61] Falconieri, M. (1999). Thermo-optical effects in Z-scan measurements using high-repetition-rate lasers. Journal of Optics A: Pure and Applied Optics, 1(6), 662.

[62] Olayo R, Garcia E, Garcia-Corichi B, Sanchez-Vazquez L, Alvarez J. Poly (vinyl alcohol) as a Stabilizer in the Suspension Polymerization of Styrene: The Effect of the Molecular Weight. Journal of applied polymer science. 1998;67(1):71-7.

[63] Lu K, Lago R, Chen Y, Green M, Harris P, Tsang S. Mechanical damage of carbon nanotubes by ultrasound. Carbon. 1996;34(6):814-6.

[64] Mukhopadhyay K, Dwivedi CD, Mathur GN. Conversion of carbon nanotubes to carbon nanofibers by sonication. Carbon. 2002;40(8):1373-6.

[65] A. I. Ryasnyansky, R.I. Tugushev, T. Usmanov R. A. Ganeev, "Characterization of Nonlinear Optical Parameters Of Metal-Doped Polyvinylpyrrolidone Nanostructures And Organic Dye Molecule", NATO Sciences Series, (2003).

[66] R. Boyd, "Nonlinear Optics", (Academic press; 2008).

[67] R. R. Alfano and S. L. Shapiro, "Observation of self-phase modulation and small-scale filaments in crystals and glasses," Phys. Rev. Lett., vol. 24, no. 11, pp. 592–594, 1970.

[68] M. Chemnitz et al., "Hybrid soliton dynamics in liquid-core fibres," Nat. Commun., vol. 8, no. 1, pp. 1–10, 2017.

[69] R. Zhang, J. Teipel, and H. Giessen, "Theoretical design of a liquid-core photonic crystal fiber for supercontinuum generation," Opt. Express, vol. 14, no. 15, p. 6800, 2006.

[70] R. A. Ganeev, A. I. Ryasnyansky, M. Baba, M. Suzuki, N. Ishizawa, M. Turu, S.

Sakakibara, and H. Kuroda, "Nonlinear refraction in CS2," Appl. Phys. B 78, 433–438 (2004).

[71] Zhao, Peng and Reichert, Matthew and Benis, Sepehr and Hagan, David J. and Van Stryland, Eric W.,"Temporal and Polarization dependece of the nonlinear optical responce of solvents", Optica, vol. 5, no. 5, p. 583, May. 2018.

[72] H. Takara, T. Ohara, K. Mori, K. Sato, E. Yamada, Y. Inoue, T. Shibata, M. Abe, T. Morioka, and K.-I. Sato, "More than 1000 channel optical frequency chain generation from single supercontinuum source with 12.5 GHz channel spacing," Electron. Lett. **36**, 2089-2090 (2000).

[73] Topics in Applied Physics. "Ultrafast Laser Pulses and Applications," Editor: W. Kaiser. Vol. **60**. Springer-Verlag. Berlin Heidelberg (1988).

[74] Samudra Roy, S. K. Bhadra, and Govind P. Agrawal. "Dispersive waves emitted by solitons perturbed by third-order dispersion inside optical fibers", Phy. Rev. A. 79, 023824-1 (2009).

[75] Rostami, S., Chini, M., Lim, K., Palastro, J. P., Durand, M., Diels, J. C., ... & Richardson, M. (2016). Dramatic enhancement of supercontinuum generation in elliptically-polarized laser filaments. Scientific reports, 6, 20363.

[76] Conti, C., Schmidt, M. A., Russell, P. S. J., & Biancalana, F. (2010). Highly noninstantaneous solitons in liquid-core photonic crystal fibers. Physical review letters, 105(26), 263902.

[77] Chemnitz, M., Gaida, C., Gebhardt, M., Stutzki, F., Kobelke, J., Tünnermann, A., ... & Schmidt, M. A. (2018). Carbon chloride-core fibers for soliton mediated supercontinuum generation. Optics express, 26(3), 3221-3235.

[78] Pniewski, J., Stefaniuk, T., Le Van, H., Van, L. C., Kasztelanic, R., Stepniewski, G., ... & Buczynski, R. (2016). Dispersion engineering in nonlinear soft glass photonic crystal fibers infiltrated with liquids. Applied optics, 55(19), 5033-5040.

[79] Ebnali-Heidari, M., Saghaei, H., Koohi-Kamali, F., Moghadasi, M. N., & Moravvej-Farshi, M. K. (2014). Proposal for supercontinuum generation by optofluidic infiltrated photonic crystal fibers. IEEE Journal of Selected Topics in Quantum Electronics, 20(5), 582-589.

[80] Chemnitz, M., Scheibinger, R., Gaida, C., Gebhardt, M., Stutzki, F., Pumpe, S., ... & Schmidt, M. A. (2018). Thermodynamic control of soliton dynamics in liquid-core fibers. Optica, 5(6), 695-703.

[81] Kedenburg, S., Vieweg, M., Gissibl, T., & Giessen, H. (2012). Linear refractive index and absorption measurements of nonlinear optical liquids in the visible and near-infrared spectral region. Optical Materials Express, 2(11), 1588-1611.

[82] Jiang, P., Schroeder, T., Bath, M., Lesnyak, V., Gaponik, N., Eychmüller, A., & Benson, O. (2012). Incoherent photon conversion in selectively infiltrated hollow-core photonic crystal fibers for single photon generation in the near infrared. Optics express, 20(10), 11536-11547.

[83] Xiao, L., Jin, W., Demokan, M. S., Ho, H. L., Hoo, Y. L., & Zhao, C. (2005). Fabrication of selective injection microstructured optical fibers with a conventional fusion splicer. Optics Express, 13(22), 9014-9022.

[84] Kieu, K., Schneebeli, L., Norwood, R. A., & Peyghambarian, N. (2012). Integrated liquid-core optical fibers for ultra-efficient nonlinear liquid photonics. Optics Express, 20(7), 8148-8154.